

A Method to Predict Transitions in Material Behavior

by

John J. Wlassich

B.S., Mechanical Engineering, 1983
University of Rhode Island

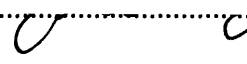
S.M., Mechanical Engineering, 1985
Massachusetts Institute of Technology

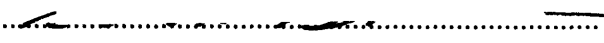
Submitted to the Department of Mechanical Engineering
in Partial Fulfillment of the Requirements for the Degree of
Doctor of Philosophy

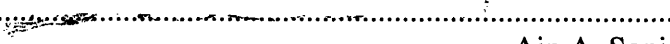
at the

Massachusetts Institute of Technology
May 1995

© Massachusetts Institute of Technology 1995
All rights reserved

Signature of Author
 Department of Mechanical Engineering
May 10, 1995

Certified by

Stuart B. Brown
Richard P. Simmons Associate Professor of Materials Manufacturing
Thesis Supervisor

Accepted by

Ain A. Sonin
Professor of Mechanical Engineering
Chair, Departmental Committee on Graduate Students

MASSACHUSETTS INSTITUTE
OF TECHNOLOGY

AUG 31 1995

Barker Eng

A Method to Predict Transitions in Material Behavior

by

John J. Wlassich

Submitted to the Department of Mechanical Engineering
in Partial Fulfillment of the Requirements for the
Degree of Doctor of Philosophy at the
Massachusetts Institute of Technology

Abstract

This work addresses two transitions in material behavior: one, the initial peak in stress response associated with dynamic recrystallization and two, the rapid increase in grain growth rate associated with pore separation from grain boundaries. A criterion is derived that predicts the initial peak in stress response associated with dynamic recrystallization, and another criterion is derived that predicts the rapid increase in grain growth rate associated with pore separation from grain boundaries.

The criterion for the initial peak in stress associated with dynamic recrystallization shows the interaction between the rate of dislocation accumulation and the rate of recrystallization, modified by the individual contribution of dislocation density and recrystallized volume fraction. It is the first criterion for dynamic recrystallization that shows explicitly the interaction of internal structure with temperature and strain rate. The criterion for the rapid increase in grain growth rate associated with pore separation shows the interaction between the grain growth rate and the densification rate, modified by the grain size and relative porosity of the material. It is the first criterion for pore separation that explicitly shows the effect of variations in temperature, pressure, and material parameters on internal structure; none of the existing criteria account for all of these quantities at once. Both criteria derived in this work show good agreement with experimental data. The criteria's sensitivity to uncertainties in parameter values is shown.

The criteria are presented in two equivalent forms: as algebraic expressions and graphically as processing envelopes. In either form the criteria can assist the planning of component fabrication processes, such as hot rolling or sintering, because components made from materials that sustain an unintended transition in material behavior are rendered useless.

Finally, work is presented on a general, structured method to derive a convergence rate criterion for complex transitions in material behavior governed by coupled, simultaneous kinetic processes.

Thesis Supervisor: Professor Stuart B. Brown
Richard P. Simmons Associate Professor of Materials Manufacturing

Acknowledgments

Fifty years ago this month my mother wrote in her diary, “today I had a warm meal”. A few months later, diary in hand, she was straining to see the Statue of Liberty from the deck of a crowded freighter.

Fifty years ago my father, despite profoundly poor eyesight, was conscripted into the dying days of the war. He survived and emigrated to Canada. Together with my mother they settling in Providence, Rhode Island and sold Fuller brushes door-to-door.

My first and final thanks go to my parents for providing opportunities that my sister and I have been privileged to choose from.

Of course this is the page where thesis advisors are acknowledged too! I’d like to tell you a little about Prof. Stuart Brown. His ideas have impact, his engineering solutions simple and elegant. He has been advisor/mentor in the best tradition.

My officemates: Chris, Mayank, Patricio, Prat, and Will are why it is hard for me to celebrate finishing my studies. Their day-to-day company will be sorely missed.

Table of Contents

<u>Chapter</u>	<u>Page</u>
1- Introduction	12
1.1 Previous Research to Predict Transitions in Material Behavior	14
1.1.1 Standard Practices	15
1.1.2 Mathematically More Advanced Approaches	16
1.2 Introduction to the Following Chapters	17
1.2.1 Chapter 2 - A Criterion for Dynamic Recrystallization.....	18
1.2.2 Chapter 3 - A Criterion for Pore Separation	18
1.2.3 Chapter 4 - Formulating a Characteristic Time	18
1.2.4 Chapter 5 - Closing	19
2 - A Criterion for Dynamic Recrystallization	20
2.1 Previous Work to Develop a Criterion for Dynamic Recrystallization	23
2.2 Internal Variable Model	24
2.2.1 General form of an Internal Variable Model	24
2.2.2 Internal Variable Model Analyzed in this Work	25
2.3 Evaluation of the Performance of the Internal Variable Model	29
2.4 Derivation of A Criterion for Dynamic Recrystallization	37
2.4.1 A General Approach to Formulating a Criterion	38
2.4.2 The General Approach Applied to Dynamic Recrystallization	39
2.5 Evaluation of the Performance of the Criterion	42
2.6 Discussion of Implications of the Criterion	43
Nomenclature	52

<u>Chapter</u>	<u>Page</u>
3 - A Criterion for Pore Separation	54
3.1 Previous Work to Develop a Criterion for Pore Separation	58
3.1.1 Previous Local Analyses of Pore Separation	58
3.1.2 Previous Global Analyses of Pore Separation	59
3.1.3 Selected Assumptions used in this Chapter from Previous Work	60
3.2 Internal Variable Model of Grain Growth and Densification Kinetics	62
3.3 Evaluation of the Performance of the Internal Variable Model	64
3.4 A Criterion Based on a Global Analysis of Pore Separation	66
3.5 A Criterion Based on a Local Analysis of Pore Separation	71
3.6 Evaluation of the Performance of the Criteria	80
3.7 Discussion of the Implications of the Criterion	82
Nomenclature	89
4 - Formulating a Characteristic Time	92
4.1 Previous Work to Derive a Characteristic Time	92
4.1.1 Widely Practiced Approaches	93
4.1.2 Mathematically More Advanced Approaches	94
4.2 Approach in General	95
4.3 Unresolved Issues of this Approach	101
4.4 A Characteristic Time for Pore Separation	105
4.5 Comparison to Simulations	107

<u>Chapter</u>	<u>Page</u>
5 - Closing	112
5.1 Main Results of this Work	112
5.2 Suggested Improvements to the Internal Variable Models	112
5.3 Preliminary Work on using the Models in an Adaptive Controller	113
5.3.1 Feedback Linearization	114
5.3.2 Adaptive Control with Dynamic Parameter Estimation	116
5.3.3 Simulation Results	119
5.4 Suggested Future Work	121
References	124

List of Figures

<u>Figure</u>	<u>Page</u>
2.1 (a) Schematic of the microstructural evolution characterizing dynamic recrystallization, from Frost and Ashby [14]. (b) Micrograph on left shows an old, deformed grain with the numerous dislocation structures while the micrograph on the right shows a newly recrystallized grain with a relatively low dislocation density, from Sakai and Ohashi [15].	21
2.2 Oscillating stress/strain curves for OFHC copper deformed at 0.002 1/s strain rate and five different temperatures, from Blaz et. al. [29]. Micrographs used only to roughly illustrate the linkage between the stress peak and the evolution in microstructure. The micrographs are the same as those shown in figure 2.1.	22
2.3 Simulated time-evolution in dislocation density (nondimensionalized by the steady state dislocation density, ρ_{ss}) and volume fraction recrystallized for OFHC copper at 775 K and a strain rate of 0.002 s^{-1} .	35
2.4 State trajectories showing the dislocation density (nondimensionalized by the steady state dislocation density, ρ_{ss}) and volume fraction recrystallized for OFHC copper at a strain rate of 0.002 s^{-1} and three different temperatures; 675 K, 775 K, 975 K.	36
2.5 State trajectories of the dislocation density (nondimensionalized by the steady state dislocation density, ρ_{ss}) and volume fraction recrystallized for OFHC copper at 775 K and two strain rates; 0.02 and 0.002 s^{-1} .	37
2.6 Comparison of strain at peak stress as a function of temperature. Points are predicted strains using the model and the criterion. Vertical bars show variation in the strain at peak stress reported by Blaz et. al. [29] due to a variation in initial grain size.	43
2.7 Comparison of strain at peak stress as a function of temperature. Curved line is the predicted strain using the model and the criterion. Points are experimental data from Luton [40] for OFHC copper. Plot (a) is for 0.00049 s^{-1} strain rate and (b) is for 0.00081 s^{-1} strain rate.	44

Figure

Page

- 2.8** Comparison of strain at peak stress as a function of temperature. Curved line is the predicted strain using the model and the criterion. Points are experimental data from Luton [40] for OFHC copper. Plot (a) is for 0.0016 s^{-1} strain rate and (b) is for 0.0049 s^{-1} strain rate.45
- 2.9** Numerical value of the criterion as a function of strain for isothermal, $T = 775 \text{ K}$, constant strain rate, $\dot{\epsilon} = 0.02 \text{ 1/s}$ conditions.46
- 2.10** Simulated state trajectory for $T = 775 \text{ K}$ and $\dot{\epsilon} = 0.002 \text{ 1/s}$, until intersection with the boundary denoting the first peak in stress, equation (2.32).47
- 2.11** Processing envelope. Surface gives strains at peak stress, as a consequence of dynamic recrystallization, for isothermal, constant strain rate conditions.48
- 2.12** Effect of a -20% change in the activation energy for vacancy self diffusion, Q_{sd} on the criterion predicting the first peak in stress and the state trajectory (upper trajectory corresponds to the unchanged case).50
- 3.1** a) Schematic of the microstructural evolution characterizing pore separation. (b) Micrograph on the left shows closed voids residing primarily on grain boundaries. Micrograph on upper right shows pores separated from grain boundaries, from Aigeltinger [42]. Micrograph on lower right is a copy of the one on the left to roughly illustrate continued pore attachment.....55
- 3.2** Simulated state trajectory showing the effect of pore separation for OFHC copper at $T = 1200 \text{ K}$ and $P = 50 \text{ MPa}$. Micrographs are the same used in figure 3.1 to illustrate roughly the linkage with microstructural evolution.....56
- 3.3** Global geometric model of a pore separation.57
- 3.4** Local geometric model of pore separation.57
- 3.5** Vector field and a state trajectory using parameter values for copper tabulated in [14], $T = 1200 \text{ K}$, $P = 50 \text{ MPa}$, $R_{max} = 80 \mu\text{m}$, $\tilde{R}_0 = 0.35$, and $\Delta_0 = 0.92$.65
- 3.6** Plot of Ashby's criterion, equation (3.19), and the criterion derived in this section, equation (3.32), using parameter values for alumina [14] with $T = 2123 \text{ K}$72

Figure

Page

- 3.7** Evolution of free-energy for the local geometric model of a pore separation.73
- 3.8** Plot of the numerical values of $Ts - u$ and $\frac{\pi a^2 \gamma}{3f}$ as a function of temperature using values of s and u for iron from [65], and $f = 0.78$. The intersection of the two curves is the point where the bracketed term in equation (3.35) is equal to zero.....75
- 3.9** Comparison of the surface area of the cone and the catenoid of revolution for $r = 5 \mu m$, $R = 100 \mu m$, and $\theta = 45^\circ$. Only a quarter-section is shown.76
- 3.10** Separation criterion developed in this work and Ashby's criterion. Experimental data for alumina from Patterson [67] and Long [68]. A solid circle denotes experimental data for pores separated from grain boundaries. (a) Simulation for $T = 1873K$ and $P = 1 \text{ atm}$. (b) for $T = 2123K$ and $P = 0.1 \text{ atm}$ 81
- 3.11** Separation criterion developed in this work and Ashby's criterion. A solid circle denotes experimental data for pores separated from grain boundaries. (a) Simulation for $T = 1523K$ and $P = 1 \text{ atm}$, experimental data for nickel from Watwe [69]. (b) Hollow circles denotes experimental data for pores attached to grain boundaries. Simulation for $T = 1278K$ and $P = 1 \text{ atm}$, experimental data for copper from Aigeltinger [42].83
- 3.12** Separation criterion developed in this work and Ashby's criterion. A grey-filled circle denotes experimental data showed pores were neither predominantly attached nor separated. Simulation for $T = 2123K$ and $P = 1 \text{ atm}$, experimental data for alumina from Patterson [67].84
- 3.13** Variation in the separation criterion as a function of changes in: (a) pressure, at constant temperature $T = 1523 \text{ K}$ and (b) temperature, at constant pressure $P = 50 \text{ MPa}$, all for nickel with $R_m = 7 \mu m$ 86
- 3.14** Simulated effect of a -5% change in the activation energy for core diffusion, Q_c , on the separation boundary. Simulation is for low carbon steel using parameter values from [54], at $T = 1500 \text{ K}$ and $P = 50 \text{ MPa}$88
- 4.1** An example of the upper bound on Φ given by equation (4.6).96
- 4.2** Example of mapping an evolution in $\Phi(z)$ to $\tilde{\lambda}(z)$ 100

Figure

Page

4.3	Example of mapping an evolution in $\Phi(\underline{z})$ to $\tilde{\lambda}(\underline{z})$	100
4.4	Example of mapping an evolution in $\Phi(\underline{z})$ to $\tilde{\lambda}(\underline{z})$	101
4.5	Example of mapping an evolution in $\Phi(\underline{z})$ to $\tilde{\lambda}(\underline{z})$	101
4.6	Geometric interpretation of the characteristic time based on the upper bound Φ_u , for the specific evolution in $\Phi(\underline{z})$ shown.	102
4.7	Case in which τ_u fails as a prediction of $t_{\text{transition}}$	103
4.8	Example of changes in the shape of $\Phi(t)$ which result in the characteristic time, τ_u , being not proportional to the time-to-transition, $t_{\text{transition}}$	104
4.9	Simulation of the upper bound on the free energy $G_u(t)$, equation (4.22), and the free energy $G(t)$, equation (4.16) using copper parameter values listed in [54] where $\Delta_0 = 0.92$ and $R_0 = 0.25$ with $T = 1300$ K and $P = 1$ atm	107
5.1	Block diagram of the feedback linearization given by equations (5.1) to (5.5) and (5.8) to (5.10).	117
5.2	Block diagram of the resulting dynamics of the feedback-linearization system illustrated in figure 5.1.	118
5.3	Block diagram of one-half of the adaptive controller, equations (5.12) to (5.18), with feedback-linearized plant, equations (5.6).	120
5.4	Simulation of the adaptive control strategy using inputs and parameter values to facilitate validation of the computer program.	121
5.5	Partial time-histories of temperature and strain rate inputs required to for the states to evolve to $v_r = 0.3$ and $\rho = 1 \times 10^{14}$ m/m ³	122

List of Tables

<u>Table</u>	<u>Page</u>
2.1	Parameter values for OFHC copper.31
3.1	Magnitude of equations (3.20) and (3.22) for $\tilde{R} = 0.2$, $\Delta = 0.92$, and $T = 1500$ K.71
3.2	Parameter values for iron used in equations (3.20) and (3.22) from [65][71].....72
3.3	Results of a sign test applied to the pore separation criteria and experimental data in figures 3.9 through 3.12.84
4.1	Simulated time-to-separation compared to predictions by the characteristic time. Unless otherwise noted, the initial state of each simulation was $\tilde{R}_0 = 0.4$ and $\Delta_0 = 0.92$, for $T = 1573$ K and $P = 50$ MPa. Simulations used parameter values for alumina from [54].109
4.2	Model-exact time-to-separation as a function of changes in initial state, temperature, pressure, and material parameter values for alumina. Unless otherwise noted, the initial state of each simulation was $\tilde{R}_0 = 0.4$ and $\Delta_0 = 0.92$, for $T = 1573$ K and $P = 50$ MPa.111

CHAPTER 1 Introduction

Hot working operations such as rolling, forging, and extrusion can trigger a rapid transition in material behavior. A rapid transition in behavior, such as a sudden change in deformation resistance, can complicate the control of hot working operations. In some instances the transition is desired, for example when dynamic recrystallization is exploited to refine grain size. Whether the transition is desirable or undesirable, control of the hot working process is improved if the transition can be predicted.

The most widely practiced approach to derive criteria to predict transitions in material behavior has been to model their governing kinetic processes as decoupled, parallel or serial processes. The ability of this approach to continue to provide sufficient analysis is being strongly challenged by a growing need to predict *complex* transitions governed by multiple, *simultaneous*, coupled kinetic processes [1, 2, 3]. This work addressed complex transitions in material behavior governed by multiple, simultaneous, coupled kinetic processes that cannot be adequately modelled by decoupling the kinetic processes into component parallel or serial processes.

The goal of this research was to develop criteria to predict complex transitions in material behavior governed by simultaneous, coupled kinetic phenomena. A predictive capability was defined as having three parts:

1. An expression relating the transition to the states of the material, processing inputs, and material parameters.
2. An estimate of the rate of convergence to the transition as a function of the state variables of the material, processing inputs, and material parameters.
3. An ability to evaluate the effect of uncertainty in material parameter values on (1) and (2).

The predictive capability could be used to assist the planning of component fabrication processes and the design of new component fabrication equipment. The mathematical

expressions making up the predictive capability should be simple so that they can be readily understood. A graphical interpretation of these relations, in the form of processing envelopes, will help put the criteria into practice.

The approach to reach the goal was divided into three steps. Step one, investigate several transitions in material behavior to find candidates for further analysis. Candidate transitions in material behavior had to be complex, i.e. governed by simultaneous, coupled kinetic processes. Candidate transitions also had to have a large body of published experimental data showing the transition occurring for many process input values and initial conditions. Experimental data would be necessary to validate the criteria and to provide material parameter values for the models of the governing kinetic processes. Step two, choose two or three transitions from amongst the candidates and derive criteria for them. Step three, generalize the derivation of these criteria based on insight gained during step two.

Four different transitions in material behavior were investigated: dynamic recrystallization, shear localization, pore separation from grain boundaries, and superplastic flow. Each of these transitions in material behavior have been characterized by experiments for over forty years. Two of these were chosen for further analysis: dynamic recrystallization and pore separation from grain boundaries, because they appeared to have the largest amount of published experimental data giving quantifying the evolution of microstructure during each transition.

There were two premises implicit to this approach. One, previous researchers have published some mathematical models that characterize the simultaneous, coupled kinetic processes governing complex transitions. Two, these models take the form of coupled, nonlinear ordinary differential equations with a stability structure containing *a boundary corresponding to the transition* in material behavior. The boundary might be the boundary of a domain of attraction, a boundary manifold, a trajectory describing a limit cycle, or even a bifurcation. If the transition in material behavior could be linked to the boundary, then a mathematical expression for the boundary is also a criteria for the transition in terms of the state of the material. An expression for the boundary might be derived using analysis methods from nonlinear dynamics, given the assumed general form of the model.

These two premises were found to be only partially valid. First, it was found that mathematical models of the kinetic processes associated with complex transitions either do not exist or are only partially developed. Therefore, it was necessary to first model the kinetic processes associated with the two transitions chosen before criteria could be derived. The modelling effort yielded a new model of the kinetics associated with dynamic recrystallization and modifications of a model of the kinetics linked to pore separation. These models are presented at the beginning of chapters 2 and 3, respectively. Each model is comprised of two, first-order, coupled, nonlinear differential equations. The time-evolution of the state variables governed by these models shows good agreement with experimental data.

Second, it was found that neither model had a stability structure containing a boundary that corresponds to the transition being investigated. Each model produced a gradient field for a wide range of process inputs and parameter values. This fact will be shown in chapters 2 and 3.

Nevertheless, chapters 2 and 3 show that it was still possible to use these models to develop a criterion to predict the first peak in stress associated with dynamic recrystallization and a criterion to predict the rapid increase in grain growth resulting from pore separation from grain boundaries. The approach is to introduce an auxiliary, scalar-valued function of the states of the system that has a feature in its time-evolution that corresponds to the transition in material behavior. The model of the kinetic processes are then mathematically linked to the auxiliary function to form a criterion. The criteria so derived are the first to explicitly show the dependence of the transitions on the microstructure of the material, processing inputs, and material parameters.

1.1 Previous Research to Predict Transitions in Material Behavior

This section describes some established approaches to derive criteria to predict transitions in material behavior. The first section reviews standard practices and gives examples taken from the literature. The second section discusses mathematically more advanced methods than the standard practices. The beginning of chapters 2, 3, and 4 review research efforts specific to each topic of those chapters.

1.1.1 Standard Practices

The most commonly analyzed transitions governed by multiple kinetic processes are those that can be analyzed by modelling the kinetic processes as decoupled parallel or serial processes. Levenspiel 4 presents a good review of transitions that yield to this analysis technique. Examples of such transitions occur in certain gas/solid reactions, such as burning coal or wood, and fluid/fluid reactions, such as the nitration of sulfuric acid to form nitroglycerin.

Consider gas/solid reactions. Under certain circumstances, this reaction can be modelled as the dynamic interaction of two kinetic processes: mass transfer and a chemical reaction 4. The mass transfer and chemical reaction are treated as processes in series. At one extreme, when the processing temperature is such that the chemical reaction is very fast, the mass transfer controls the overall rate of the phenomena. The mass transfer is modelled by a single, first-order differential equation. It has the same form as the constitutive equation for a conductance, i.e. a flow variable set equal to an effort variable multiplied by an inverse resistance. Here, the flow variable is the time rate of change of moles reactant in the gas phase and the effort variable is the concentration of the reactant in the gas phase. The conductance is made up from the individual contribution of two conductances: one, the conductance as modelled by the mass transfer coefficient of the gas, and two, the conductance as modelled by the mass transfer coefficient of the liquid, added according to the law for conductances in series. At the other extreme, when the processing temperature is such that the mass transfer is very fast, the chemical reaction rate controls the overall rate of the phenomena. The analysis proceeds as just described for mass transfer control of the overall rate of the phenomena. The result is another, single, first-order differential equation that governs the time rate of the change of moles reactant in the gas phase.

The processing temperature determines the transition between these two extremes, mass-transfer-control and chemical-reaction-control. The reaction rates change with temperature since the conductances are functions of temperature. By plotting the two reaction rates, one from the mass-transfer-control extreme and one from the chemical-reaction-control extreme, versus temperature on a single plot, the transition boundary

emerges. The plot shows two curves each curve giving a much larger reaction rate as compared to the other for a certain range of temperature, as expected. The temperature range in-between the two ranges where one reaction rate dominates over the other is considered the transition boundary.

There are two commonly practiced methods of determining transitions in material behavior governed by multiple kinetic processes that cannot be approximated by decoupling the kinetics into component parallel or serial processes. The first method uses linearization of the material behavior model and subsequent analysis of the linear system by linear methods. Analysis of complex transitions by linear techniques may not be sufficient since linearization results in the loss of subtle nonlinearities that may characterize the coupling of the kinetic processes. The second method uses numerical integration of the material behavior model for a set of initial conditions. Numerical methods alone often do not give sufficient confidence that the behavior of a material has been characterized for all initial conditions, processing inputs, and parameter values. In addition, numerical methods do not explicitly show the dependence of the material behavior on initial conditions, processing inputs, and parameter values.

1.1.2 Mathematically More Advanced Approaches

Investigators have applied more advanced mathematics to analyze transitions in material systems. Penrose and Fife ⁵ used a requirement of stability to specify the proper form of Lyapunov functions associated with phase transformations. Their Lyapunov functions were correlated with measures of free energy and entropy. The results of their work did not include specific kinetic equations for a given material process. Gegel ⁶ recommended the use of Lyapunov stability methods to analyze internal variable models but did not apply the methods to any particular system. Holmes ⁷ has investigated the stability properties of models of systems from continuum mechanics. These models take the form of systems of partial differential equations, unlike the models used in this work that take the form of systems of nonlinear ordinary differential equations.

More generally, there are methods from nonlinear dynamics that have been developed to investigate the stability structure of systems of nonlinear ordinary differential equations that could be applied to models of kinetic processes governing material behavior. The

texts by Strogatz 8, Slotine and Li 9, and Luenberger 10 give comprehensive introductions to these methods. These texts give numerous examples of systems with stability structures containing attractors, repellers, saddles, limit cycles, bifurcations, domains of attraction, and boundary manifolds (also known as a separatrices). Hahn 11 also provides a review of methods from nonlinear dynamics and shows more of the real analysis to prove many of the theorems that comprise these methods. Hahn also provides some interesting theorems not commonly found elsewhere. One such theorem is Zubov's theorem. Fantastically, Zubov's theorem offers a way to derive an expression for the boundary of the domain of attraction. An expression for the boundary of the domain of attraction has great potential. If, for instance, a transition in material behavior was linked to the boundary of a domain of attraction, then an expression for the domain of attraction is a criteria for the transition in terms of the state variables of the material.

Finally, there are approximate solution methods for systems of nonlinear differential equations, such as describing functions and perturbation methods. Describing functions replace a nonlinear term in a system with a linear time-invariant system. The linear system is chosen by fulfilling criteria that show it to be the best among alternative candidate linear systems. Perturbation methods are used to compare the behavior of systems where a particular term is at first present and then later missing. This can be used to understand the effects of nonlinearities on the stability structure of a system. Walter 12, Vidyasagar 13, and Hahn 11 give mathematically concise reviews of approximate solution methods for systems of nonlinear differential equations. As mentioned previously, linear techniques were not the focus of this research.

1.2 Introduction to the Following Chapters

The research reported in this document is interdisciplinary, including modelling of material kinetic processes, methods from nonlinear system dynamics, and adaptive control theory. To help the reader use the information in this text, each of the following chapters starts with a description of the issues addressed in those chapters assuming only a general engineering background. The following sections give a brief synopsis of each of the remaining chapters.

1.2.1 Chapter 2 - A Criterion for Dynamic Recrystallization

This chapter shows the derivation of a criterion for the first peak in stress response associated with dynamic recrystallization. The derivation is first shown in general. Then the general approach is applied to the specific problem of dynamic recrystallization. The performance of the criterion is evaluated by comparing its predictions to experimental data. Implications of this criterion to the design of hot deformation processes, such as rolling or extrusion, are then discussed. The criterion is used to make processing envelopes to help guide the selection of process inputs, such as temperature and strain rate, or the materials themselves. The general approach that is applied to dynamic recrystallization in this chapter is applied again in the next chapter to derive a criterion for the onset of pore separation from grain boundaries during consolidation processing.

1.2.2 Chapter 3 - A Criterion for Pore Separation

Two criteria for the onset of pore separation are presented in this chapter. The derivation of the first criterion takes pores separation as the simultaneous detachment of several pores from a single grain. An existing, popular criterion for pore separation also takes pore separation as the simultaneous detachment of several pores from a single grain. It is shown, for the first time, that the popular criterion fails to account for the effect of entropy transfer, which is included in the derivation of first criterion proposed in this chapter. The derivation of the second criterion takes pore separation as the detachment of a single, isolated pore from a two-grain boundary. Taking the onset of pore separation as the detachment of a single, isolated pore from a two-grain boundary requires fewer modelling assumptions than the approach taken by the first criterion and yields better results. The second criterion is an explicit function of both temperature and pressure whereas the first criterion accounts for temperature explicitly but only indirectly accounts for processing pressure. Implications of the second criterion to guide the planning of pressure and temperature schedules for hot isostatic pressing or sintering are discussed.

1.2.3 Chapter 4 - Formulating a Characteristic Time

Each criteria derived in chapters 2 and 3 can be mathematically interpreted as a boundary that separates the state space of a material into two regions. One region corresponds to the material prior to a transition in behavior, the other, after the transition. In this chapter the

focus is on the region prior to the transition. An attempt is made to develop a systematic approach to formulating a characteristic time for a state trajectory to cross the transition boundary, given an initial state. As in the previous chapters, the material behavior is assumed to be governed by coupled, simultaneous kinetic processes. The characteristic time is a function of the internal variables, process input variables, and material parameters. The characteristic time can aid the choice of processing inputs, such as temperature and strain rate for an extrusion process, by predicting the rate of approach to the transition.

The formulation of the characteristic time is shown, however, to be incomplete. Approaches for improvement are given. The approach is then applied to pore separation to highlight the unresolved issues.

1.2.4 Chapter 5 - Closing

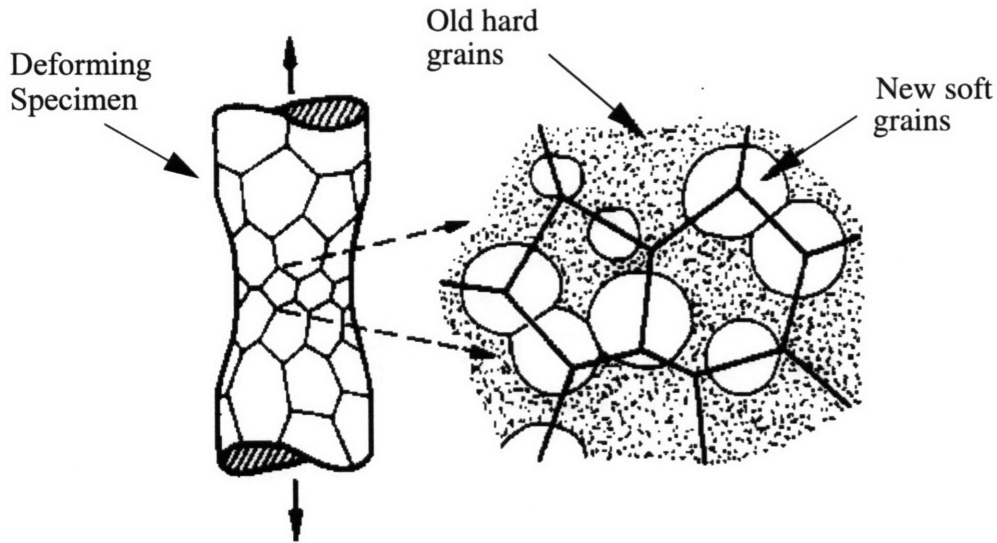
This chapter begins by discussing the main results of this work. Following this discussion, suggestions to improve the internal variable models and auxiliary functions are summarized. Finally, some preliminary work on how the models can be used in an adaptive control framework is presented.

CHAPTER 2 A Criterion for Dynamic Recrystallization

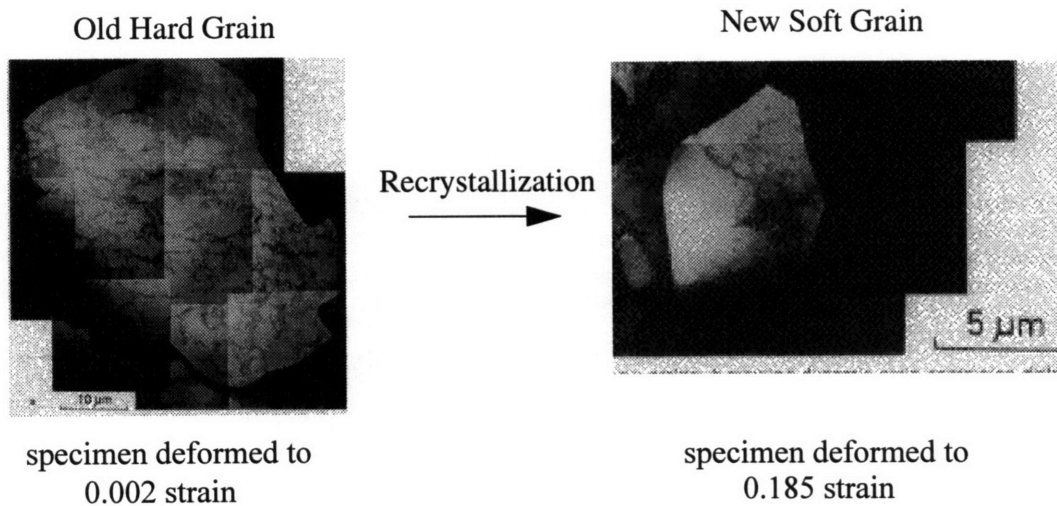
This chapter considers the phenomenon of dynamic recrystallization within a state variable, nonlinear system dynamics framework. Dynamic recrystallization is defined as a recrystallization process that occurs while a material experiences a nonzero strain rate. The effect of dynamic recrystallization on the evolution of a material's microstructure is characterized by waves of recrystallization replacing old, deformed grains with new grains having a relatively low dislocation density. Figure 2.1 illustrates this evolution in microstructure. The old grains are many times harder than the new grains owing to the much larger dislocation density in the old as compared to the new. The micrographs shown in the figure are from experiments by Sakai and Ohashi using pure nickel at a constant strain rate of 0.002 1/s and temperature of 923 K [15].

A common macroscopic effect of dynamic recrystallization on rate-dependent constitutive behavior is to introduce a maximum in the stress/strain response, with possible additional oscillations in the flow stress resulting from repeated cycles of recrystallization. Figure 2.2 shows representative oscillating stress/strain curves for OFHC copper at relatively high homologous temperatures [15]. A criterion to predict the peak in stress associated with dynamic recrystallization would be useful because an unexpected change in deformation resistance can complicate the control of hot working operations. The phenomenon is normally associated with low stacking fault energy materials that have a low rate of static and dynamic recovery, thereby permitting high dislocation densities and consequently high stored elastic internal energy densities to drive recrystallization.

The analysis presented here considers only the onset of dynamic recrystallization as manifested by the first peak in deformation resistance. The first peak is the maximum in the stress/strain curve where the deformation resistance begins to decrease with increasing



a) Schematic of microstructural evolution



b) Micrographs showing change in dislocation density

Figure 2.1 (a) Schematic of the microstructural evolution characterizing dynamic recrystallization, from Frost and Ashby [14]. (b) Micrograph on left shows an old, deformed grain with the numerous dislocation structures while the micrograph on the right shows a newly recrystallized grain with a relatively low dislocation density, from Sakai and Ohashi [15].

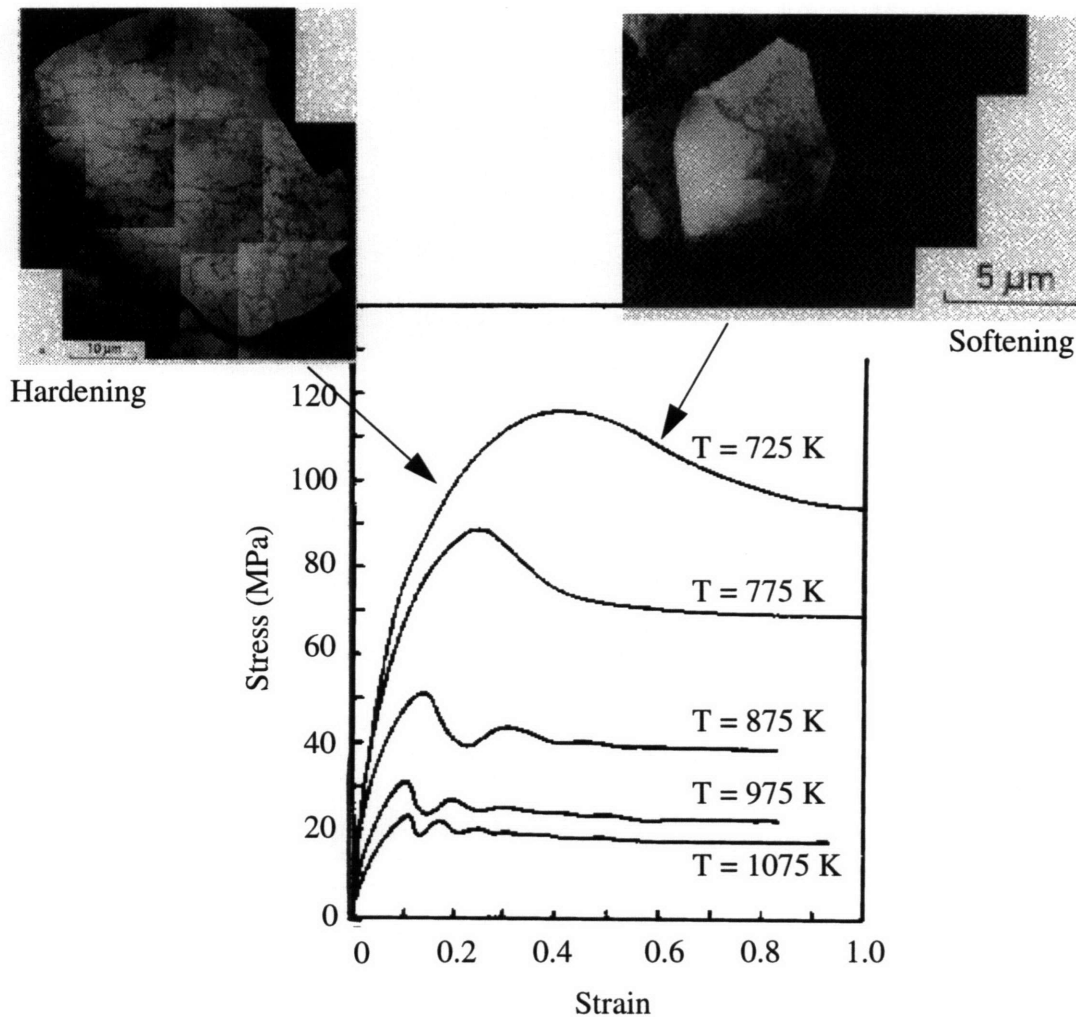


Figure 2.2 Oscillating stress/strain curves for OFHC copper deformed at 0.002 1/s strain rate and five different temperatures, from Blaz et. al [29]. Micrographs used only to roughly illustrate the linkage between the stress peak and the evolution in microstructure. The micrographs are the same as those shown in figure 2.1.

strain. At constant temperature and strain rate, this corresponds to the first peak in stress in the measured stress/strain response. The analysis does not attempt to predict the transition from single to multiple peak behavior, nor does it consider steady state grain sizes. As will be seen, modeling multiple peak behavior and steady state grain size is not needed to predict the first peak in stress as a consequence of dynamic recrystallization.

This chapter is organized as follows. Section 2.1 reviews previous research to develop a criterion for dynamic recrystallization. Section 2.2 starts with a description of the

general form of an internal variable model and then derives the internal variable model analyzed in this work. Section 2.3 uses numerical simulations to evaluate the performance of the model with parameter values for OFHC copper. Section 2.4 first presents a general approach to developing criteria for transitions in material behavior and then applies this general approach to derive a criterion for the peak stress associated with dynamic recrystallization. Section 2.5 evaluates the performance of the criterion given two sets of data for OFHC copper. This chapter ends with section 2.6 by discussing some implications and limitations of the criterion.

2.1 Previous Work to Develop a Criterion for Dynamic Recrystallization

Although criteria have been proposed to predict the onset of dynamic recrystallization, most if not all of these criteria are applicable under a limited set of operating conditions. Luton and Sellars [16] and Sakai and Jonas [17] define the onset of dynamic recrystallization via critical strain criteria. The oscillations in macroscopic stress/strain behavior are correlated with different threshold strains that represent the onset or completion of cycles of recrystallization. These critical strain measures are valid only under isothermal, constant strain rate conditions – conditions that are not frequently met during typical hot working processes such as rolling, forging, or extrusion. The shortcoming of a criterion based on strain derives from the inability of strain to represent the state of a hot-worked metal under nonsteady conditions. Strain is not a state variable at elevated temperatures since the microstructure continues to evolve through thermally-activated processes that continue in the absence of deformation. Other variables are therefore necessary to represent the true state of the material.

There appear to be two efforts to use scalar internal variable models to predict dynamic recrystallization. Sandstrom and Lagneborg [18] employed a model consisting of a dislocation density distribution and a variable representing volume fraction recrystallized. Their formulation is rational physically since there is certainly a distribution of dislocation densities within a given volume of deforming, recrystallizing metal. Sandstrom, however, does not consider the metal flow to be rate-dependent, which is non-physical. Adebajo and Miller [19] proposed a modification to Miller's MATMOD constitutive model [20] involving five internal variables consisting of an isotropic

deformation resistance, an anisotropic backstress, two solute strengthening variables, and a recrystallization variable representing the interfacial area of recrystallized material. They consider the dynamically recrystallizing material deformation to be rate-dependent. The Adebajo and Miller model is particularly intricate, however, involving over 20 scaling parameters. Both models considered the mechanical response of a dynamically recrystallizing material to large strain, and therefore included multiple cycles of recrystallization and evolution of grain size. Excellent reviews of dynamic recrystallization include those by Sakai and Jonas [17] and Cahn [21].

2.2 Internal Variable Model

In this section the general form of an internal variable model is shown, followed by a presentation of the internal variable model of kinetic process associated with dynamic recrystallization. The model of the kinetic processes associated with dynamic recrystallization is comprised of three nonlinear, first order, ordinary differential equations: dislocation density evolution, volume fraction recrystallization rate, and temperature evolution.

2.2.1 General form of an Internal Variable Model

A family of constitutive models of material behavior, called internal variable models, characterizes the coupling between macroscopic measures of material behavior, such as viscoplastic rate dependence, with microstructural evolution. Internal variables represent microstructural features; examples are dislocation density and grain size. The general form of an internal variable model is a system of first order, nonlinear, autonomous, ordinary differential equations [3], analogous to the state-space representation used by the system dynamics community to characterize dynamic systems [10]. The form of internal variable models makes them particularly suited to analysis using methods from nonlinear dynamics. Analysis of internal variable models by methods adapted from nonlinear dynamics presents an opportunity to investigate the kinetic processes associated with transitions in material behavior.

The complicated character of dynamic recrystallization is a convenient example to present the general form of an internal variable formulation, where the evolution of

multiple internal structure variables is defined via first order kinetic equations. An internal variable model takes the form:

$$\dot{s}_n = f_n[\dot{\epsilon}, T, s_1, \dots, s_m], \quad 1 \leq n \leq m \quad (2.1)$$

The internal variables s_n may be scalars or higher order, even-ranked tensors. The variables $\dot{\epsilon}$, strain rate, and T , temperature, are process variables and represent the nonstructure variables. The internal variables represent material microstructures such as dislocation density, grains size and obstacles. Process variables and internal variables taken together characterize the current state of the material. Internal and process variables represent state variables from a systems viewpoint in that knowledge of those state variables provides sufficient information to describe the particular phenomenon completely. They are not necessarily thermodynamic state variables.

Internal variable models, like other dynamical models, are frequently represented via a state-space formulation with the system dynamics modeled by a system of first order differential equations that can be both nonlinear and highly coupled. Consider a state vector

$$\underline{x} = [x_1, x_2, x_3, \dots, x_n] . \quad (2.2)$$

then the time history of this system is modeled by a set of dynamic functions

$$\dot{\underline{x}} = f(\underline{x}) \quad (2.3)$$

In this case the system dynamics are assumed not dependent on time (autonomous).

2.2.2 Internal Variable Model Analyzed in this Work

The model presented here assumes a scalar deformation and stress space, where tensorial variables such as stress and strain rate are assumed to be either single component states or are expressed in scalar magnitude equivalents. This formulation also assumes that the deformation field is homogeneous, and that dynamic recrystallization can occur at any spatial point within the material. Nuclei for heterogeneous nucleation are assumed to

be uniformly distributed throughout the material; deformation therefore continues uniformly throughout the bulk of the material. Dynamic recrystallization can cause oscillations in the microstructural state as waves of recrystallization “sweep” through a material. Here, however, only the onset of the first cycle of recrystallization is considered. The model proposed below is not adequate to represent the subsequent cycles of recrystallization, nor can it capture the three dimensional character of this cyclic material response.

Four state variables are proposed: ρ , dislocation density, v_r volume fraction recrystallized, $\dot{\epsilon}$, T . The first two state variables are internal variables representing the microstructural state. The last two variables measure the imposed processing conditions.

To place the material model within a state space representation, a system of first order differential equations characterizing the evolution of each state variable is required. The following sections present coupled equations based on simple models of dislocation density evolution, grain boundary migration, and energy balance. The equations have been non-dimensionalized for analytical convenience. The dynamic response of the equations remain unchanged.

Evolution equation for dislocation density

The evolution of dislocation density is a general form of the Bailey-Orowan relation, where the dislocation density varies through separate hardening and recovery rates:

$$\dot{\rho} = h[\dot{\epsilon}, T, \rho] - r(\rho, T) \quad (2.4)$$

The equation below combines the effect of hardening and dynamic recovery in a Voce term [22] and includes the effect of static recovery in a power law form used by both Prinz and Argon [23] and Nix and Gibeling [24]:

$$\dot{\rho} = \frac{A_1}{b} \sqrt{\rho} \left(1 - \frac{\rho}{\rho_{ss}} \right) \dot{\epsilon} - A_2 (b^2 \rho)^{m_1} \exp\left(\frac{-Q_{sd}}{kT}\right) \frac{v_c T_m}{b^2 T} . \quad (2.5)$$

Symbols used in equations in this chapter are defined at the end of this chapter. The

constant ρ_{ss} represents a steady state value of dislocation density in the absence of static recovery. Although several models for dynamic recovery have been proposed based on thermally-activated cross slip [24][25], this phenomenological form is selected since it matches hardening data well at strain rates associated with hot working procedures [3][26] while remaining simple analytically. The steady state dislocation density ρ_{ss} can be represented by:

$$\rho_{ss} = \tilde{\rho} \left[\frac{\dot{\epsilon}}{v_{dm} A_3} \exp\left(\frac{Q_{dr}}{kT}\right) \right]^{m_2}. \quad (2.6)$$

For moderate strain rates above 10^{-3} s^{-1} the effect of static recovery can be neglected and equation (2.6) reduces to one that incorporates only hardening and dynamic recovery:

$$\dot{\rho} = \frac{A_1}{b} \sqrt{\rho} \left(1 - \frac{\rho}{\rho_{ss}} \right) \dot{\epsilon}. \quad (2.7)$$

Evolution equation for volume fraction recrystallized grains.

This evolution equation assumes an initial density of recrystallization nuclei. A constant site density was assumed since Roberts et. al. [27] suggests that existing nuclei are first exhausted (site saturation) before new nuclei grow. Site saturation does not appear to occur for $v_r \leq 0.3$, therefore the assumption of constant site density is reasonable for low values of v_r . It also assumes that the nuclei grow in a hemispherical manner, growing into a deformed grain with a given dislocation density. The grain boundary velocity relation follows the treatment of Doherty [28], where the grain boundary mobility is a function of the activation barrier to atomic migration across grain boundaries and the difference in free energy between the deformed and dislocation free grains.

$$\dot{v}_r = 3A_5 N_s C_{ac} b v_{gb} v_r^{2/3} \exp\left(\frac{-Q_{gb}}{kT}\right) \left(\frac{\Delta G \Omega}{kT}\right) (1 - v_r). \quad (2.8)$$

Here, the change in free energy per unit volume associated with recrystallization is assumed equal to the reduction in elastic strain self-energy at a given dislocation density:

$$\Delta G = \frac{\mu b^2}{2} \rho. \quad (2.9)$$

Here, μ is the temperature-dependent shear modulus [14] and b is the magnitude of the burgers vector. Changes in volumetric strain energy and configurational entropy between the deformed and recrystallized conditions are assumed negligible. Additionally, experimental data indicates that the vast majority of recrystallizing grains do not impinge before causing sufficient recrystallization to reach the first peak in the stress/strain response [29]. The effect of impingement is approximated by adding the $(1 - \nu_r)$ term in the rate equation. The effect of this term at the peak stress is less than 20%, however. The effect of impurities such as precipitates or solute concentration on grain boundary mobility may be included as described by Cahn [21]. Insufficient data was available on the materials systems described later to include impurity effects explicitly. A relatively pure material was selected for calibration of the model, thereby reducing the influence of precipitates or solutes.

Evolution equation for temperature.

The temperature evolution equation results from an energy balance:

$$\dot{T} = \frac{1}{c_p \rho_d} \left(k_{th} \frac{d^2 T}{dx^2} + \omega \dot{\epsilon} \sigma + \nu_r \frac{\mu b^2}{2} \rho \right). \quad (2.10)$$

The last term represents the conversion of elastic energy into thermal energy as the high dislocation density metal recrystallizes. Isothermal conditions yield only the second two terms of the above equation.

Evolution equation for strain rate.

The strain rate is assumed to be imposed externally by the deformation process. Therefore, the evolution equation is taken as an imposed strain rate history:

$$\dot{\epsilon} = f(t) \quad (2.11)$$

such that

$$\ddot{\epsilon} = \frac{d}{dt} f(t) . \quad (2.12)$$

2.3 Evaluation of the Performance of the Internal Variable Model

The performance of the model was evaluated by comparing numerical simulations of the evolution of ρ and v_r to experimental data. The simulations required numerical values for the parameters in equations (2.5) and (2.8), and initial conditions of ρ and v_r . Numerical values for the parameters, other than the scaling parameters (A_1, A_2, A_3, A_5) were obtained from published data for OFHC copper [14][23][24][30][31]. Table 2.1 lists these parameter values.

As previously mentioned, the nucleation site density was assumed constant [27]. The nucleation site density value was chosen as an average value for single phase, high purity polycrystalline metals based on classical theory of nucleation [32]. Numerical values for the scaling parameters A_1, A_2, A_3 and A_5 were obtained by isolating each element of the model in which a scaling parameter appeared, and then fitting the isolated function to experimental data of the appropriate kinetic process. Fitting of scaling constants was performed outside the range of conditions where dynamic recrystallization occurs. The scaling parameters were therefore not chosen to fit the response of the entire model to dynamic recrystallization data.

The scaling parameter A_1 modifies the function in the model that describes the rate of dislocation density increase due to athermal hardening:

$$\dot{\rho}_{\text{hard}} = \frac{A_1}{\rho} \sqrt{\rho} \dot{\epsilon} . \quad (2.13)$$

Dividing the expression above by $\dot{\epsilon}$ gives the increase in dislocation density for an infinitesimal increment in strain:

$$\frac{d\rho}{d\varepsilon} = \frac{A_1}{C} \sqrt{\rho} . \quad (2.14)$$

To first order, the increase in dislocation density for an infinitesimal increment in strain can be derived from first principles [35] as:

$$\frac{d\rho}{d\varepsilon} = \frac{1}{bC} \sqrt{\rho} \quad (2.15)$$

where C is a constant equal to the mean number of dislocation line-lengths a dislocation will traverse before being annihilated [23]. Comparing these two expressions results in a numerical value for A_1 :

$$A_1 = \frac{1}{C} . \quad (2.16)$$

The value $C = 100$ was chosen, which is supported by Nix and Gibeling [24].

The term A_2 scales the function in the model that represents the rate of dislocation decrease due to static recovery, reproduced below.

$$\dot{\rho}_{\text{static}} = -A_2 (b^2 \rho_{\text{static}})^{m_1} \exp\left(\frac{-Q_{sd}}{kT}\right) \frac{v_c T_m}{b^2 T} \quad (2.17)$$

Collecting all constants and taking $m_1 = 3$ (as given by Prinz and Argon [23]) results in:

$$\dot{\rho}_{\text{static}} = -A_2 v_c b^4 \frac{T_m}{T} \exp\left(\frac{-Q_{sd}}{kT}\right) \rho_{\text{static}}^3 . \quad (2.18)$$

A relation of the same form has been proposed by Prinz and Argon [23]:

$$\dot{\rho}_{\text{static}} = -2K_3 \rho_{\text{static}}^3 \quad (2.19)$$

Parameter	Value
b	2.56×10^{-10} m
C_{ac}	0.5
k	1.38×10^{-23} J/K
m_1	3.0
m_2	0.07
n	5.8
N_s	1.0×10^{16} m ⁻³
Q_{dr}	117×10^3 J/mol
Q_g	176×10^3 J/mol
Q_{gb}	104×10^3 J/mol
Q_{sd}	117×10^3 J/mol
T_m	1356 K
v_c	1.0×10^{13} s ⁻¹
v_{dm}	1.0×10^{11} s ⁻¹
v_{gb}	1.0×10^{13} s ⁻¹
μ	42.1×10^9 Pa
$\tilde{\rho}$	1.0×10^{15} m ⁻²
Ω	1.18×10^{-29} m ³

Table 2.1 Parameter values for OFHC copper.

where

$$K_3 = \frac{\sqrt{2}}{\pi(1-\nu)} \left(A_c D_c \right) \left(\frac{\mu\Omega}{kT} \right) \quad (2.20)$$

and

$$A_c D_c = A_c D_{oc} \exp\left(\frac{-Q_{sd}}{kT}\right). \quad (2.21)$$

ν is Poisson's ratio, A_c is the dislocation core cross-sectional area, and D_c is the dislocation core diffusion constant. This expression was found to fit experimental data in [23] well. The two expressions, (2.18) and (2.19), when compared yield a relation for A_2 :

$$A_2 = \frac{2\sqrt{2}\mu\Omega \left(A_c D_{oc} \right)}{\pi(1-\nu) k\nu_c b^4 T_m}. \quad (2.22)$$

Prinz and Argon [23] give a numerical value for K_3 computed for aluminum. A_2 was computed for OFHC copper parameter values from [14]. The resulting relation for the scaling factor A_2 was then inserted in the simulation code, where μ is temperature-corrected.

The term A_3 appears in the model as a scaling factor on the phenomenological expression for the temperature and strain rate dependence of the saturation dislocation density:

$$\rho_{ss} = \tilde{\rho} \left[\frac{\dot{\epsilon}}{\nu_{dm} A_3} \exp\left(\frac{Q_{dr}}{kT}\right) \right]^{m_2} \quad (2.23)$$

A_3 was evaluated numerically by assuming that at room temperature (300K), $\rho_{ss} = \tilde{\rho}$. The expression above can then be solved for A_3 directly:

$$A_3 = \frac{\dot{\varepsilon}}{v_{dm}} \exp\left(\frac{-Q_c}{300k}\right). \quad (2.24)$$

This expression was inserted into the simulation code to compute numerical values of A_3 .

The term A_5 scales the relation of the evolution of volume fraction recrystallized in the dynamic recrystallization model:

$$\dot{v}_r = 3A_5 N_s C_{ac} b v_{gb} v_r^{2/3} \exp\left(\frac{-Q_{gb}}{kT}\right) \left(\frac{\mu b^2 \Omega \rho}{2kT}\right) (1 - v_r). \quad (2.25)$$

The numerical value for A_5 was computed by evaluating this expression from data presented by Blaz et. al. in [29] on the evolution of volume fraction recrystallized. A numerical value for the time rate of change of fraction recrystallized, \dot{v}_r , was estimated by drawing a tangent at a point on a curve in figure 7 in [29] that relates total volume fraction recrystallized to strain. The point chosen corresponds to the first peak in stress. For a small change in v_r , a corresponding increment in strain (related to time since the experiment was performed at a constant strain rate) was determined. Dividing the increment in volume fraction recrystallized by the increment in time approximates \dot{v}_r near a point (v_r, ε) on the curve. The numerical value of the dislocation density for this calculation was the value of the steady state dislocation density, 10^{13} m/m^3 , given by equation (2.6) using the temperature and strain rate from figure 7 in [29].

Initial conditions for ρ and v_r to start the simulation were chosen from a range of values for annealed OFHC copper to duplicate experimental initial conditions. Initial dislocation density was therefore set at 10^{10} m/m^3 . The initial value of the volume fraction recrystallized was based on a computation of the volume of a single nucleus, containing about 100 atoms, summed over the assumed number of nucleation sites per cubic meter. The result of this computation was an initial volume fraction recrystallized of 10^{-11} .

There is a critical absence of appropriate physical data for calibrating internal variable models for dynamic recrystallization. There appears to be no single investigation that has

measured dislocation densities, volume fraction recrystallized material, nucleation site densities, and flow stress data for a single material, at any one temperature and strain rate, much less over a range of processing conditions. The data that does exist are results from constant temperature, constant true strain rate experiments [16][17][29]. Rigorous validation of the model presented in this article or other models is thus difficult, if not impossible, without appropriate data on the state of the material throughout dynamic recrystallization. The material constants used to calibrate the model therefore involved inevitable compromises. Continued progress in coupling structure variables to dynamic recrystallization will require such data, not just for isothermal constant strain rate conditions, but also for more complicated temperature and strain rate histories.

Nevertheless, it was possible to evaluate the model by choosing a model material for calibration and limiting the simulations to the isothermal, constant strain rate case. OFHC copper was selected for the comparison since the largest amount of test data on structure was available for this metal. Numerical integration of the internal variable model for the isothermal, constant strain rate case was executed by a commercially available fourth order Runge-Kutta subroutine [37]. Data showing peak strains for OFHC copper under isothermal, constant strain rate conditions is available [29] for a quantitative comparison of the internal variable model. Results from numerically integrating the model for a constant temperature of 775 K and constant strain rate of 0.002 s^{-1} are plotted in figure 2.3. Above a strain of approximately 0.5, the rate of change in dislocation density decreases as the dislocation density approaches the saturation value. Likewise, as the volume fraction exceeds approximately 0.4, the rate of change of volume fraction recrystallized switches from positive to negative denoting the asymptotic limit of volume fraction at 1.0. The model simulates the dislocation density of unrecrystallized grains only, therefore, the dislocation density at large strains does not represent the average dislocation density of the material.

Figure 2.4 shows the numerical integration of the model plotted in state space where the dislocation density has been normalized by the steady state dislocation density ρ_{ss} , for a constant strain rate of 0.002 s^{-1} and three different temperatures: 675 K, 775 K, 975 K. The normalization of the dislocation density curves by ρ_{ss} each used a value for ρ_{ss}

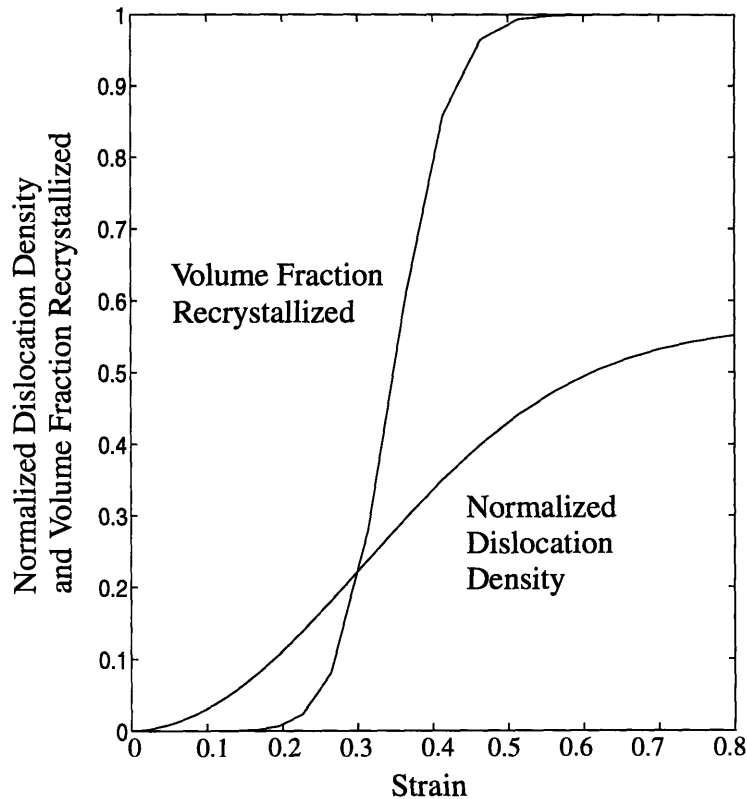


Figure 2.3 Simulated time-evolution in dislocation density (normalized by the steady state dislocation density, ρ_{ss}) and volume fraction recrystallized for OFHC copper at 775 K and a strain rate of 0.002 s^{-1} .

corresponding to one of the three temperatures in turn. The figure shows that for increasing temperature the normalized saturation dislocation density decreases from 0.85 to 0.1. This is expected since the hardness of a material decreases with temperature, i.e. the processes of annealing are thermally activated.

Figure 2.4 shows the model for a temperature of 775 K and two different strain rates; 0.02 s^{-1} and 0.002 s^{-1} . Decreasing the strain rate yields a decrease in the normalized saturation dislocation density. This behavior is anticipated because of the decrease in dynamic hardening as strain rate decreases; i.e. dislocations are generated at a reduced rate.

However, the phase planes in figures 2.4 and 2.4 also lack an anticipated behavior. The trajectories in figure 2.4 suggest that the stability structure of the system given by

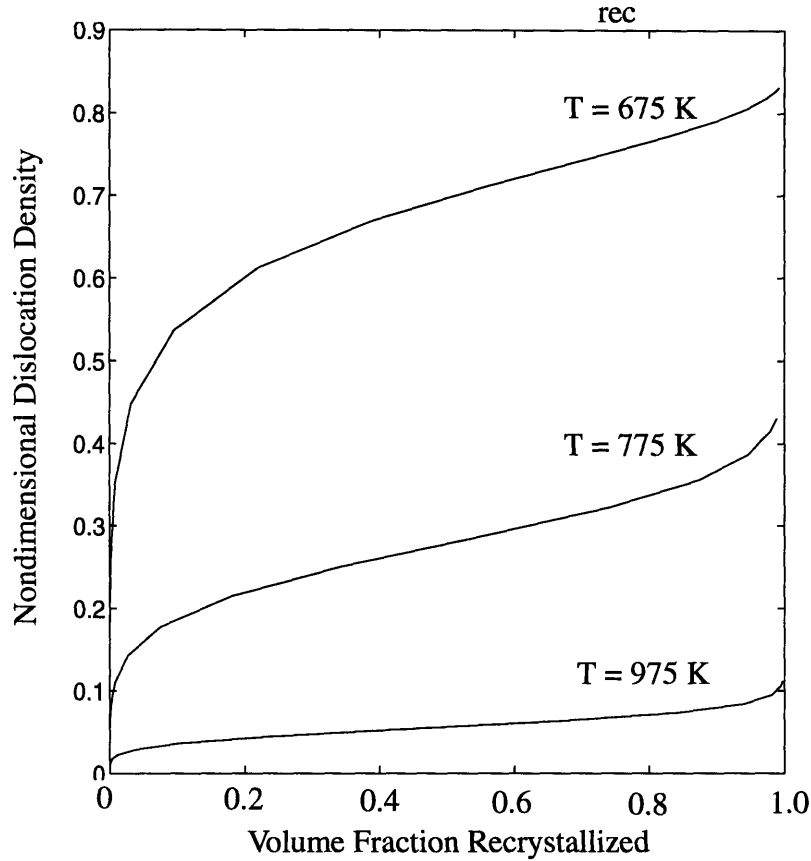


Figure 2.4 State trajectories showing the dislocation density (nondimensionalized by the steady state dislocation density, ρ_{ss}) and volume fraction recrystallized for OFHC copper at a strain rate of 0.002 s^{-1} and three different temperatures; 675 K, 775 K, 975 K

equations (2.5) and (2.8) does not contain a boundary that would indicate a transition in microstructural evolution resulting in the first peak in the stress response of copper. The first peak in stress would occur well before a volume fraction recrystallized of 0.50 [21]. Therefore, before proceeding further, the stability structure of this model should to be examined in detail. Physically, the analysis will be limited to the region in the state space given by $\mathfrak{R} = \{ \frac{\rho}{\rho_{ss}}, v_r / 0 < \frac{\rho}{\rho_{ss}} \leq 1.0, 0 < v_r < 1.0 \}$. It can be easily verified that each ODE in the model is continuous in this region and hence solutions are guaranteed to exist and be unique. Further, the system has two nullclines, $v_r = 1$ and $\frac{\rho}{\rho_{ss}} = 1$ (when static recovery is neglected). The system's one fixed point is $v_r = \frac{\rho}{\rho_{ss}} = 1$.

The rates for dislocation evolution and volume fraction recrystallization given by the model are positive semi-definite in \mathfrak{R} . Therefore, $\frac{\rho}{\rho_{ss}}$ and v_r increase monotonically. No

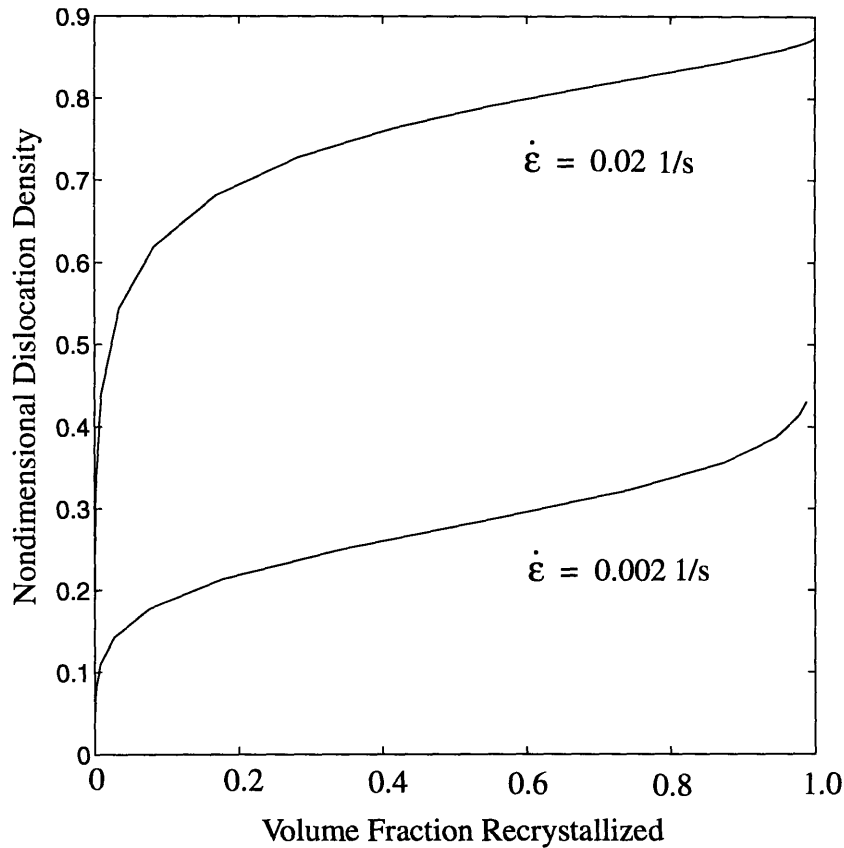


Figure 2.5 State trajectories of the dislocation density (nondimensionalized by the steady state dislocation density, ρ_{ss}) and volume fraction recrystallized for OFHC copper at 775 K and two strain rates; 0.02 and 0.002 s^{-1} .

limit cycles exist within \mathfrak{R} since the vector field within \mathfrak{R} is a gradient field, as suggested by the trajectories in figures 2.4 and 2.4. Figures 2.4 and 2.4 indicate that the fixed point $v_r = \frac{\rho}{\rho_{ss}} = 1$ is an attracting node. This stability structure does not change over a wide range of physically meaningful parameter values. The conclusion is that the model does not have a stability structure containing a boundary, such as a boundary manifold or a limit cycle, that might correspond to the first peak. The next section will show how this model can still be used to derive a boundary in state space that corresponds to the first peak in stress of pure metals.

2.4 Derivation of a Criterion for Dynamic Recrystallization

Once a particular system is modeled using the state-space formalism, a collection of analytical methods (phase plane representations, perturbation methods, bifurcation

analysis, Lyapunov methods, invariant set theorems) [8][9][10] becomes available to investigate the dynamics of that system model. As was shown in the previous section, the model does not contain a boundary that would indicate a change in the evolution of the microstructure that corresponds to the first peak in stress. This section shows how such models can still be used to form a criterion for a transition in material behavior.

The approach is given in two sections. First, an expression of a boundary in the state space of the material which corresponds to the transition in material behavior is formulated. Second, a characteristic time-to-transition as a function of material parameters and initial conditions is derived. In each section the approach is described in general and then followed by an application to the specific case of pore separation from grain boundaries during hydrostatic, high temperature consolidation processes.

2.4.1 A General Approach to Formulating a Criterion

The approach begins by choosing a scalar-valued function Φ of the system's state variables, $\Phi = \Phi[z_1, z_2, \dots, z_n]$, with continuous first partial derivatives. Φ is C^1 and maps the values of the state variables, as they evolve with time, to \mathbb{R}^+ . Φ should undergo a distinct transition coinciding with the onset of the transition in the material behavior. The transition can be a zero crossing, a minima or a maxima for example. The system of equations governing the evolution of the state variables need not represent the system behavior after the transition. Kinetics equations governing the system behavior either before or after the transition can be used to develop a criterion using this approach.

Corresponding to the distinct transition in Φ there exists a boundary in the state space of the material denoting those states where the transition occurs. The boundary may or may not form a bounded region. If the boundary does not form a bounded region, the boundary combined with physically motivated limits on the values of the states constructs a bounded region.

An example of a suitable function Φ is given in the next section. In this section, Φ is a scalar characterization of the stress response of a rate-dependent material. The stress response of a rate-dependent material has a distinct peak as a result of the onset of dynamic recrystallization. The peak in the stress response is the desired transition in Φ . A peak in the stress response is stated equivalently by a change in the sign of $\frac{d\Phi}{dt}$, from

negative to positive. The region in state space described by $\{z, \dot{z} \text{ such that } \dot{\Phi} = \nabla \bullet z < 0\}$ shows the states and their derivatives that avoid the first peak in stress associated with dynamic recrystallization. Substituting the ODE's from the internal variable model for \dot{z} in this expression leads to a criterion solely in terms of the state variables.

2.4.2 The General Approach Applied to Dynamic Recrystallization

The general method outlined in the previous section is now applied to the internal variable model presented in section 2.2. Since the model is valid in representing the first peak in flow stress, but is not valid for subsequent peaks, the criterion is only valid for the first peak in flow stress.

To begin the analysis, a standard, nondimensionalized power law representation of viscoplastic strain rate [33]:

$$\dot{\epsilon} = A_4 v_{dm} \left[\frac{\sigma}{b \mu \sqrt{\rho} [1 - v_r]} \right]^n \exp\left(\frac{-Q_g}{kT}\right) \quad (2.26)$$

is inverted to solve for the stress response:

$$\sigma = \left[\frac{1}{A_4 v_{dm}} \dot{\epsilon} \exp\left(\frac{Q_g}{kT}\right) \right]^{1/n} \mu b \sqrt{\rho} (1 - v_r) \quad (2.27)$$

and taken as the summarizing function Φ described in section 2.4.1.

The microstructural state of the material enters into the rate equation, equation (2.26), as a scaling parameter for the applied stress. The square root of the dislocation density is modified by the volume fraction unrecrystallized, $(1 - v_r)$, to obtain an equivalent effective dislocation density. This can also be interpreted as a volume average of deformation resistance, where the deformation resistance of the recrystallized metal is small compared to the unrecrystallized metal, so that it can be ignored.

The stress response, equation (2.27), is scalar-valued and has continuous first partial derivatives. The activation energy Q_g represents an average of the thermally-activated

processes contributing to dislocation motion. For standard climb-controlled power law behavior, Q_g is expected to be very close to the activation energy for self-diffusion Q_{sd} .

Stress was selected as the summarizing function for several reasons. First, the macroscopic manifestation of dynamic recrystallization during rate-dependent deformation is the presence of a peak stress followed by softening. The peak stress can be considered as a point of neutral stability, suggesting that stress could function as a criterion. Similarly, the peak stress represents the macroscopically measurable quantity frequently used to indicate the onset of dynamic recrystallization. Second, there is a large body of literature describing the variation of peak stress with temperature and strain rate available for correlation with a summarizing function based on stress. Third, the flow equation expressed with stress as the dependent variable, σ , directly correlates with rate-dependent deformation processes. The power law relation has been explained via thermally-activated recovery processes leading to power law creep [34]. Other flow equations are also possible, including that proposed by Kocks, Argon, and Ashby [30] to represent the kinetics of dislocation glide. In addition, one may interpret dynamic recrystallization as a transition from an increasing energy state to a decreasing one. Increasing stress represents an accumulation of dislocation density and elastic strain energy that then decreases once dynamic recrystallization reaches a certain value.

Continuing with the derivation of a criterion, the derivative of the stress response is:

$$\dot{\sigma} = \frac{\partial \sigma}{\partial \rho} \frac{\partial \rho}{\partial t} + \frac{\partial \sigma}{\partial v_r} \frac{\partial v_r}{\partial t} + \frac{\partial \sigma}{\partial T} \frac{\partial T}{\partial t} + \frac{\partial \sigma}{\partial \dot{\epsilon}} \frac{\partial \dot{\epsilon}}{\partial t} \quad (2.28)$$

Substituting for the partial derivatives gives

$$\dot{\sigma} = \sigma \left[\frac{1}{2\rho} \dot{\rho} - \frac{1}{[1 - v_r]} \dot{v}_r + \frac{Q_g}{nkT^2} \dot{T} + \frac{1}{\dot{\epsilon}n} \ddot{\epsilon} \right]. \quad (2.29)$$

For the assumption of scalar stress states, σ takes positive values only, $\sigma > 0$. Therefore a peak in stress is given by:

$$\left[\frac{1}{2\rho} \dot{\rho} - \frac{1}{[1-v_r]} \dot{v}_r + \frac{Q_g}{nkT^2} T + \frac{1}{\dot{\epsilon}n} \ddot{\epsilon} \right] = 0. \quad (2.30)$$

For constant temperature, constant strain rate conditions, the criterion simplifies to:

$$\frac{1}{2\rho} \dot{\rho} - \frac{1}{[1-v_r]} \dot{v}_r = 0. \quad (2.31)$$

Equation (2.31) will be referred to as the criterion for the remainder of this chapter. Qualitatively, according to this criterion, a peak in stress is a consequence of the dynamic interaction between the rate of dislocation accumulation and the rate of recrystallization, modified by the individual contribution of dislocation density and recrystallized volume fraction. Although this makes sense intuitively, I believe that the criterion represents the first criterion for dynamic recrystallization that makes the interaction of internal structure explicit. Sandstrom and Lagneborg [18] alluded to this interaction, but did not attempt any representation of this criterion. The first peak in flow stress as a consequence of dynamic recrystallization will occur when the system internal states (ρ, v_r) first result in the equation (2.31) being satisfied.

Substitution of the rate equations for the dislocation density ρ and volume fraction recrystallized v_r produces a criterion based on the state variables alone:

$$\frac{A_1}{2b\sqrt{\rho}} \left(1 - \frac{\rho}{\rho_{ss}} \right) \dot{\epsilon} - 3A_5 N_s C_{ac} b v_{gb} v_r^{2/3} \exp\left(\frac{-Q_{gb}}{kT}\right) \left(\frac{\mu b^2 \rho \Omega}{2kT} \right) = 0. \quad (2.32)$$

where static recovery has been neglected in the evolution equation of dislocation density. This criterion for peak stress is different from those previously proposed for dynamic recrystallization in that it depends only on internal structure (ρ, v_r) and operating conditions $(\dot{\epsilon}, T)$. Strain, which is neither a state variable nor valid in nonisothermal, nonsteady conditions, is not included in the criterion. Solving equation (2.32) for v_r yields:

$$v_r = \left[\frac{\frac{A_1}{b\rho^{3/2}} \left(1 - \frac{\rho}{\rho_{ss}}\right) \dot{\epsilon}}{3A_s N_s C_{ac} b v_{gb} \exp\left(\frac{-Q_{gb}}{kT}\right) \left(\frac{\mu b^2 \Omega}{kT}\right)} \right]^{3/2} \quad (2.33)$$

This expression plotted in the ρ, v_r state space, as a function of temperature and strain rate, can be used to produce a processing envelope that can assist the planning of component fabrication processes such as hot rolling. In the next section such uses of equation (2.33) will be discussed.

2.5 Evaluation of the Performance of the Criterion

The criterion was partially validated by comparison to existing data. Predictions of the first peak in flow stress by the criterion can be compared to experimental data under constant temperature, constant strain rate conditions. The experimental data required to examine the criterion, equation (2.31), are values of the internal variables and their rates of change. Alternatively, equation (2.32) could be used to verify the criterion based on structure data alone. As previously mentioned, the necessary data to validate equations (2.31) or (2.32) directly has not been found. Instead, the rate equations were numerically integrated for $\rho(t)$ and $v_r(t)$ and the criterion was tested using the simulated values of ρ and v_r . The code was structured such that the evolution of ρ and v_r was allowed to proceed until the criterion changed sign from positive to negative, i.e. the stress reaches a peak. Equivalently, the criterion is satisfied by the numerical values of the rate of dislocation accumulation and the rate of recrystallization, modified by the individual contribution of dislocation density and recrystallized fraction. As one would expect, the criterion predicts the first peak in stress as a consequence of dynamic recrystallization before dislocation density reaches its saturation value. Peak stress and strain data are available for constant strain rate conditions, therefore the performance of the criterion was evaluated by comparing the peak strain predicted by the simulation with peak strain from experiments.

Results of the criterion's ability to predict the peak stress is shown in figure 2.6 using experimental data from Blaz et. al. [29] for OFHC copper. The experimental values have

vertical bands for peak strain due to the reported variation in peak strain for various initial grain sizes. As mentioned earlier, nucleation site density was chosen as a more

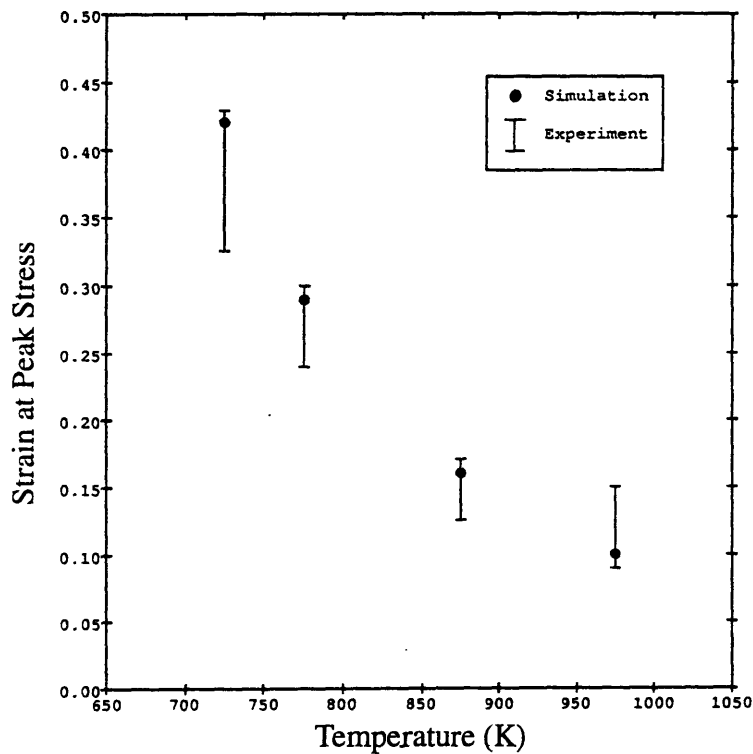
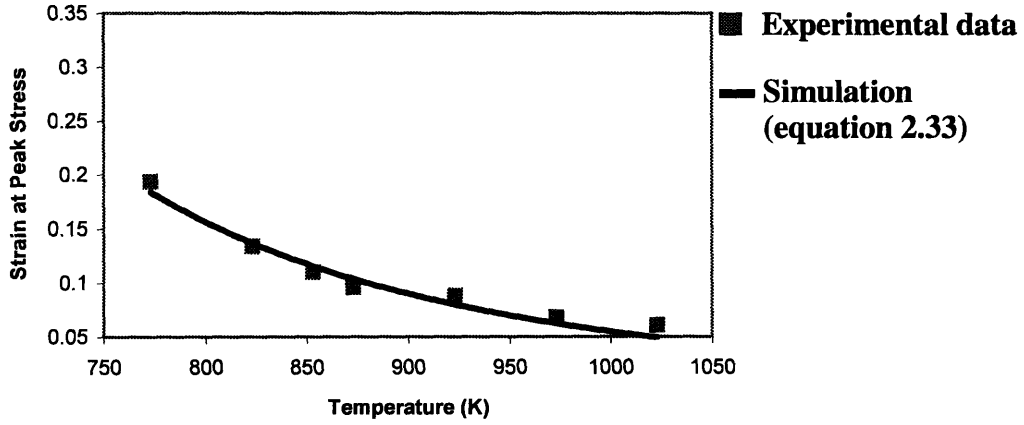


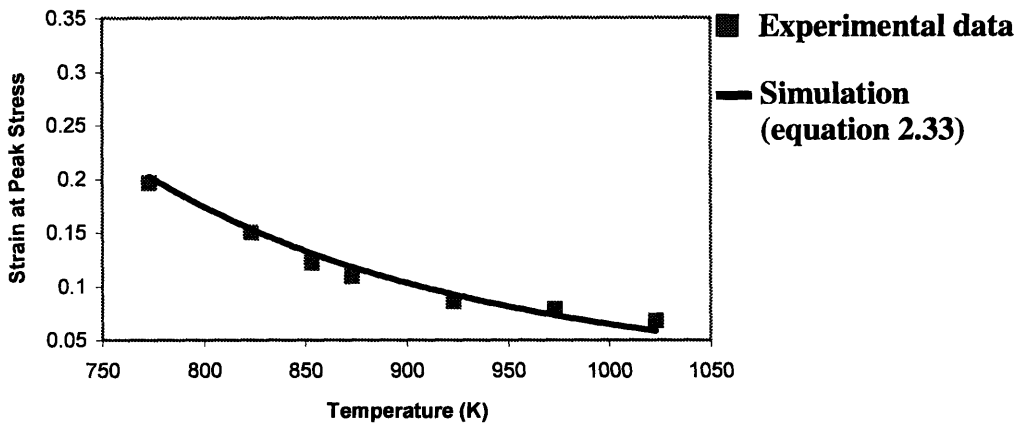
Figure 2.6 Comparison of strain at peak stress as a function of temperature. Points are predicted strains using the model and the criterion. Vertical bars show the variation in the strain at peak stress reported by Blaz et. al. [29] due to variations in the initial grain size.

fundamental parameter in the model rather than initial grain size. By assuming a constant nucleation site density an average initial grain size is implied. The criterion fits this data well and appears to capture the temperature dependence of dynamic recrystallization.

More results of the criterion's ability to predict the peak stress are shown in figures 2.7 and 2.7 using experimental data from Luton [40] for OFHC copper. There were no error bars given for this data. The data in each plot in figures 2.7 and 2.7 is for a constant strain rate. The data presented in figure 2.6 is for a strain rate between the low and high strain rates of figures 2.7 and 2.7. These figures indicate that the criterion captures the temperature dependence of dynamic recrystallization but shows departure from the experimental data for variations in strain rate.

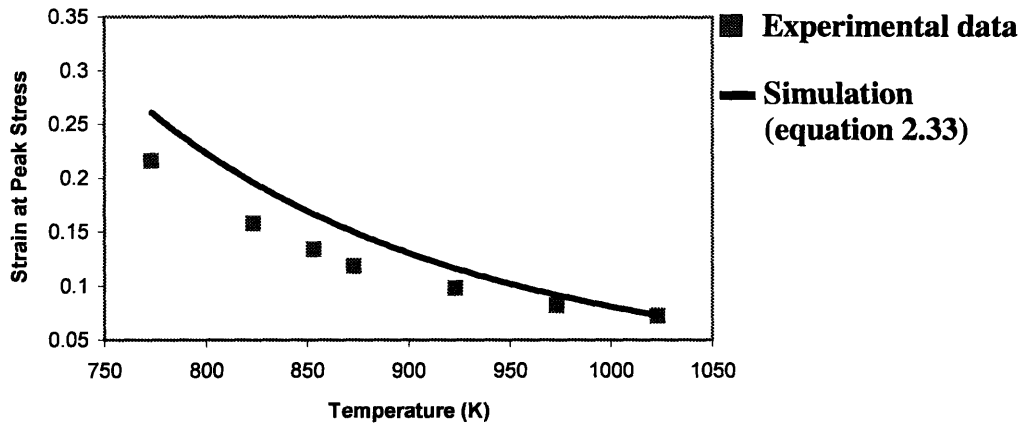


a) Strain rate = 0.00049 1/s

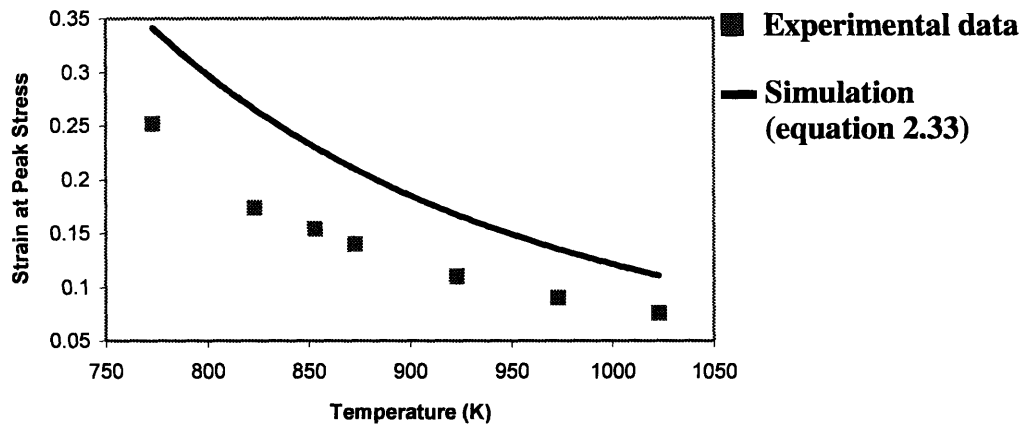


a) Strain rate = 0.00081 1/s

Figure 2.7 Comparison of strain at peak stress as a function of temperature. Curved line is the predicted strain using the model and the criterion. Points are experimental data from Luton [40] for OFHC copper. Plot (a) is for 0.00049 s^{-1} strain rate and plot (b) is for 0.00081 s^{-1} strain rate.



a) Strain rate = 0.0016 1/s



a) Strain rate = 0.0049 1/s

Figure 2.8 Comparison of strain at peak stress as a function of temperature. Curved line is the predicted strain using the model and the criterion. Points are experimental data from Luton [40] for OFHC copper. Plot (a) is for 0.0016 s^{-1} strain rate and plot (b) is for 0.0049 s^{-1} strain rate.

2.6 Discussion of Implications of the Criterion

It should be emphasized that this chapter is not highlighting a dramatically new model for dynamic recrystallization. Instead, it presents an analysis methodology for evaluating the onset of dynamic recrystallization. The methodology is not limited to the model presented in this paper, nor is it necessarily limited to the physical process of dynamic recrystallization. This approach, in the case of dynamic recrystallization, permits evaluation of aspects of the process that have not been previously considered, particularly since it uses only microstructural state variables instead of strain that has no microstructural analogue. The criterion proposed here is therefore dramatically different from previously proposed measures for the onset of dynamic recrystallization.

The behavior of the criterion reflects the kinetic processes represented by the model. Figure 2.9 plots the numerical value of the criterion versus strain for the same temperature and strain rate as figure 2.6. The vertical axis is the numerical sum of the terms on the left

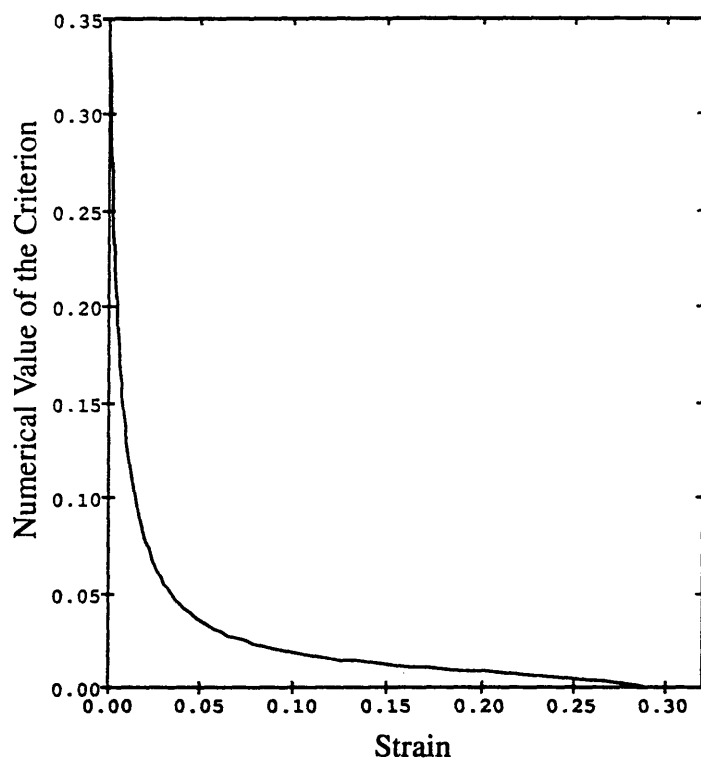


Figure 2.9 Numerical value of the criterion as a function of strain for isothermal constant strain rate conditions ($T = 775$ K, $\dot{\epsilon} = 0.02$ 1/s).

hand side of the criterion. The point where the numerical value of the criterion crosses the strain axis denotes the first peak in stress. The criterion can be interpreted as the evolution of the copper state trajectory towards the first peak in stress. For values of strain below 0.05 the criterion is dominated by the dislocation and dislocation rate. With increasing strain, the rate of volume fraction increases and the rate of increase of dislocation density decreases. For strain values approaching the peak strain, the value of the criterion shows a dependence on both the dislocation density term and the volume fraction recrystallized term. The criterion predicts what is qualitatively understood: namely, the kinetic processes at the first peak in stress are coupled and multivariable.

Figure 2.10 is an example of how the criterion can be used to produce a processing envelope. It shows a plot of the criterion for isothermal, constant strain rate conditions. The state space is defined by ρ and v_r . The curve sloping to the right marks the boundary of the domain of attraction for the case where $T = 775\text{K}$ and $\dot{\epsilon} = 0.002 \text{ s}^{-1}$. The boundary was generated by solving equation (2.33) for v_r as a function of ρ . The state trajectory is the result of a simulation using the internal variable model. The simulation was terminated when the criterion was satisfied. The point where the state trajectory crosses the boundary marks the first peak in stress due to dynamic recrystallization.

Figure 2.10 shows another example of how the criterion can be used to make a processing envelope. The figure shows the strain at peak stress as a function of temperature and strain rate assuming isothermal, constant true strain rate conditions. Figure 2.10 is a composite of many model simulations for OFHC copper that shows this dependence on temperature and strain rate. The volume below the surface depicted in the figure gives those temperatures, strain rates, and strains that avoid the first peak in flow stress as a consequence of dynamic recrystallization for OFHC copper. The contour lines are constant strain contours. The volume qualitatively duplicates experimental results: the strain at peak stress increases both with decreasing temperature and increasing strain rate. The jagged edge at the upper boundary of the volume is due to discrete integration steps. Figure 2.10 represents a constant strain rate slice of this surface.

The internal variable model for isothermal, constant strain conditions showed sensitivity to variations in key parameters. Sensitivity was measured by comparing values

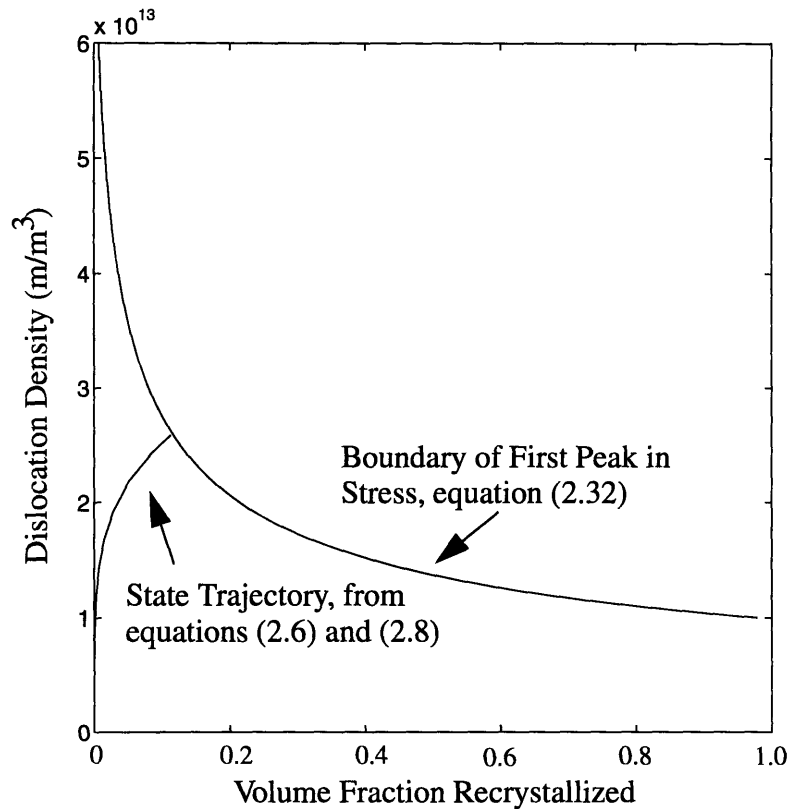


Figure 2.10 Simulated state trajectory for $T = 775$ K and $\dot{\epsilon} = 0.002$ 1/s, until intersection with the boundary denoting the first peak in stress, given by equation (2.32).

of volume fraction recrystallized and strain at peak stress to values reported Blaz et. al. in [29] for 4 different temperatures (725K, 775K, 875K, and 975K) at a constant strain rate of 0.002 s⁻¹. The model is more sensitive to variations in initial dislocation density than initial volume fraction recrystallized by many orders of magnitude. The model deviates from expected values by one order of magnitude due to variations of 50% in nucleation site density (likewise for the scaling parameter A_5). For 50% variations in activation energies of vacancy self-diffusion and grain boundary atomic migration the model showed deviations of approximately five-fold. Variation in the numerical values of the scaling parameter for hardening and dynamic recovery, A_1 , within one order of magnitude, resulted in the magnitude of the accumulated dislocation density varying by greater than an order of magnitude. Variations as large as 100% of the values of the scaling parameter for static recovery, A_2 , changed resulting model variables by less than 5%.

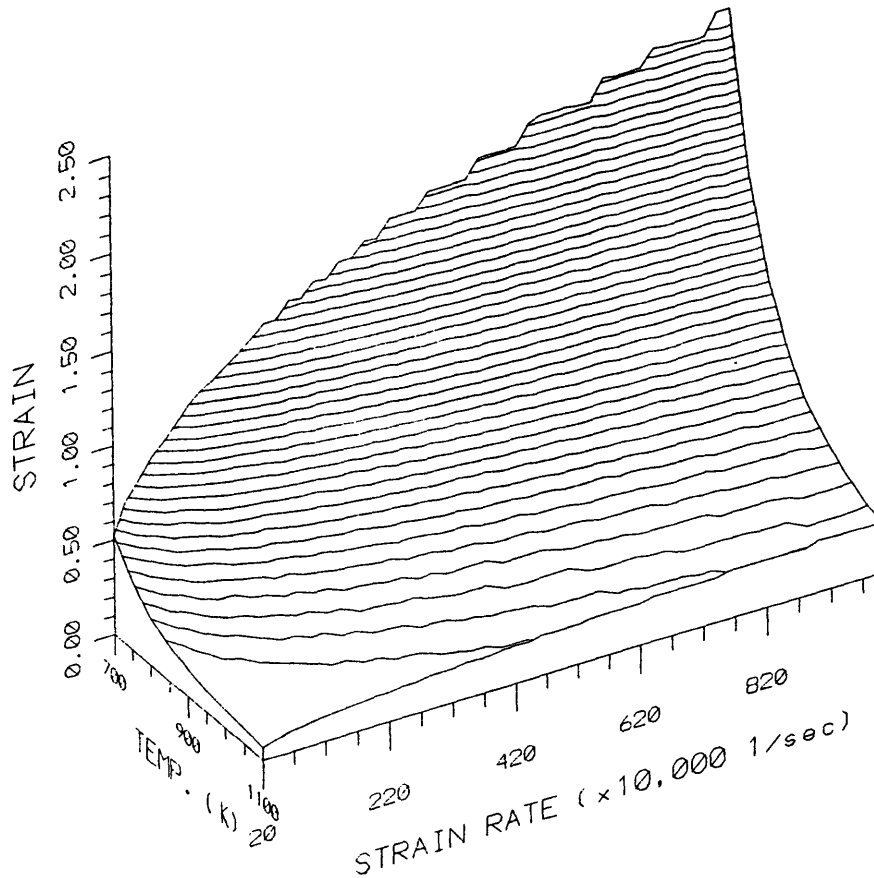


Figure 2.11 Processing envelope. Surface gives strains at peak stress, as a consequence of dynamic recrystallization, for isothermal, constant strain rate conditions.

Figure 2.12 shows a way to evaluate the sensitivity of the criterion to uncertainties in parameter values. The variation in the criterion is due solely to a -20% change in the activation energy for vacancy self diffusion, Q_{sd} . A reduction in the activation energy for vacancy self diffusion increases the static recovery rate, which leads to a reduced steady state dislocation density, ρ_{ss} , without influencing the final value of the volume fraction recrystallized, namely $v_r = 1.0$. The reduced value for ρ_{ss} makes the trajectory corresponding to the smaller value for Q_{sd} appear below trajectory corresponding to the unmodified value for Q_{sd} . Since Q_{gd} is correlated with Q_{sd} , the simulation in figure 2.12 should have included the effect of the reduction in value of Q_{gd} . The figure presents the simulation without a corresponding decrease in the value of Q_{gd} to emphasize the ability of the model-based approach taken by this work to interpret the consequences of variations in parameter values unambiguously.

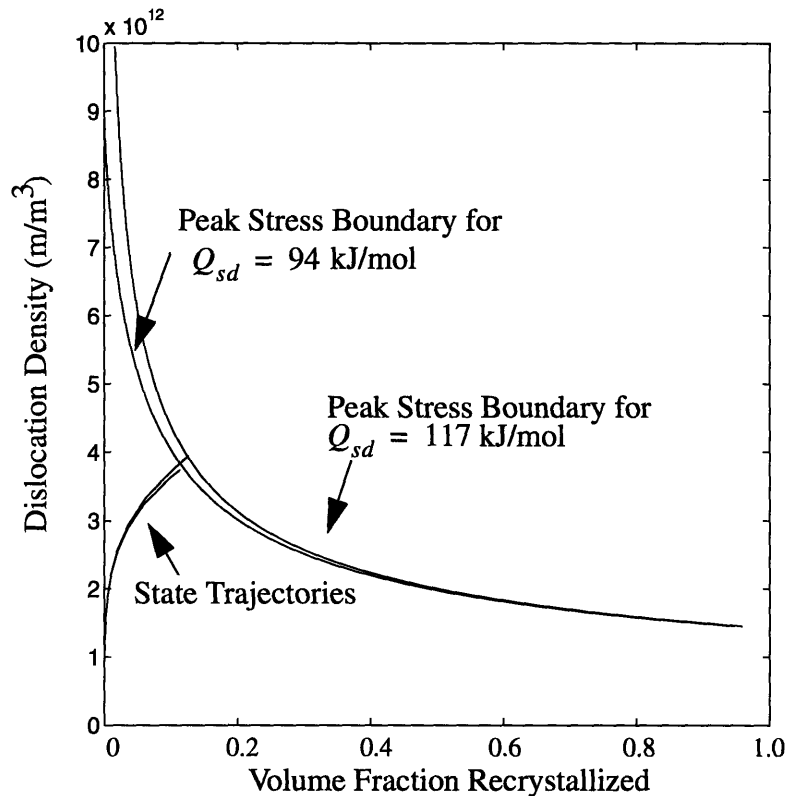


Figure 2.12 Effect of a -20% change in the activation energy for vacancy self diffusion, Q_{sd} on the criterion predicting the first peak in stress and the state trajectory (upper trajectory corresponds to the unchanged case).

The criteria represented by equation (2.30) is not limited to isothermal, constant strain rate conditions, and can accommodate arbitrary deformation and temperature histories. It was not possible to validate this general criterion with experimental data since data in the literature is not given for conditions where the temperature and strain rate vary. Calibration of microstructurally-based models of dynamic recrystallization will require data taken under more complicated, nonsteady conditions, both to test whether the model is sufficiently robust to handle these conditions and to simulate true processing conditions.

The model can increase in complexity without necessarily changing the manner in which the criterion is determined. Nucleation kinetics, for example, can be added through another state variable that represents nucleation site density. This would require another kinetic equation for the evolution of nucleation sites, but there is no fundamental restriction to two internal state variables. A recent review by Peczak and Luton [41] of

nucleation models offers a logical place to start an investigation. The lack of a nucleation model may account for the criterion's inability to reproduce the dependence on strain rate as seen exhibited in figures 2.7 and 2.7 by the increasing departure of the simulated strain at peak stress from the experimental data for increasing strain rate. By taking nucleation site density as a constant, instead of increasing with increasing dislocation density, the volume fraction recrystallized increases more slowly and hence the strain at the first peak in stress is larger than would otherwise occur. Larger than expected strains at peak stress are seen in figure 2.7.

Similarly, the characterization of the flow response of a material to an applied stress, equation (2.27), includes the effect of the recrystallizing material in a very simple manner by using a volume average of unrecrystallized material. Flow equations that use other approaches to obtain the macroscopic viscoplastic strain rate, for example by assuming multiple phases with different viscoplastic flow behavior, can be used without loss of generality.

The model of the stress response is not unique, so other scalar-valued functions that have alternative physical interpretations should be considered. Candidate functions include the energy dissipation rate and a measure of the free energy of the metal that includes the contribution of lattice strain energy, dislocation elastic self energy, and grain boundary energy. The different functions will establish different criteria, i.e., different regions of temperature, strain rate, dislocation density, and volume fraction recrystallized that denote a peak in stress.

2.7 Nomenclature

Symbol	Definition
A_1	Scaling constant for athermal hardening.
A_2	Scaling constant for static recovery.
A_3	Scaling constant for saturation dislocation density.
A_4	Scaling constant for viscoplastic strain rate.
A_5	Scaling constant for volume fraction recrystallization evolution.
b	Magnitude of Burgers vector.
C_{ac}	Accommodation coefficient.
c_p	Specific heat.
k	Boltzman's constant.
k_{th}	Thermal conductivity.
m_1	Power law dependence of static recovery on ρ .
m_2	Power law exponent.
n	Power law exponent.
N_s	Nucleation site density.
Q_{dr}	Activation energy for cross-slip.
Q_g	Activation energy for glide.
Q_{gb}	Activation energy of grain boundary atomic migration.
Q_{sd}	Activation energy for vacancy self-diffusion.
T	Absolute temperature.
T_m	Melting temperature.
v_r	Volume fraction recrystallized grains.
ω	Fraction of plastic work converted to heat, approximately 0.9.
ΔG	Change in free energy due to recrystallization.
$\dot{\epsilon}$	Viscoplastic strain rate.
μ	Shear modulus.
v_c	Attempt frequency for climb.

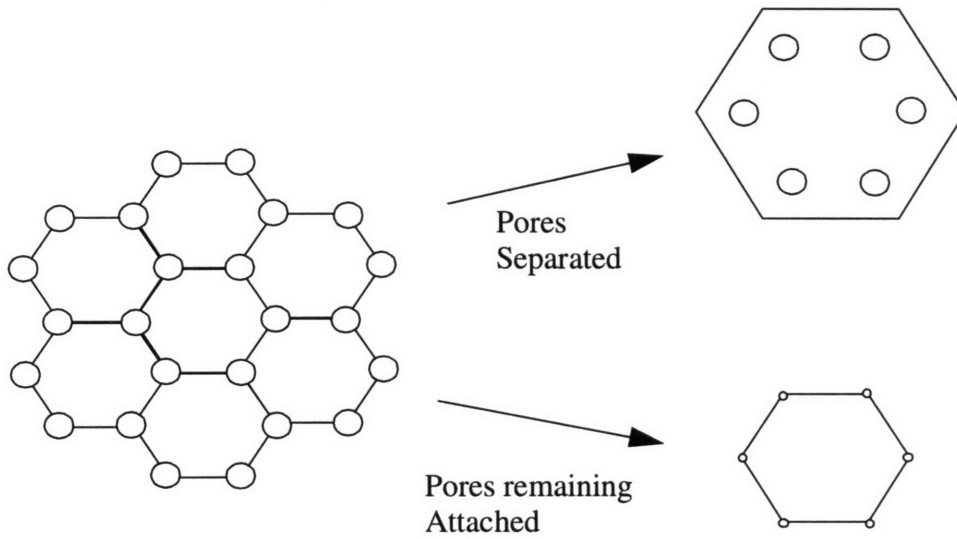
Symbol	Definition
v_{dm}	Attempt frequency for dislocation motion.
v_{gb}	Atomic grain boundary jump frequency.
ρ	Dislocation density in unrecrystallized grains.
ρ_d	Mass density.
ρ_{ss}	Steady-state dislocation density.
$\tilde{\rho}$	Scaling constant representing a maximum dislocation density.
σ	Stress response.
Ω	Atomic volume.

CHAPTER 3 A Criterion for Pore Separation

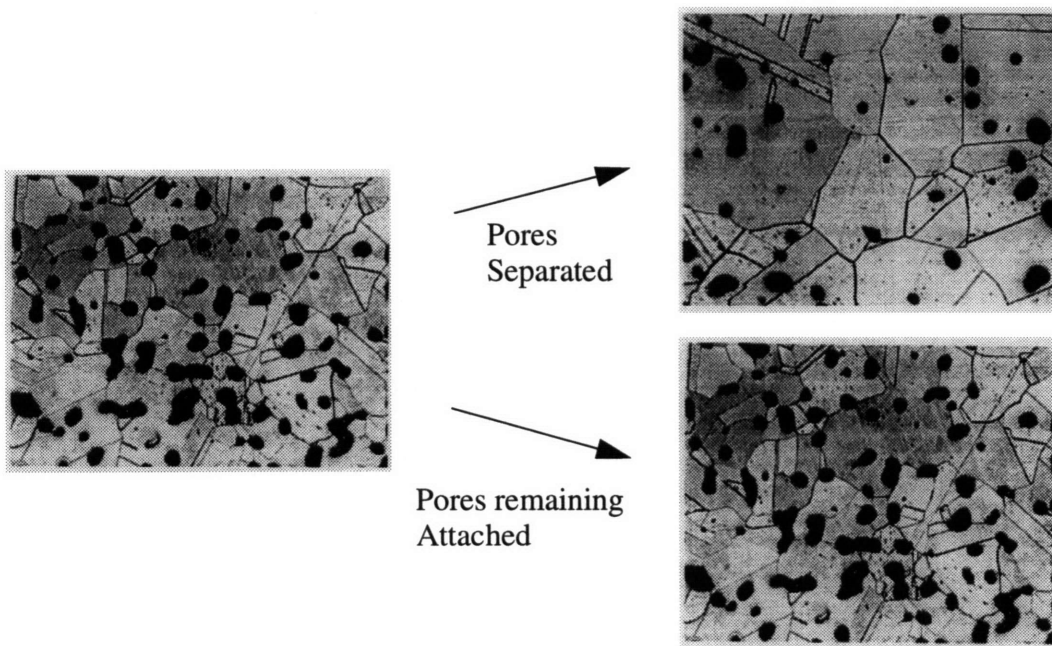
This chapter considers the phenomenon of pore separation within a state variable, nonlinear system dynamics framework. Pore separation is defined as the detachment of closed voids from a migrating grain boundary. The effect of pore separation on the evolution of a material's microstructure is characterized by a large increase in the rate of grain growth and a sharp curtailment in the rate of pore shrinkage. Figure 3.1 illustrates this characteristic evolution in microstructure. The micrographs shown in the figure are from Aigeltinger for OFHC copper sintered in air at a temperature of 1278 K [42].

A macroscopic effect of pore separation is the steep reduction in rate of consolidation of a material with closed voids. Figure 3.1 shows a simulated state trajectory before and after pore separation. The simulation uses a model described in detail in section 3.2 and parameter values for OFHC copper tabulated by Frost and Ashby in [14]. A criterion to predict pore separation would be useful because an unexpected decrease in the densification rate during a consolidation process can lead to a component with an unacceptably large residual porosity. It is assumed in this chapter that the driving force for grain boundary migrating arises solely from a distribution of grain sizes in the material.

The analysis presented here results in two criteria for pore separation. The derivation of the first criterion assumes a global model for pore separation, i.e. the simultaneous detachment of several pores from a single grain, as depicted in figure 3.3. The derivation uses the same global model used to derive an existing, popular criterion for pore separation. It is shown, for the first time, that this popular criterion fails to account for the effect of entropy transfer, which is accounted for by the first criterion proposed in this chapter. The derivation of the second criterion assumes a local model for pore separation, i.e. the detachment of a single, isolated pore from a two-grain boundary, as illustrated in figure 3.4. The second criterion is an improvement over the first criterion. The second



a) Schematic of microstructural evolution



b) Micrographs showing accelerated growth of grains for pore separation

Figure 3.1 (a) Schematic of the microstructural evolution characterizing pore separation. (b) Micrograph on the left shows closed voids residing primarily on grain boundaries. Micrograph on upper right shows pores separated from grain boundaries, from Aigeltinger [42]. Micrograph on lower right is a copy of the one on the left to roughly illustrate continued pore attachment.

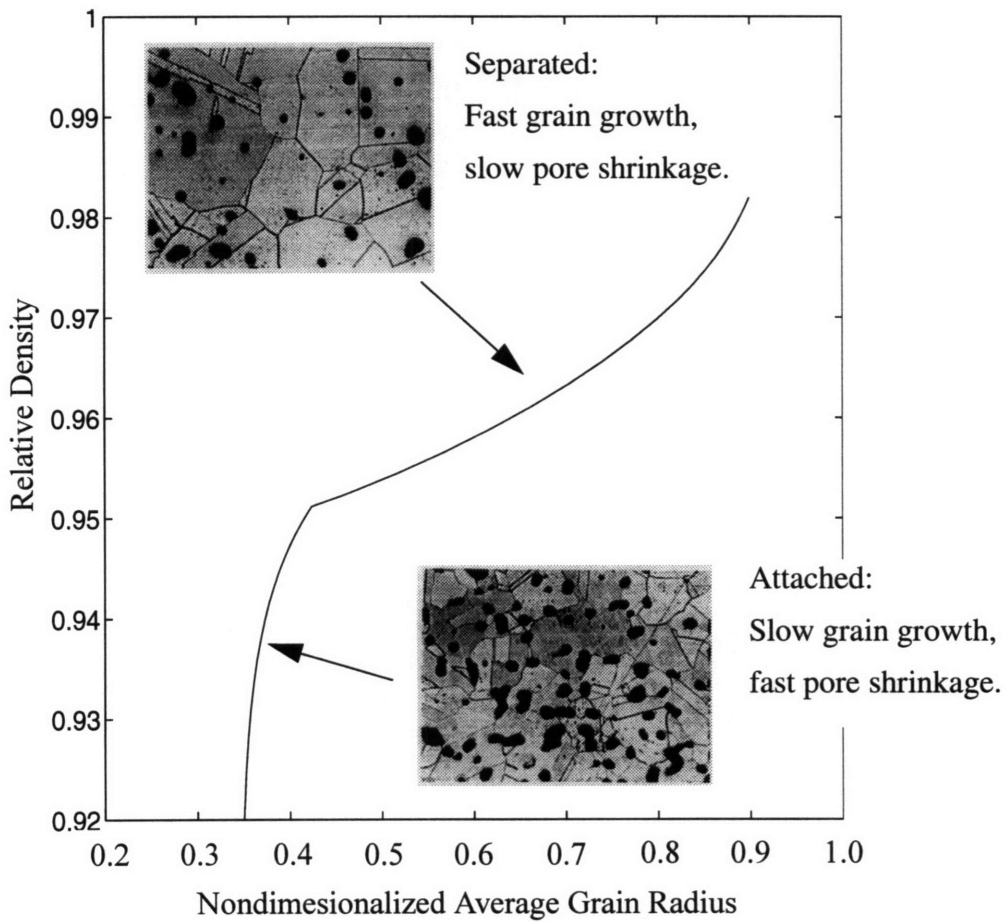


Figure 3.2 Simulated state trajectory showing the effect of pore separation for OFHC copper at $T = 1200$ K and $P = 50$ MPa. Micrographs are the same used in figure 3.1 to illustrate roughly the linkage with microstructural evolution.

criterion is an explicit function of both temperature and pressure whereas the first criterion accounts for temperature explicitly but only indirectly accounts for processing pressure. Implications of the second to planning pressure and temperature schedules for hot isostatic pressing are discussed.

The derivation of both criteria assumes a single phase, polycrystalline material with a uniform temperature field, T , and surface energy, γ . In this treatment pores are assumed closed, i.e. relative densities greater than about 0.92, and grain boundary migration is modeled as driven only by the reduction in energy associated with decreasing grain surface area.

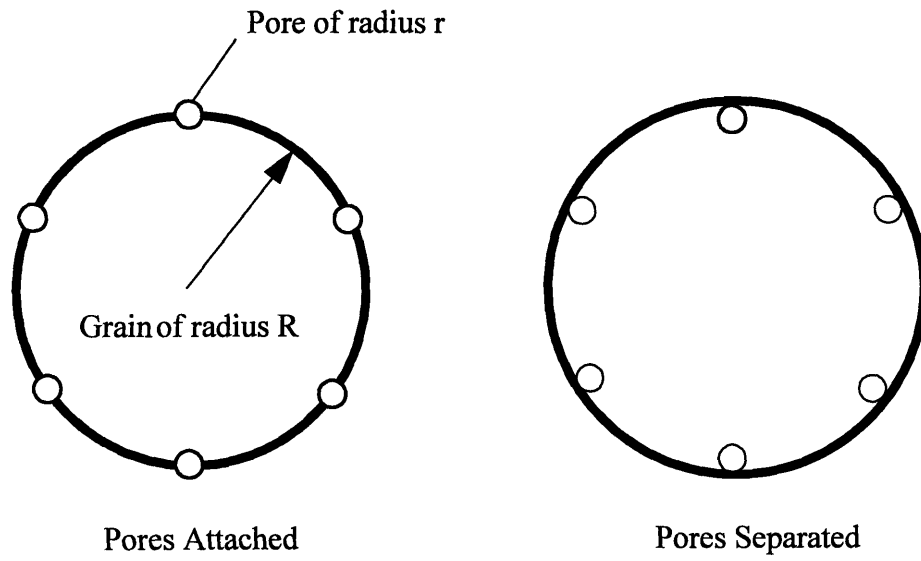


Figure 3.3 Global geometric model of a pore separation.

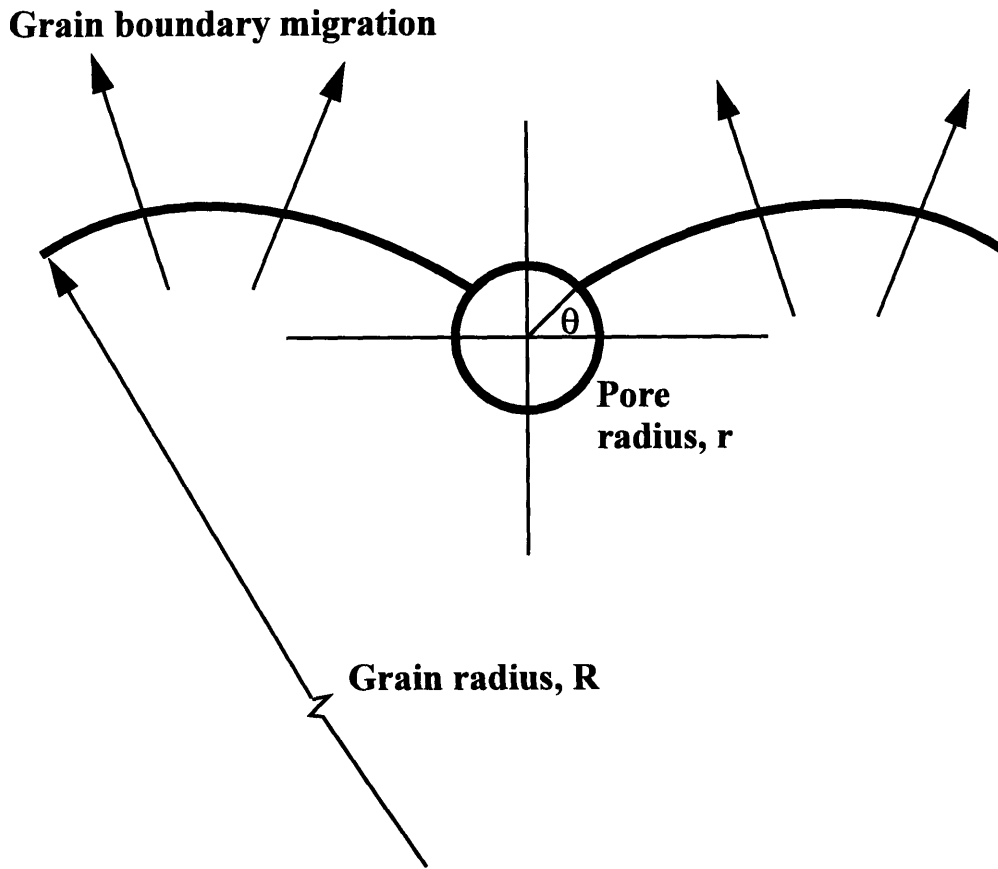


Figure 3.4 Local geometric model of pore separation.

3.1 Previous Work to Develop a Criterion for Pore Separation

Previous efforts to derive criteria for separation are classified here as global or local. Global analyses treat separation as the simultaneous detachment of many pores from a single grain. Local analyses treat separation as the detachment of an isolated, single pore from a grain boundary. The following review of previous research focuses on initial contributions to the analysis of pore separation from grain boundaries.

3.1.1 Previous Local Analyses for Pore Separation

This section begins by categorizing local analyses of pore separation into three approaches; one, a balance of forces acting on a pore attached to a grain boundary; two, equating the grain boundary migration rate with the pore velocity during drag; and three, a free energy balance of the region local to a pore attached to a grain boundary. The section concludes by reviewing models of the grain boundary geometry local to a dragged pore.

Zener [43] proposed a model of pore separation as a force imbalance acting on a single spherical pore attached to a migrating grain boundary. His approach is independent of the shape of the grain boundary and implicitly assumes a single value of surface energy throughout the system. Ignoring the shape of the grain boundary implies neglecting the contribution of curvature local to a pore to the driving forces of separation. However, estimates of the contribution of local curvature to the free energy of the region local to a pore show that this contribution is small compared to the free energies associated with the local pore-grain and grain-grain surface areas.

By comparing the velocity of a pore with the grain boundary migration rate, Nichols [44], Brook [45], and Kingery and Francois [46] developed separation criteria. Their analysis asserts that the pore velocity and grain boundary migration rate must be unequal in order for a pore to separate. Yet, forces acting on a pore and grain boundary are assumed to remain in equilibrium during separation. The resulting criterion is a function of pore size, grain size, and temperature. The grain boundary geometry local to a pore does not enter into their analysis. Also, pores are assumed to be randomly distributed throughout the material. This assumption is not valid for analyzing the first occurrence of pore separation from grain boundaries during consolidation processing because, initially, all pores reside on grain boundaries for powdered materials.

Speight and Greenwood [47] investigated pore separation by examining the change in free energy local to a pore subject to grain boundary displacements. The model predicts that the equilibrium grain boundary geometry changes as pores near separation. They use approximate values for the maximum deflection of the grain boundary and pore spacing at separation to simplify a differential expression characterizing the grain boundary. Hence, their criterion does not require an model for the grain boundary shape.

Several researchers have proposed models of the grain boundary shape local to a pore prior to separation. Gladman [48] postulated a simple grain boundary shape local to a single pore. His expression correlates well with micrographs of pores in various equilibrium configurations prior to separation, but it is not derived from first principles. Hellman and Hillert [49] derived an expression for the shape of the grain boundary local to a single pore by minimizing the surface area of the grain boundary local to the pore. The resulting shape is a catenoid of revolution. In their derivation they assumed a constant surface energy local to the pore. Hazzledine et. al. [50] derived an expression for the shape of the grain boundary local to a single pore by requiring that the grain boundary local to the pore have zero net curvature. They also assume a constant surface energy local to the pore. Worner and Cabo [51] showed that the expressions for the grain boundary shape local to a pore by Hellman and Hillert are equivalent to the shape derived by Hazzledine et. al.. They show that the radial extent of the catenoid model has an upper bound due to the assumption that growing grains must have an expanding grain boundary. They also indicate a lower bound for the catenoid radial extent linked to the assumption that the catenary is tangent to the spherical grain boundary at their point of contact [52].

Elst et. al. [53] subsequently reviewed several separation criteria and argue that the refinements by Worner and Cabo to the catenoid model by Hellman and Hillert result in a suitable description the shape of a two-grain boundary local to a pore prior to separation.

3.1.2 Previous Global Analyses for Pore Separation

Ashby [54] has proposed a pore separation criterion for hot isostatic pressing and sintering. The criterion does not predict the evolution of grain boundary configurations prior to separation. Separation is modeled as discrete, rather than gradual, detachment of multiple pores simultaneously from a single grain. His analysis is predicated on an energy

balance for a single grain. The grain's internal energy change is modeled by the change in its grain boundary area, and an energy transfer is given by the approximate work done by the grain boundary during separation. An entropy balance is not included in his development.

The global and local analyses reviewed so far idealize the shape of pores and undistorted grains as spherical. Liu and Patterson [55] arrive at a separation criterion given grain-boundary-pinning particles that are not well approximated as spheres. They achieve this result by making an order-of-magnitude approximation of the maximum deflection of the grain boundary at the onset of separation. Hence, there is no use for an expression of the grain boundary shape. The derivation of their criterion incorporates an argument similar to Brook and Nichols.

3.1.3 Selected Assumptions used in this Chapter from Previous Work

This section reviews selected analysis and experimentation by researchers investigating consolidation processing. The following results are used to restrict the extent of the internal variable model used in this chapter.

Gore et. al. [56] examined the role of thermal activation to the onset of separation. For thermally activated separation to be of primary importance the required ratio of pore radius to grain radius translates to relative densities of at least 0.999. The range of relative densities in this analysis is restricted from 0.92 (approximately the relative density of pore closure) to 0.99. Thermally-activated pore separation from a grain boundary does not therefore enter the analysis. Given the contribution of thermal activation in densification (i.e. pore shrinkage) kinetics and grain growth, temperature should still appear as a state variable in any criterion for pore separation.

The analysis of pore separation kinetics requires a model of the "forces" acting on a grain boundary. In isothermal consolidation processes the primary driving force for grain boundary migration is associated with a distribution in grain sizes. Hillert's [57] standard expression characterizing the driving "pressure" of secondary recrystallization due to a variation in grain sizes is selected. Gladman's [48] modification to the Hillert formulation shows better correlation with experimental data. The Hillert expression is retained in the

analysis given its fundamental form. Gladman's modification can be incorporated if required.

Several researchers have examined pore, grain, and grain boundary geometries, and have suggested how the geometries alter an analysis of separation. Ashby [58] showed that the grain boundary geometry local to a pore is a function of the pore-grain and grain-grain surface energies local to a pore. A variation in these two surface energies results in grain boundary geometries local to a pore that are more complex than the geometric models discussed so far. A single value for surface energy is assumed in this work as it corresponds to a wide class of materials used by consolidation processes. The consequence is that in the local model used here of a pore attached to a grain boundary, the grain boundary will intersect the pore perpendicularly. The analysis presented in this chapter is not applicable to the more complicated case of variations in surface energy. More specifically, the approach can be applied to variable surface energy conditions, but then the analysis presented here would require at least another state variable to accommodate the increased complexity of the grain boundary geometry. Spears and Evans [59] base their separation criterion on an entirely different model of the grain boundary geometry than has been so far reviewed. They modeled pore geometries at four-grain junctions, rather than two-grain boundaries. Based on evidence presented by Hseuh et. al. [60] it is assumed that pores migrate from four-grain junctions to two-grain junctions *prior* to separation from grain boundaries. Therefore, the internal variable model for pore separation assumes pores residing on two-grain junctions.

Ringer et. al. [61] reported a series of experiments examining the role of pore geometry to the onset of separation, particularly in changing the drag a pore exerts on a grain boundary. The criterion derived in this chapter is limited to those cases where a spherical pore geometry is a suitable approximation of the pore shape. Kellet and Lange [62] examined the effects of pore size distributions on densification kinetics and showed that particle distribution has an important influence on densification kinetics. The internal variable model used in this work very roughly characterizes a distribution of particle sizes with a mean particle dimension and a maximum particle size. So, the accuracy of the

predictions by the criterion derived here decreases as the particle size distribution becomes broad.

3.2 Internal Variable Model of Grain Growth and Densification Kinetics

The analysis is limited to the consolidation of single phase metals, ceramics, and compounds. The pressure and temperature are assumed given by a consolidation processing schedule and hence evolution equations for pressure and temperature are not included in the internal variable model. The consolidation process is modelled as providing a uniform temperature field within the powder compact and isostatic pressure on the compact. The states chosen to describe grain growth and the evolution of relative density are: relative density Δ , nondimensionalized mean grain radius \tilde{R} , temperature T , and pressure P (symbols are defined at the end of this chapter).

The modeling requirements are simplified by the following assumptions. The analysis focuses on a single grain of average size within a distribution of sizes. The mean grain size of the powder particles is assumed to equal the mean particle size when pores first close. All pores are assumed closed, and like grains and powder particles, they are modeled as spheres. Pores are not randomly dispersed throughout the material [54] because they are initially located at the junctions where four particles meet. The analysis only considers the first occurrence of pore separation and does not consider reattachment of pores and subsequent separations. It is further assumed that pores do not coalesce, deviate from a spherical shape, or change size as a consequence of separation.

Ashby derived a model of the grain growth and consolidation of powder compacts during hot isostatic pressing or sintering [63][64]. To illustrate the system dynamics approach of this work, a new internal variable model is not derived in this chapter. Rather, the kinetic equations proposed by Ashby in [54] are used, with four modifications. One, of the two grain growth rate equations available, one assuming pore drag and the other assuming pore separation, only the pore drag equation is used. This is because physically, grain growth begins with pores attached. Two, only those portions of the model that characterize when pores are closed and attached to grain boundaries (i.e. the start of stage 2 densification using Ashby's nomenclature, or equivalently, relative densities greater than approximately 0.92) are used. Three, at pore closure most consolidation processing

temperature and pressure schedules are in a regime where, using Ashby's nomenclature, high-temperature creep dominates the overall densification rate. Therefore, the contribution of low-temperature creep is neglected. The approach would be the same if this low-temperature creep were not neglected; this choice is done solely for convenience. Four, it is assumed that when pores have closed the average grain size is equal to the average particle size. Hence, the contribution from Nabarro–Herring/Coble creep to densification is small and is therefore neglected.

The evolution equation for grain growth with pore drag is, after Ashby [54]:

$$\frac{d\tilde{R}}{dt} = \frac{C_3 \gamma \Omega}{2\tilde{R}R_m kT} \quad (3.1)$$

$$\cdot \left[\frac{\delta D_{os} \left(\Omega^{1/3} D_{om} \right) \exp \left[- \left(\frac{Q_m + Q_s}{kT} \right) \right]}{\delta D_{os} \Omega^{2/3} \exp \left(\frac{-Q_s}{kT} \right) + C_4 \left(\Omega^{1/3} D_{om} \right) (1 - \Delta)^{4/3} \tilde{R}^2 R_m^2 \exp \left(\frac{-Q_m}{kT} \right)} \right]$$

where $C_4 = 0.175$ and

$$C_3 = (1 - \tilde{R}) . \quad (3.2)$$

Ashby models densification in a powder compact during hot isostatic pressing or sintering by superimposing the densification rates of several mechanisms. These densification mechanisms, given the modifications this model mentioned earlier, are: volume diffusion, boundary diffusion, and power-law creep [54]:

$$\frac{d\Delta_{vd}}{dt} = 3 \left(\frac{1 - \Delta}{6\Delta} \right)^{4/3} \frac{D_v}{\tilde{R}^2 R_m} \tilde{F}_2 \quad (3.3)$$

$$\frac{d\Delta_{bd}}{dt} = 4 (1 - \Delta) \frac{\delta D_b}{\tilde{R}^3 R_m^3} \tilde{F}_2 \quad (3.4)$$

$$\frac{d\Delta_{plc}}{dt} = 1.5 \Delta (1 - \Delta) D_c \left[\frac{1.5}{n} \frac{P}{S_{ref} (1 - (1 - \Delta^{1/n}))} \right]^n \quad (3.5)$$

where

$$\tilde{F}_2 = \left[\frac{P\Omega}{kT} + 2 \left(\frac{6\Delta}{1-\Delta} \right) \frac{\gamma}{\tilde{R}R_m} \right] \frac{\Omega}{kT} \quad (3.6)$$

$$D_v = D_{ov} \exp \left[-\frac{Q_v}{kT} \right] \quad (3.7)$$

$$D_c = 10^{-6} \exp \left[\frac{-Q_c}{kT} \left(\frac{T_m}{T} - 2 \right) \right] \quad (3.8)$$

$$\delta D_b = \delta D_{ob} \exp \left[-\frac{Q_b}{kT} \right]. \quad (3.9)$$

As previously mentioned, equation (3.5) reflects, using Ashby's nomenclature, only the contribution of high-temperature creep. Nabarro-Herring/Coble creep is neglected since the average grain radius is assumed to equal the average particle radius for relative densities of 0.92 and greater. Equations (3.1) through (3.9) is the internal variable model analyzed in this chapter.

3.3 Evaluation of the Performance of the Internal Variable Model

Equations (3.1) through (3.9) comprise a system of nonlinear, autonomous, coupled ODEs in a state space representation. This system has two nullclines, $\tilde{R} = 1$ and $\Delta = 1$. The system's one fixed point is $\tilde{R} = \Delta = 1$. Investigating the model by linearization about this fixed point fails since the Jacobian is undefined at the fixed point (specifically, in the region in state space, $\{ \tilde{R}, \Delta / 0 < \tilde{R} \leq 1.0, 0.92 < \Delta < 1.0 \}$, the model is only C^0).

The line $\Delta = 1$ is neglected from the analysis since it can then be shown that each ODE in the model is continuous, hence solutions are guaranteed to exist and be unique. Excluding $\Delta = 1$ from the investigation is physically justifiable since, as mentioned in section 3.1.3, research by Gore et. al. [56] indicates that for relative densities in excess of 0.999, pore separation is dominated by thermally activated processes not considered by

this model. Hence the analysis in the remainder of this chapter is limited to the region given by $\mathfrak{R} = \{\tilde{R}, \Delta / 0 < \tilde{R} \leq 1.0, 0.92 < \Delta < 0.99\}$.

The rates for grain growth and densification given by the model are positive semi-definite in \mathfrak{R} . Therefore, \tilde{R} and Δ increase monotonically, as is expected during hot isostatic pressing or sintering. No limit cycles exist within \mathfrak{R} since the vector field within \mathfrak{R} is a gradient field, as depicted by figure 3.5. The figure shows the model's vector field for alumina parameter values as tabulated in [54]. The vector field also indicates that the fixed point $\tilde{R} = \Delta = 1$ is an attracting node. The solid line is a state trajectory generated by numerically integrating the model starting with $\tilde{R}_0 = 0.3$ and $\Delta_0 = 0.92$ for a constant temperature of 2000 K and pressure of 20 MPa. Ashby has calibrated this model over the last decade [54][64] with a wide variety of materials. His model has been has

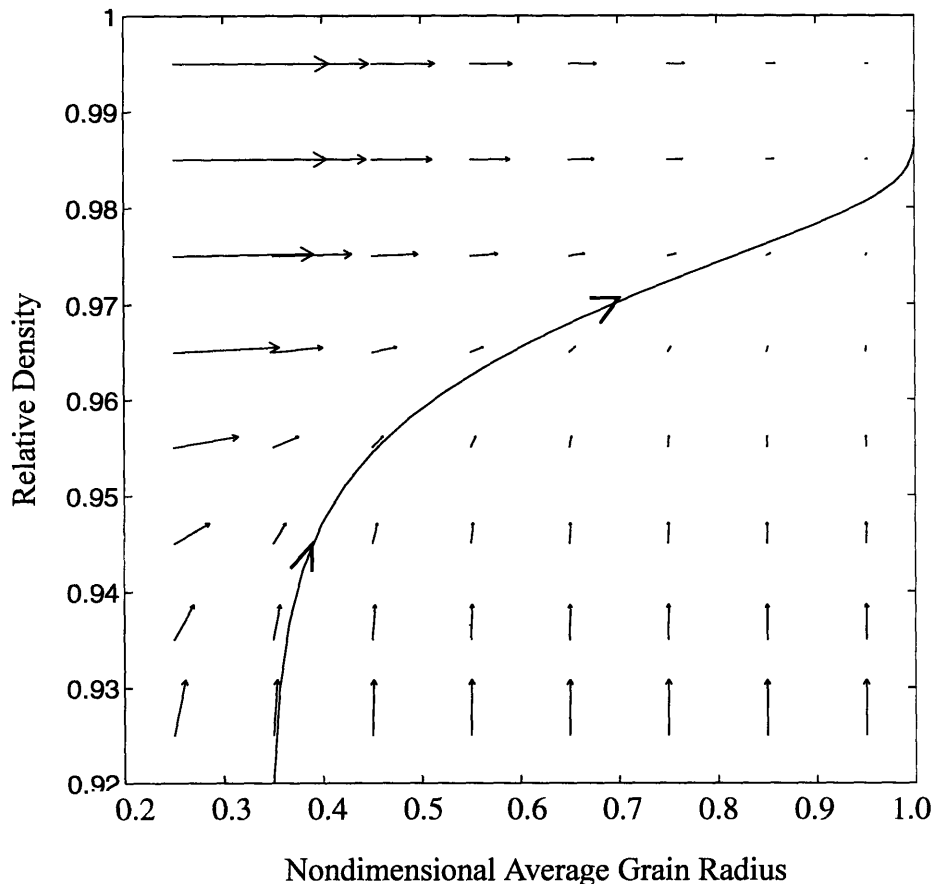


Figure 3.5 Vector field and a state trajectory using parameter values for copper tabulated in [54], $T = 1200$ K, $P = 50$ MPa, $R_{max} = 80 \mu m$, $\tilde{R}_0 = 0.35$, and $\Delta_0 = 0.92$.

seen wide use in industry as the core of a PC-based software package that simulates the stress response of a material as a function of strain rate, temperature, and pressure during hot consolidation processing. The literature showing comparison of these simulations with experimental data on the stress response is large and is too lengthy to review here. Therefore, no further comparison of the Ashby model with experimental data is warranted in this chapter.

However, as was the case with the internal variable model developed to investigate the first peak in stress due to dynamic recrystallization (chapter 2) the vector field and state trajectory in figure 3.5 has no feature which would indicate pore separation. The model was not expected to show such a feature since the grain growth rate equation is for the case of pore drag only. Therefore, the state space has none of the anticipated features, such as a boundary manifold or a limit cycle, that would correspond to the pore separation.

In the following two sections criteria will be derived that predict the onset of pore separation. In section 3.4 a criterion will be derived based on a global model of pore separation. This global criterion is derived to correct a flaw in the most popular criterion for pore separation. The global approach does not make use of the internal variable model shown in section 3.2. Section 3.5 derives a criterion for the onset of pore separation that shows how the internal variable model can be used to derive a boundary in state space that corresponds to the onset of pore separation in metals and ceramics. This second, local criterion is then shown to be superior to the global criterion in section 3.6.

3.4 A Criterion Based on a Global Analysis of Pore Separation

For a system consisting of the grain boundary of a single, idealized spherical grain with multiple spherical pores attached, figure 3.3, the fundamental relation from thermodynamics is

$$dU = TdS + \mu dn + \gamma dA \quad (3.10)$$

where U , μ , and S have their usual meanings, n is the number of atoms comprising the grain boundary, and A is the grain boundary surface area. The system is like the skin of a bubble with small bubbles on the surface. The energy balance for this system is

$$dU = \delta W + \mu' \delta n \quad (3.11)$$

where the energy transfer by work, δW , is given by the work of the migrating grain boundary driven by “force”, F , through distance dR along the radius of the grain, R

$$\delta W = FdR . \quad (3.12)$$

By mass balance, the incremental increase in the number of moles of the material making up the system is equal to the flux of material entering the system:

$$dn = \delta n , \quad (3.13)$$

and by assuming the chemical potential of atoms diffusing to the grain boundary is approximately that of atoms comprising the grain boundary:

$$\mu dn \approx \mu' \delta n . \quad (3.14)$$

Setting equations (3.10) and (3.11) equal and substituting equations (3.12) and (3.14) gives

$$FdR = TdS + \gamma dA . \quad (3.15)$$

As implied by Ashby in [54], by taking

$$\frac{TdS}{\gamma dA} \ll 1 \quad \text{and} \quad \frac{TdS}{FdR} \ll 1 \quad (3.16)$$

equation (3.15) becomes

$$FdR = \gamma dA . \quad (3.17)$$

The criterion for pore separation presented by Ashby [53] follows directly from equation (3.17). F is characterized by the Hillert expression for the driving “force” of secondary grain growth in a polycrystalline material [57]

$$F = 2\gamma \frac{(R_m - R)}{R_m R} \cdot 4\pi R^2 \quad (3.18)$$

where R_m is the largest commonly occurring grain radius. Ashby's pore separation criterion is repeated here for later comparison to separation criteria developed in this work

$$\Delta = 1 - \frac{2}{9} (1 - \tilde{R})^3 . \quad (3.19)$$

One other expression from previous work will be introduced here that will be used repeatedly later. After Swinkels and Ashby [63], average pore radius, r , is related to average grain radius, R , and relative density, Δ , by

$$r = \left(\frac{1 - \Delta}{6} \right)^{1/3} R . \quad (3.20)$$

Care must be taken when using equation (3.20) when mapping r and \tilde{R} to Δ since it is not diffeomorphic, i.e. the first partial derivative of r with respect to Δ is undefined when $\Delta = 1.0$.

I claim that the inequalities in equation (3.16) do not hold in general and therefore equation (3.15), rather than equation (3.17), is a more appropriate basis to derive a criterion of pore separation for the global geometric model depicted in figure 3.3. To prove this claim, the magnitude of the ratios in equation (3.16) will be computed for conditions typical for hot isostatic pressing and shown *not* to satisfy the inequalities. The first quantity computed in equation (3.16) is dA . Taking separation as depicted in figure 3.3, dA is very well approximated by

$$\Delta A = A|_{\text{afterseparation}} - A|_{\text{beforeseparation}} = N\pi r^2 \quad (3.21)$$

where N is the number of pores attached to a grain; nominally 24 as supported by Ashby [54]. A precise expression for ΔA would include the added grain boundary area due to the increase in the grain radius by r . This added grain boundary area is small and can be safely neglected. This enlargement in grain boundary area is small compared to the initial grain boundary area, however the total cross sectional area of the pores is a significant fraction of the initial grain boundary. Equation (3.22) compares the enlargement in grain

boundary area and the total cross sectional area of the pores to the initial grain boundary area:

$$\frac{4\pi R^2}{4\pi (R+r)^2} = \frac{1}{1+(r/R)^2} \geq 0.96 \quad (3.22)$$

$$\frac{N\pi r^2}{4\pi R^2} = \frac{N}{4} \left(\frac{r}{R}\right)^2 \leq 0.24$$

Equation (3.22) was evaluated numerically by solving equation (3.20) for $\frac{r}{R}$ and computing this ratio for closed porosity, i.e. $\Delta \geq 0.92$, which yields $\frac{r}{R} \leq 0.24$.

Continuing with the evaluation of the terms in equation (3.16), the term dS was assigned a value by first starting with an expression of the entropy balance for the system

$$dS = s\delta n + \delta S_{irr} \quad (3.23)$$

Neglecting the entropy generated by irreversibility, δS_{irr} , and using equation (3.13) yields

$$dS \geq sdn \quad (3.24)$$

Taking separation as depicted in figure 3.3, equation (3.24) becomes

$$\Delta S \geq s \left[n|_{\text{afterseparation}} - n|_{\text{beforeseparation}} \right] \quad (3.25)$$

where n can be approximated as follows. The number of atoms that occupy a grain's surface depends on the packing density of the atoms, f . Equating the fraction of the surface area occupied by atoms to the cross sectional area of an atom, of radius a , gives the number of atoms on the surface, n'

$$f(\text{surface area}) = n'\pi a^2 \Rightarrow n' = \frac{f(\text{surface area})}{\pi a^2} \quad (3.26)$$

Characterizing the grain boundary as three atoms thick, the total number of atoms, n , is

$$n = 3 \cdot \frac{f(\text{surface area})}{\pi a^2} \quad (3.27)$$

To evaluate equation (3.27), the term “surface area” was assigned the value for ΔA from equation (3.21), resulting in

$$\Delta S \geq \frac{3Nfsr^2}{a^2} . \quad (3.28)$$

The first inequality in equation (3.16) was now be evaluated by substituting equations (3.21) and (3.28)

$$\frac{T\Delta S}{\gamma\Delta A} \geq \frac{3fTs}{\pi\gamma a^2} . \quad (3.29)$$

The second inequality in equation (3.16) is simpler to evaluate than the first. The remaining quantity to compute is the change in radius, dR . Taking separation as depicted in figure 3.3, dR becomes:

$$\Delta R = R|_{\text{afterseparation}} - R|_{\text{beforeseparation}} = R + r - R = r . \quad (3.30)$$

Substituting equations (3.18), (3.20), (3.28), and (3.30) into the second inequality in equation (3.16) gives

$$\frac{T\Delta S}{F\Delta R} \geq \frac{0.206NfTs(1-\Delta)}{\pi\gamma(1-\tilde{R})a^2} . \quad (3.31)$$

where a nondimensional grain radius is defined $\tilde{R} = R/R_m$.

Table 3.1 shows the magnitude of equations (3.29) and (3.31) computed for parameter values of γ iron shown in table 3.2. The low and high magnitudes listed in table 3.1 are a function of changes in the value of f . Originally, f was taken as varying from a high of 0.91 for close-packed atoms to a low of 0.64 for randomly packed atoms. Then f was taken as varying from 1.0 to 0.1 to emphasize that the inequalities in equation (3.16) are not satisfied even for a wide variation in the density of atoms characterizing a grain boundary..

Ratio	High value ($f = 1.0$)	Low value ($f = 0.1$)
$\frac{T\Delta S}{\gamma\Delta A}$	8.0	0.8
$\frac{T\Delta S}{F\Delta R}$	0.21	0.021

Table 3.1 Magnitude of the ratios given by equations (3.20), top row, and (3.22), bottom row, for $\tilde{R} = 0.2$, $\Delta = 0.92$, and $T = 1500$ K.

Parameter	Value	Units
a	1.26	Angstrom
s	84.0	J/molK
γ	2.0	J/m ²

Table 3.2 Parameter values for γ iron used in equations (3.20) and (3.22) from [65][71].

A criterion for pore separation can now be derived based on equation (3.15). Substituting equations (3.18), (3.20), (3.21), (3.28), and (3.30) into equation (3.15) gives

$$\Delta \geq 1 - \frac{2}{9} \left[\frac{\pi\gamma(1 - \tilde{R})}{\frac{3fTs}{a^2} + \pi\gamma} \right]^3 \quad (3.32)$$

The affect of retaining the entropic term, TdS , can be seen by comparing equation (3.32) with Ashby's criterion, equation (3.19). Figure 3.6 plots both Ashby's criterion, equation (3.19), and equation (3.32), using parameter values for alumina [54] with $T = 2123$ K.

3.5 A Criterion Based on a Local Analysis of Pore Separation

In this section pore separation is analyzed for a single pore attached to a two-grain

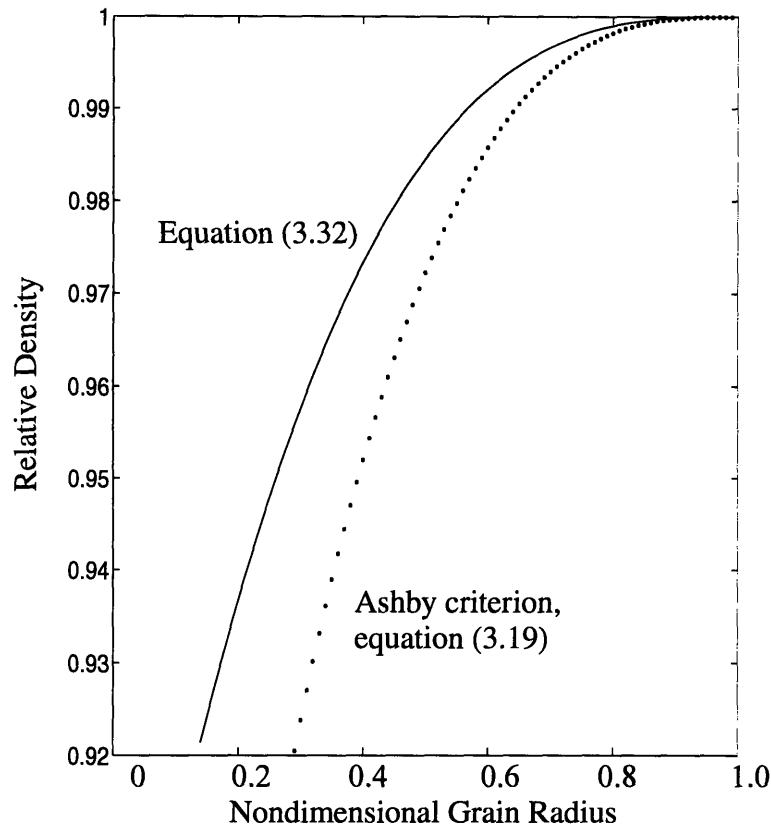


Figure 3.6 Plot of Ashby's criterion, equation (3.19), and the criterion derived in this section, equation (3.32), using parameter values for alumina [54] with $T = 2123K$.

boundary, as illustrated in figure 3.4. The system considered in this section consists of a single spherical pore and the grain boundary local to that pore.

Prior to separation the shape of the grain boundary local to the pore becomes distorted from a spherical shape, as sketched in figure 3.4, where the angle θ increases as the grain boundary distorts. The free-energy of the system evolves as the pore-grain boundary geometry changes from configurations associated with drag to a configuration representing the onset of pore separation. Stable pore-grain boundary configurations correspond to free-energy minima as shown in figure 3.7(a). As the pore progresses toward the onset of separation, the free-energy of the system increases until, at the onset of separation, the free-energy of the system attains a maximum, sketched in figure 3.7(b). The system can then lower its free-energy by progressing to pore separation. Figure 3.7(b)

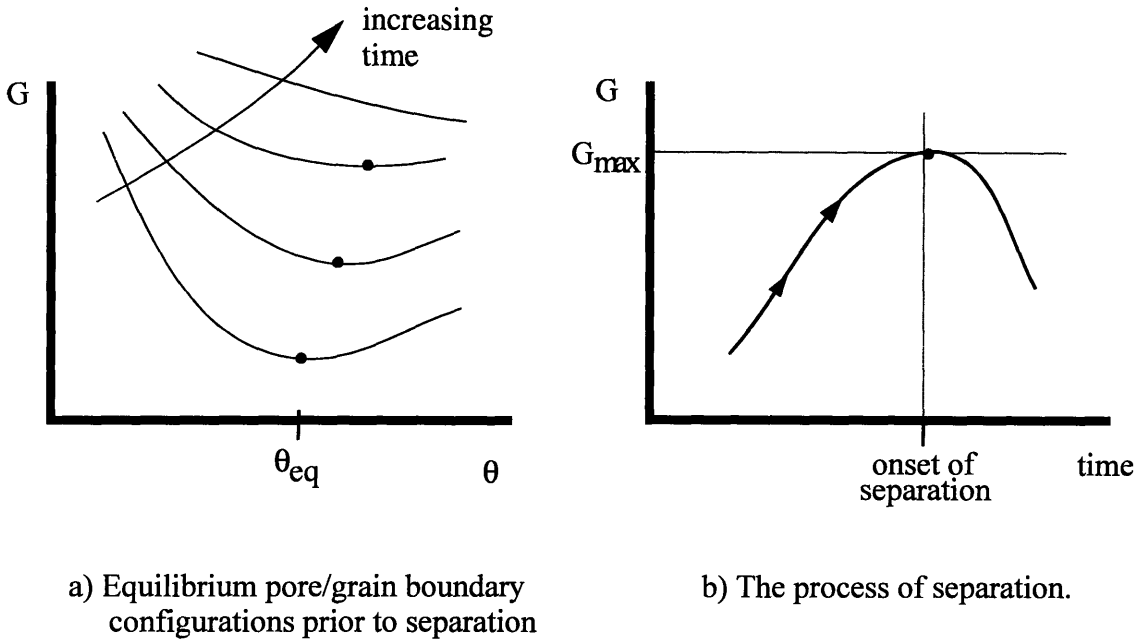


Figure 3.7 Evolution of the free-energy of the system depicted by the local geometric model of a pore separation, figure 3.4, where θ characterizes the pore/grain boundary configuration.

indicates the point where the free-energy is a maximum is a criterion for the onset of separation. In the following analysis, an expression for the free-energy of this system is derived and used to formulate a criterion for the onset of pore separation.

To begin the analysis, an expression for the free energy of the system is proposed:

$$dG = dU - TdS + \gamma dA = udn - Tsdn + \gamma dA \quad (3.33)$$

where A is now the grain boundary area local to the pore and n , by the same argument leading to equation (3.27), is $n = 3fA/\pi a^2$. The curvature associated with the distorted grain boundary is assumed large enough so that the variation in surface energy with curvature can be neglected. Taking the time derivative of equation (3.37) gives

$$\frac{dG}{dt} = u \frac{dn}{dt} - Ts \frac{dn}{dt} + \gamma \frac{dA}{dt} = \frac{uf}{\pi a^2} \frac{dA}{dt} - \frac{3fTs}{\pi a^2} \frac{dA}{dt} + \gamma \frac{dA}{dt} = \left[\frac{3f}{\pi a^2} (u - Ts) + \gamma \right] \frac{dA}{dt} \quad (3.34)$$

The onset of separation is given by setting equation [3.34] equal to zero, because, as was proposed, the onset of separation corresponds to the maximum in free energy, i.e. where $\dot{G} = 0$:

$$\left[\frac{3f}{\pi a^2} (u - Ts) + \gamma \right] \frac{dA}{dt} = 0 \quad (3.35)$$

The bracketed term in this equation represents thermodynamic driving force for pore separation, given the assumptions of the local model, section 3.1.3. It is the magnitude of the stored free energy of the system. It is comprised of a balance between internal energy and surface energy with entropy. The term $\frac{dA}{dt}$ represents the rate of change of the size of the system that is subject to the thermodynamic driving force. Since the size of the system is related to some of the length scales of the diffusion processes associated with pore separation, the term $\frac{dA}{dt}$ summarizes the effect of the underlying kinetic processes that evolve for a given material. $\frac{dA}{dt}$ represents evolution in the pathways to release the stored internal free energy. Together, the two terms measure the rate of change of free energy of the system.

For equation (3.35) to be satisfied, either the term in brackets is zero, $\frac{dA}{dt}$ is zero, or both. The term in brackets in equation (3.34) is equal to zero when $Ts - u = \frac{\pi a^2 \gamma}{3f}$. The numerical values of these two terms are plotted in figure 3.7 for $T = 300 \text{ K}$ to $T = 2200 \text{ K}$. The figure uses values of s and u for iron from [65] and an average value of the packing density, f , computed as follows. f ranges from a value of 0.64 for random packing to a value of 0.91 for close packing. The figure assumes an average of these values, 0.78. The point of intersection of the two curves in the figure is the temperature at which the bracketed term in equation (3.35) is equal to zero. This temperature is well below the temperature at which consolidation processing normally takes place for iron. Nevertheless, the criterion predicts that there is no thermodynamic driving force available for pore separation at this temperature, despite the availability of kinetic processes for pore separation. Further investigation of cases where the bracketed term is equal to zero, for materials other than iron, was not pursued. When $\frac{dA}{dt}$ is zero, there is both the thermodynamic driving force and kinetic processes available for pore separation.

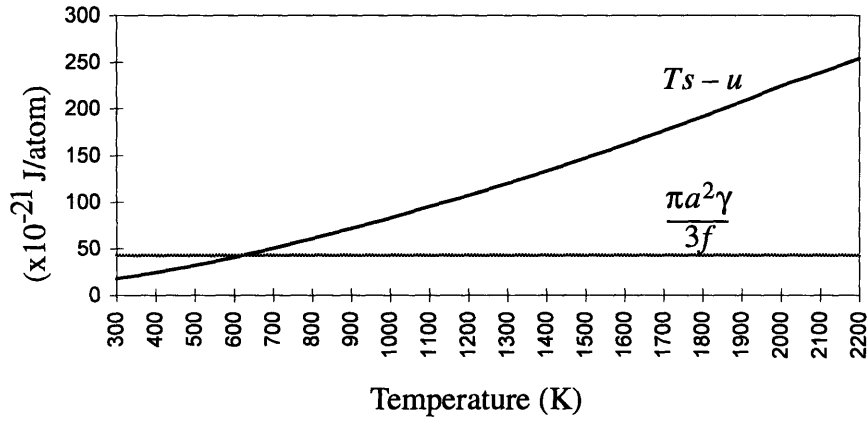


Figure 3.8 Plot of the numerical values of $Ts - u$ and $\frac{\pi a^2 \gamma}{3f}$ as a function of temperature using values of s and u for iron from [65], and $f = 0.78$. γ is taken constant with temperature. The intersection of the two curves is the point where the bracketed term in equation (3.35) is equal to zero.

Therefore, by neglecting the bracketed term, the criterion for the onset of pore separation, equation (3.35), simplifies to:

$$\frac{dA}{dt} = 0. \quad (3.36)$$

An expression for the shape of the grain boundary local to the pore, A , is needed to compute $\frac{dA}{dt}$. Hellman and Hillert [49] derived an expression for the shape of the grain boundary local to a single pore by minimizing the surface area of the grain boundary local to the pore. The result is a catenoid of revolution. Worner et. al. [52] show that the radial extent of the catenoid model has an upper bound due to the assumption that growing grains must have an expanding grain boundary. They also indicate a lower bound for the catenoid's radial extent by taking the catenoid tangent to the spherical grain boundary at their point of contact. For a catenoid of revolution, A is given by [49]

$$A_{\text{cat}} = \pi c^2 \left\{ \left[\frac{R}{c} \left(\frac{R}{c} - 1 \right) \right]^{1/2} - \frac{\cos \theta}{\sin \theta} + \text{acosh} \left(\frac{R}{c} \right)^{1/2} - \text{acosh} (\csc \theta) \right\} \quad (3.37)$$

$$c = \frac{1}{2} r \sin 2\theta$$

Therefore, evaluating equation (3.36) involves taking the time derivative of equation (3.37). This derivative is potentially a very complex expression. Instead of evaluating this derivative, I propose modelling the area of the distorted grain boundary local to a pore as a simpler geometry; a right circular cone. The radius and height of the cone are taken equal to the radial extent of the catenoid of revolution, $a_{\text{cat}} = \sqrt{0.5rR \sin 2\theta}$, as shown by Worner et. al. [52], with two modifications. One, evaluate $\sin 2\theta$ at $\theta = 45^\circ$ so that the radius of the cone is $a_{\text{cone}} = \sqrt{0.5rR}$. Two, take the height of the cone such that it is equal to the height of the catenoid at $\theta = 45^\circ$ and $r/R = 0.05$, i. e. $h_{\text{cone}} = \sqrt{0.174rR}$. With these modifications the lateral surface area of the cone becomes

$$A_{\text{cone}} = 0.432\pi rR . \quad (3.38)$$

Figure 3.9 compares the surface area of the cone and the catenoid for $\theta = 45^\circ$ and $r/R = 0.05$. The figure shows that the cone's surface area deviates the most from the

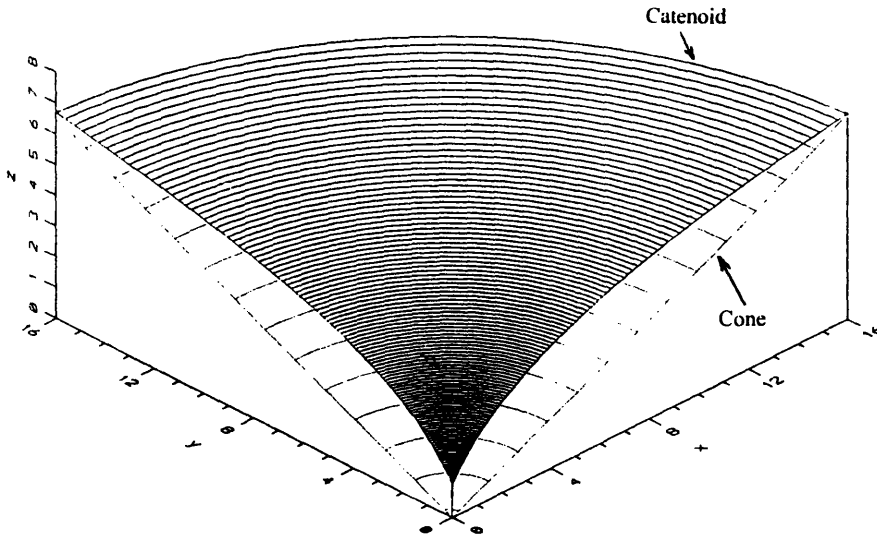


Figure 3.9 Comparison of the surface area of the cone and the catenoid of revolution for $r = 5 \mu\text{m}$, $R = 100 \mu\text{m}$, and $\theta = 45^\circ$. Only a quarter-section is shown.

catenoid's surface area near to the center where the pore is located. The cone is a better approximation to the catenoid's surface area away from the pore. The constant in equation (3.38) does not affect the criteria for separation.

Like the surface area of the catenoid of revolution, equation (3.37), the lateral surface area of the cone can have a maximum as r and R evolve since it is assumed here that r shrinks monotonically, $\dot{r} < 0$, and R grows monotonically, $\dot{R} > 0$, and in addition, $\ddot{r} > 0$ and $\ddot{R} < 0$. A maximum in the surface area implies a maximum in free-energy, which in turn denotes the onset of separation. Using A_{cone} , equation (3.38), to evaluate the criterion, equation (3.36), yields:

$$r\dot{R} + R\dot{r} = 0 . \quad (3.39)$$

Equation (3.39) can be put in terms of relative density, Δ , average grain size R , and their time-derivatives, by differentiating equation (3.20) with respect to time and substituting the result into equation (3.39), giving:

$$\frac{\dot{\Delta}}{1 - \Delta} = \frac{\dot{R}}{0.166R} . \quad (3.40)$$

This criterion for the onset of separation can be cast in terms of Δ , R , T , and processing pressure, P , by substituting for $\dot{\Delta}$ and \dot{R} in equation (3.40) with the kinetics equations for Δ and R presented in section 3.2. The result is:

$$C_6 R^6 + C_4 R^4 + C_3 R^3 + C_2 R^2 + C_1 R + C_0 = 0 \quad (3.41)$$

where

$$C_6 = 0.318k (\Omega^{1/3} D_{om}) 1.5^{(n+1)} D_c \Delta^{4/3} (1 - \Delta)^{10/3} P^n T e^{\frac{Q_s}{kT}}$$

$$C_4 = 0.603k^2 \delta D_{os} \Omega^{2/3} 1.5^{(n+1)} D_c \Delta^{4/3} (1 - \Delta)^2 P^n T^2 e^{\frac{Q_m}{kT}} + \\ 0.525 (nS_{ref})^n \Omega (\Omega^{1/3} D_{om}) D_v (1 - \Delta)^{8/3} (1 - (1 - \Delta)) P e^{\frac{Q_s}{kT}}$$

$$C_3 = 1.91 (\Omega^{1/3} D_{om}) \Omega (nS_{ref})^n (1 - \Delta)^2 (1 - (1 - \Delta))^{4/3} [0.667\delta D_{ob} P + \gamma D_v] + \\ 1.817\gamma \delta D_{os} k (nS_{ref})^n \Omega (\Omega^{1/3} D_{om}) (1 - \Delta) (1 - (1 - \Delta)) \frac{1}{R_m}$$

$$\begin{aligned}
 C_2 &= k\delta D_{os}\Omega^{5/3}(nS_{ref})^n D_v(1-\Delta)^{4/3}(1-(1-\Delta))Pe^{\frac{Q_m}{kT}} + \\
 &\quad 4.62\Omega(\Omega^{1/3}D_{om})\delta D_{ob}\gamma(nS_{ref})^n\Delta^{2/3}(1-\Delta)^2(1-(1-\Delta))e^{\frac{Q_s}{kT}} - \\
 &\quad 1.817\gamma\delta D_{os}k(nS_{ref})^n\Omega(\Omega^{1/3}D_{om})(1-\Delta)(1-(1-\Delta)) \\
 C_1 &= 3.62k\delta D_{os}\Omega^{5/3}(nS_{ref})^n D_v(1-\Delta)^{4/3}(1-(1-\Delta))^{4/3}Pe^{\frac{Q_m}{kT}}[0.667\delta D_{ob}P + \gamma D_v] \\
 C_0 &= 4.826k\delta D_{ob}\gamma\delta D_{os}(nS_{ref})^n\Omega^{5/3}\Delta^{2/3}(1-\Delta)^{2/3}(1-(1-\Delta))Te^{\frac{Q_s}{kT}}.
 \end{aligned}$$

Numerically solving for the roots of equation (3.41), over a wide range of material parameter values and values for T and P, yields one complex conjugate pair, two negative reals, and two positive reals. This result can be shown analytically. Descartes theorem states that the number of positive real roots of a polynomial with real coefficients is either equal the number of changes in sign in the series of coefficients of the polynomial, or an even number less [72]. Equation (3.41) has two changes in sign, as can be seen by inspecting the signs of each of the coefficients, assuming parameter values within physically meaningful limits. Equation (3.41) therefore has two positive real roots. Since the number of negative real roots of a polynomial $f(x)$ is equal to the number of positive real roots of the polynomial $f(-x)$, it can be readily shown that equation (3.41) has two negative real roots. The remaining roots of equation (3.41) must have an imaginary component.

The roots of equation (3.41) represent the average grain radius for a value of relative density, at the onset of pore separation. The complex roots and negative roots have no physical meaning. One of the positive real roots is four orders of magnitude smaller than the other. The smaller positive real root gives an unrealistically small ratio of average grain radius to maximum grain radius. Such a small ratio implies an enormously large driving force for grain boundary migration that would immediately lead to separation, even for a relative density of 0.92. Experiments do not support this conclusion. The larger positive real root is of the magnitude expected for the onset of separation. This larger root will be used to plot the separation criterion in the next section. Since, as shown by Ruffini and Abel [72] for the general case, polynomials of degree greater than four are

not solvable by radicals, the next section will rely on numerical simulations to solve for the roots of the criterion.

Before leaving this section an expression derived from equation (3.41) is given that relates the separation boundary to material parameters and processing inputs that is much simpler to solve than equation (3.41), but is less accurate. By Maclaurin's method, the value of the positive roots of a polynomial like equation (3.41) can be bounded within an interval (3.41). The lower value and upper value of the interval are both functions of the coefficients of the polynomial. The method states that the smaller value of the interval is given by:

$$R_{\text{lower value}} = \left[1 + \left[\frac{B}{a_0} \right]^{1/l} \right]^{-1} \quad (3.42)$$

where B is the greatest of the absolute values of the negative coefficients of the polynomial, a_0 is the leading coefficient, and l is equal to the subscript of the coefficient in the polynomial given by B . In terms of the coefficients in equation (3.41), equation (3.42) becomes:

$$R_{\text{lower value}} = \left[1 + \sqrt{\frac{|C_2|}{C_0}} \right]^{-1} \quad (3.43)$$

or

$$R_{\text{lower value}} = \left[1 + \frac{1.817 (1 - \Delta)^{1/3} [\Omega^{1/3} D_{om}]}{\sqrt{4.826 \delta D_{ob} (\Omega \Delta)^{2/3} T \exp \left[\frac{Q_s}{kt} \right]}} \right]^{-1} \quad (3.44)$$

where the first two terms in the coefficient C_2 have been neglected before substitution into equation (3.43). Since, operationally, the term under the radical is much larger than 1, equation (3.44) can be simplified to give an estimate of the dependence of the boundary on material parameters and processing inputs:

$$R_{\text{lower value}} \sim \sqrt{\frac{2.5\delta D_{ob} (\Omega\Delta)^{2/3} T \exp\left[\frac{Q_s}{kt}\right]}{(1-\Delta)^{1/3} [\Omega^{1/3} D_{om}]}}. \quad (3.45)$$

3.6 Evaluation of the Performance of the Criteria

The performance of the criterion based on the global model of pore separation, equation (3.32), is not evaluated because, like Ashby's criterion, the criterion given by equation (3.32) has many drawbacks as compared to the local approach. In contrast to the global criteria, the local criterion is not only a function of Δ , and \tilde{R} , but also includes several material parameters and all processing inputs, i.e. T and P . The local criterion is mathematically more complex than the global criterion, but both criteria are simple algebraic formulae which are easily implemented on a computer and have fast computation times. In this section the criterion based on the local model of pore separation, equation 3.40, is compared to experimental data. The performance of this criterion is quantified using a form of nonparametric test from statistics. The performance of Ashby's criterion is also evaluated since it serves as a convenient benchmark to highlight the benefits of equation (3.40).

Figure 3.9 shows sintering data from Patterson [67] and Long [68] for alumina. In this and all subsequent figures a hollow circle means that the data corresponds to micrographs showing pores predominantly attached to grain boundaries while a solid circle denotes pores were predominantly separated. The local criterion is plotted as a solid curve and Ashby's criterion the dotted. The local criterion predicts separation to the left of the solid curve. The Ashby criterion predicts pore separation to the left of the dotted line. Figure 3.9(a) indicates that both the local criterion and the Ashby criterion predict separation equally well as compared to the experimental data for $T = 1873K$. Figure 3.9(b) shows sintering data for alumina at $T = 2123K$. Figure 3.9(b) indicates that the local criterion may be better in predicting pore separation as compared to the Ashby criterion, however given the scarcity of data no conclusions can be drawn. Figure 3.9(a) plots sintering data from Watwe using nickel [69] at $T = 1523K$. Figure 3.9(b) gives sintering data from Aigeltinger [42] using copper at $T = 1278K$. Taken together, these plots suggest that the

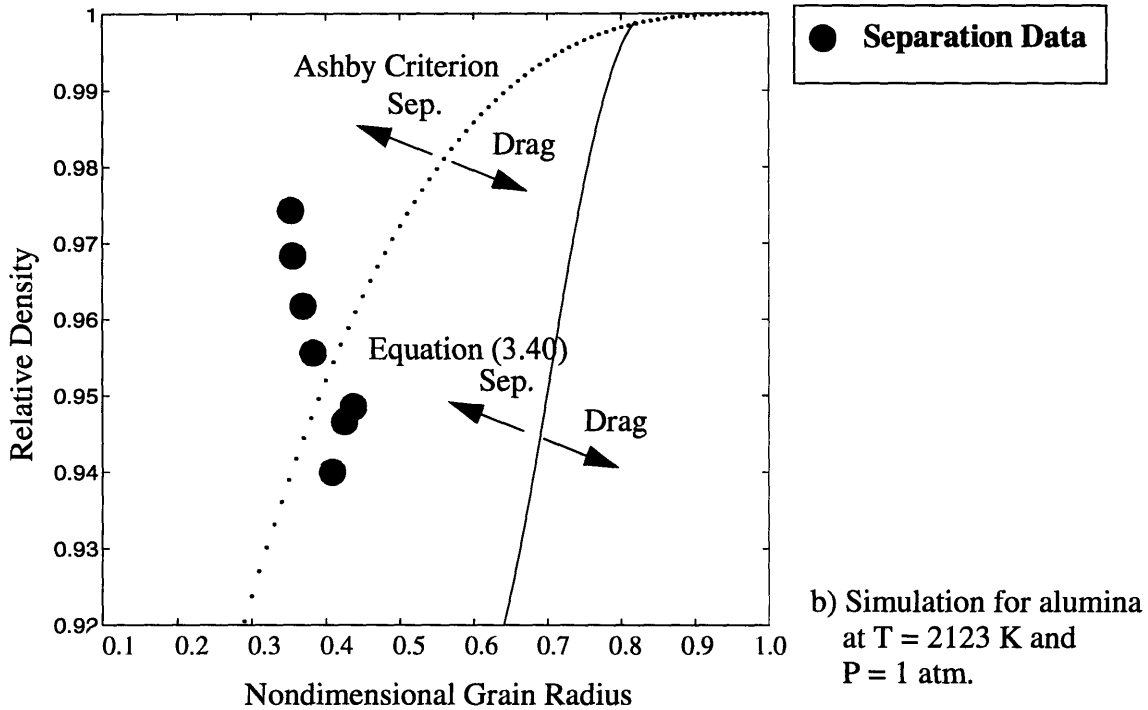
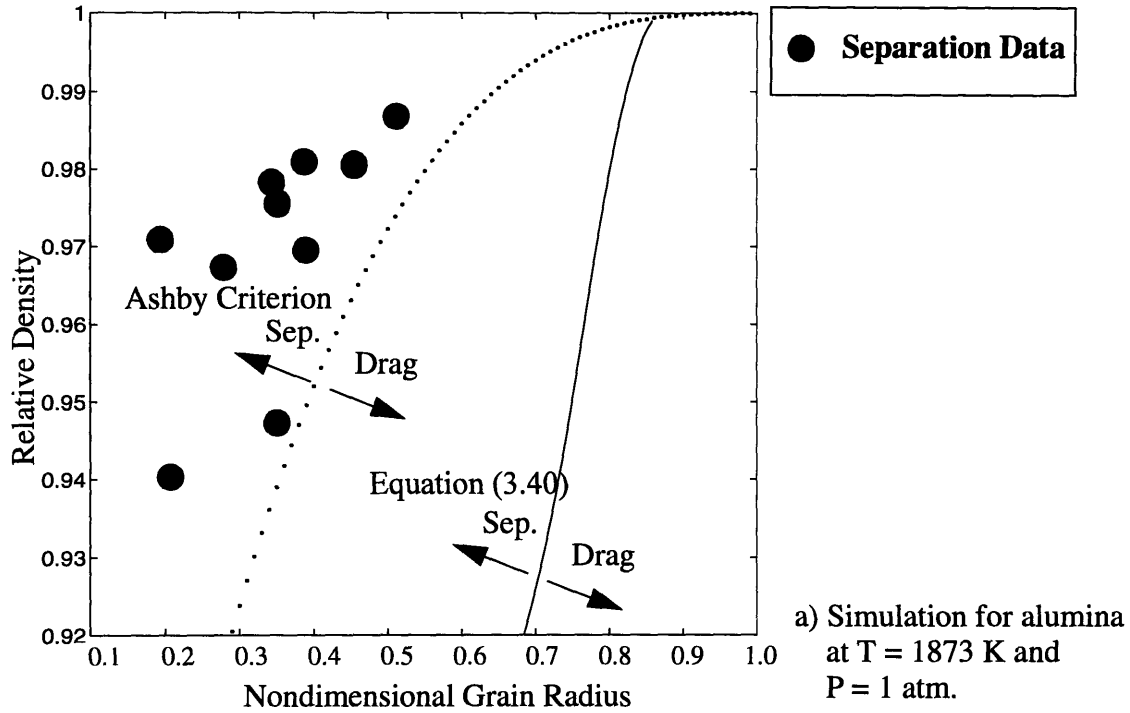


Figure 3.10 Separation criterion developed in this work, equation (3.40), and Ashby's criterion. Experimental data for alumina from Patterson [67] and Long [68]. The solid circles denote experimental data corresponding to pores that were separated from grain boundaries. (a) Simulation for $T = 1873\text{ K}$ and $P = 1\text{ atm}$, (b) for $T = 2123\text{ K}$ and $P = 1\text{ atm}$.

local criterion predicts pore separation better than Ashby's criterion. Figure 3.12 shows sintering data from Patterson using alumina [67] at $T = 2123K$. The grey-filled circles denote ambiguous data because pores were neither predominantly attached nor separated. Figure 3.12 gives no indication as to which criterion is better.

Ashby's criterion and the criterion given by equation (3.40) were further evaluated with a sign test; a form of nonparametric test from statistical methods. The test done in two parts. First, the criteria were compared to all data points corresponding to separated pores. The hypothesis for this first case was that the data for separated pores lay above and to the left of the criteria. Second, the criteria were compared to all data points corresponding to attached pores. The hypothesis for this second case was that the data for attached pores lay below and to the right of the criteria. Both tests were conservative since the data in figure 3.12 was taken as counter examples of the hypothesis. The level of significance was set at 25% for both tests. That is, there is a 25% degree of risk that the result of the tests are false. This value for the level of significance was a nearly arbitrary choice based on the author's experience with all other separation criteria.

Table 3.3 summarizes the two sign tests, one for each criteria. "Threshold Level" refers to the number of data points that must agree with the hypothesis in order for it to be accepted at the 25% level of significance. "Sample Value" refers to the number of data points that agreed with the hypothesis for each test "Decision" refers to whether or not the hypothesis is upheld at the 25% level of significance. If the data points in figure 3.12 are removed from the sign tests, the "decision" entry in the upper right hand corner of table 3.3 changes from reject to accept. All other entries remain the same.

3.7 Discussion of the Implications of the Criterion

The approach, in general, was to formulate a criterion that is a sufficient condition to show transition from one type of material behavior to another, given that the material evolution model is a system of coupled, nonlinear ODEs. This is no guarantee that the optimum criterion has been found to predict the earliest transition in material behavior. The model of grain growth rate and densification rate presented in section 3.2 yields order-of-magnitude results, as detailed by Frost and Ashby in [14]. Consequently, the predictions by the local criterion derived in section 3.5 serves as rough approximations only. The

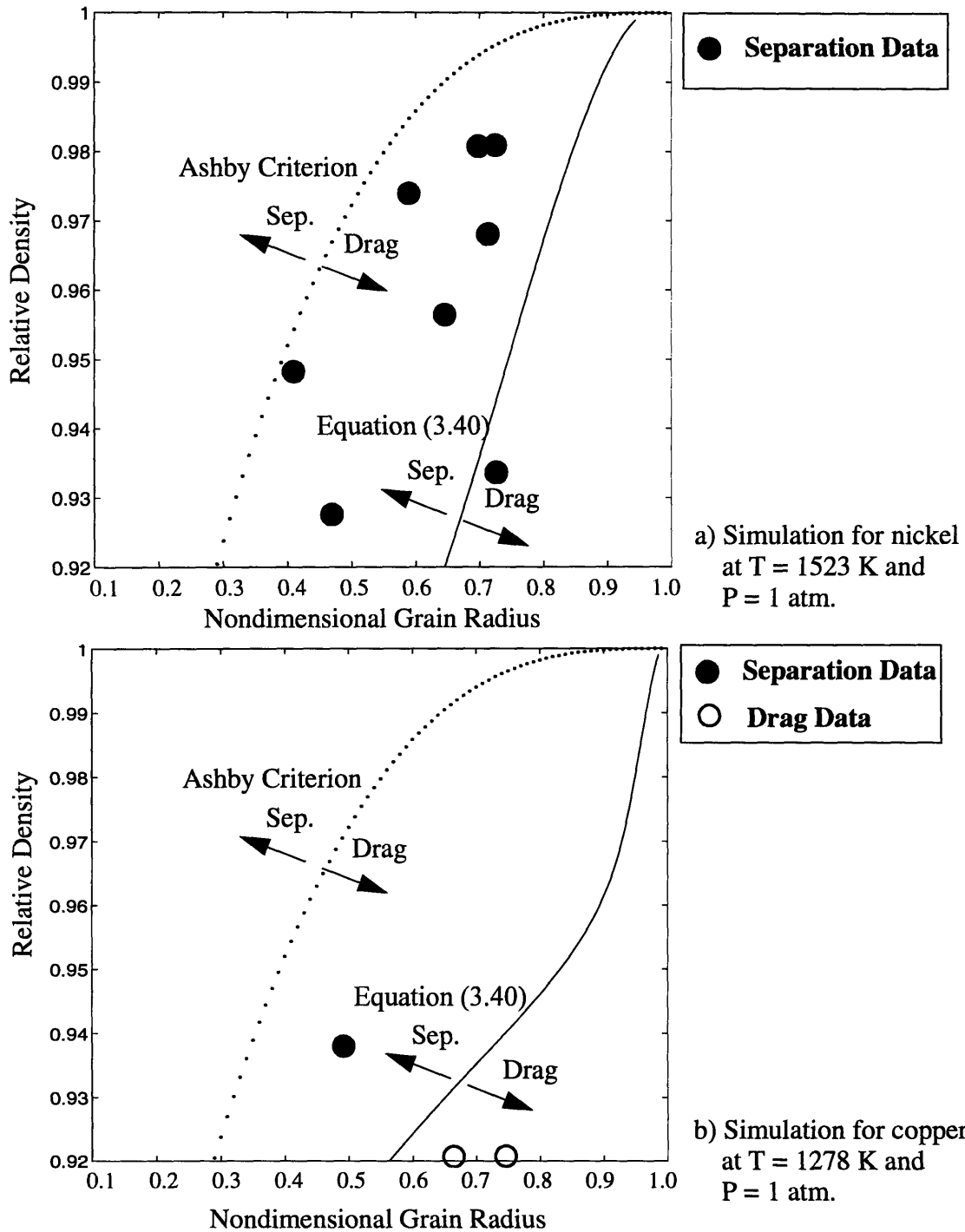


Figure 3.11 Separation criterion developed in this work, equation (3.40), and Ashby's criterion. The solid circles denote experimental data corresponding to pores that were separated from grain boundaries. a) Simulation for $T = 1523\text{ K}$ and $P = 1\text{ atm}$, experimental data for nickel from Watwe [69]. b) Hollow circles denote experimental data for pores attached to grain boundaries. Simulation for $T = 1278\text{ K}$ and $P = 1\text{ atm}$, experimental data for copper from Aigeltinger [42].

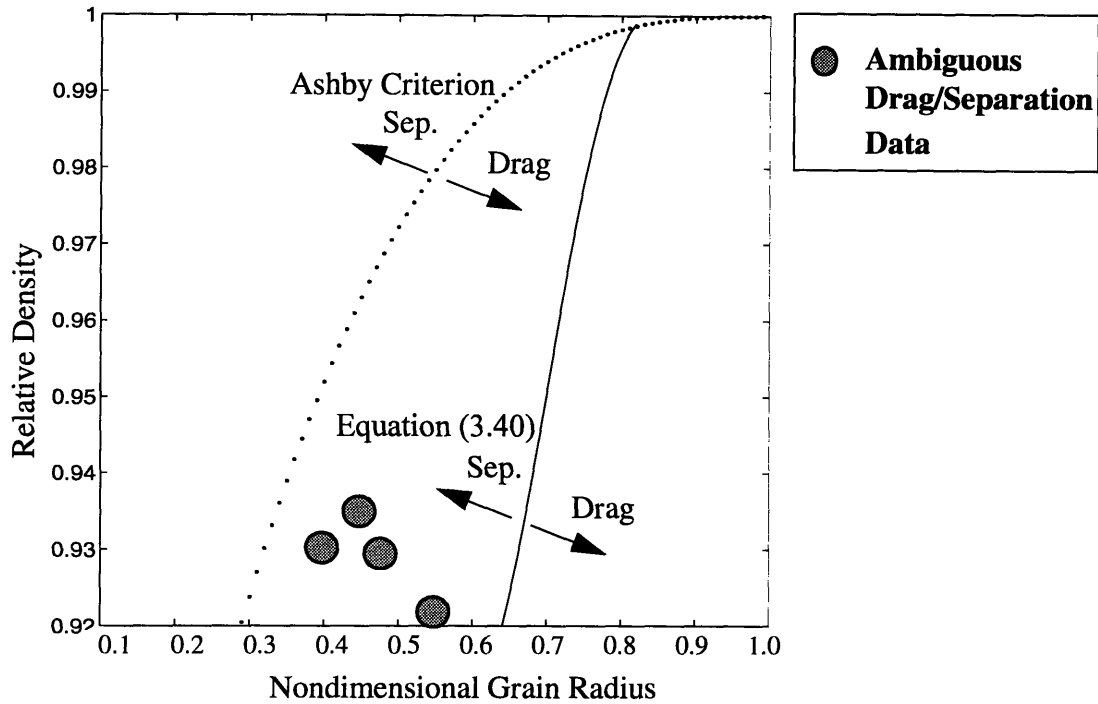


Figure 3.12 Separation criterion developed in this work, equation (3.40), and Ashby’s criterion. Grey-filled circles denote experimental data corresponding to pores that were neither predominantly attached nor separated. Simulation for $T = 2123K$ and $P = 1atm$, experimental data for alumina from Patterson [67].

	Sign test using data for separated pores.	Sign test using data for attached pores.
Local criterion, equation [3.39].	Threshold Level = 17 Sample Value = 25 Decision: accept.	Threshold Level = 5 Sample Value = 2 Decision: reject.
Ashby criterion, equation [3.19].	Threshold Level = 17 Sample Value = 15 Decision: reject.	Threshold Level = 5 Sample Value = 0 Decision: reject.

Table 3.3 Results of a sign test applied to the pore separation criteria and experimental data in figures 3.9 through 3.12.

predictions of the local pore separation criterion could be improved by using more accurate models, without altering the approach, as long as the form of the new model is a system of coupled, nonlinear, ODEs with monotonically increasing state variables.

The criterion is only applicable to relative densities where pores are closed. The criterion by Liu and Patterson [55], while modeling the process of separation as a single step, extends to accommodate open porosity.

The phase plane analysis presented in section 3.2 and the separation boundary presented in section 3.5 have implications not described in this paper that may be helpful in planning a consolidation process to either avoid pore separation or hasten its onset. Figure 3.13 shows the effects of a wide variation in temperature and pressure on the separation criterion. The maximum particle radius for this simulation was 7 microns. The implication is that the onset of separation during hot consolidation of nickel powders is sensitive to changes in temperature and pressure that the Ashby criterion is incapable of predicting.

Mathematically, the effect of variations in temperature and pressure seen in figure 3.13 is a result of changes to the relative magnitudes of the terms in equations (3.40), or equivalently, equation (3.41). The effect of variations in temperature and pressure on these equations is not obvious. In the case of equation (3.40), an increase in pressure will result in an increased rate of densification (since densification by power law creep increases, see equation (3.5)), but the effect on pore separation in terms of the relative density and average grain radius is difficult to determine since the densification rate and grain growth rate are themselves functions of relative density and average grain radius. In the case of equation (3.41), an increase in pressure changes the magnitude of a sixth-order polynomial, making the effect on pore separation criterion not obvious.

Physically, the effect of variations in temperature and pressure seen in figure 3.13 might be explained as follows. An increase in temperature increases the free energy of the system. This point is characterized in equation (3.33) where it can be seen that an increase in temperature leads to an increase in the total derivative of the free energy. Referring to figure 3.7(b), an increase in the total derivative of the free energy means that the free energy of the system is not approaching a maximum, hence separation is postponed.

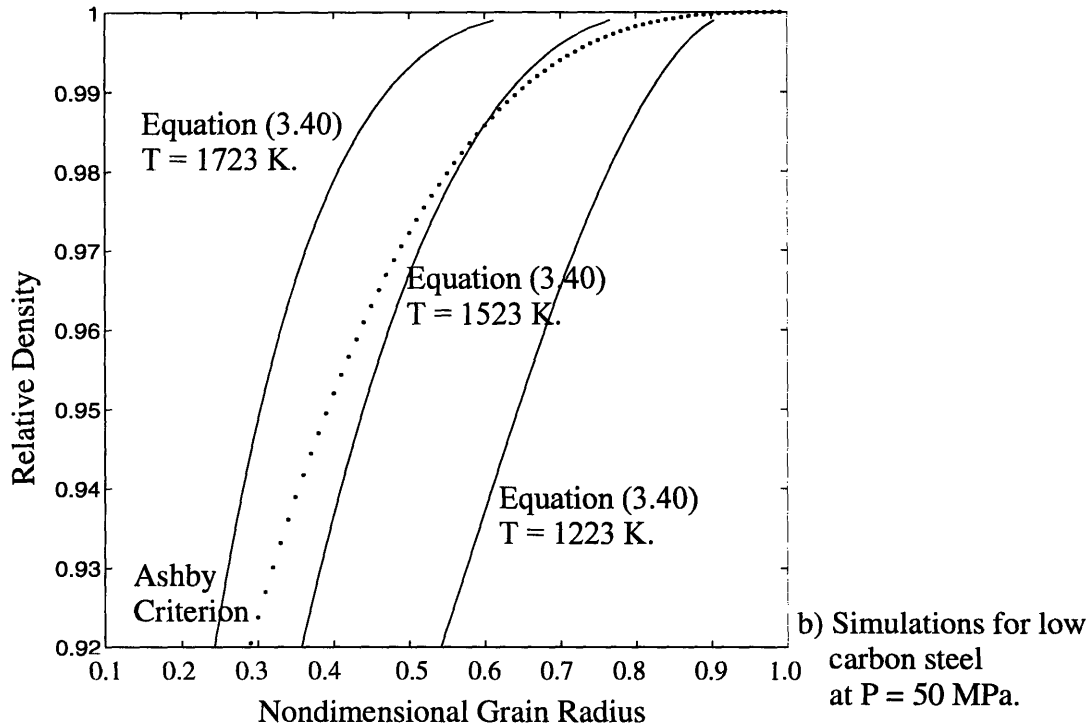
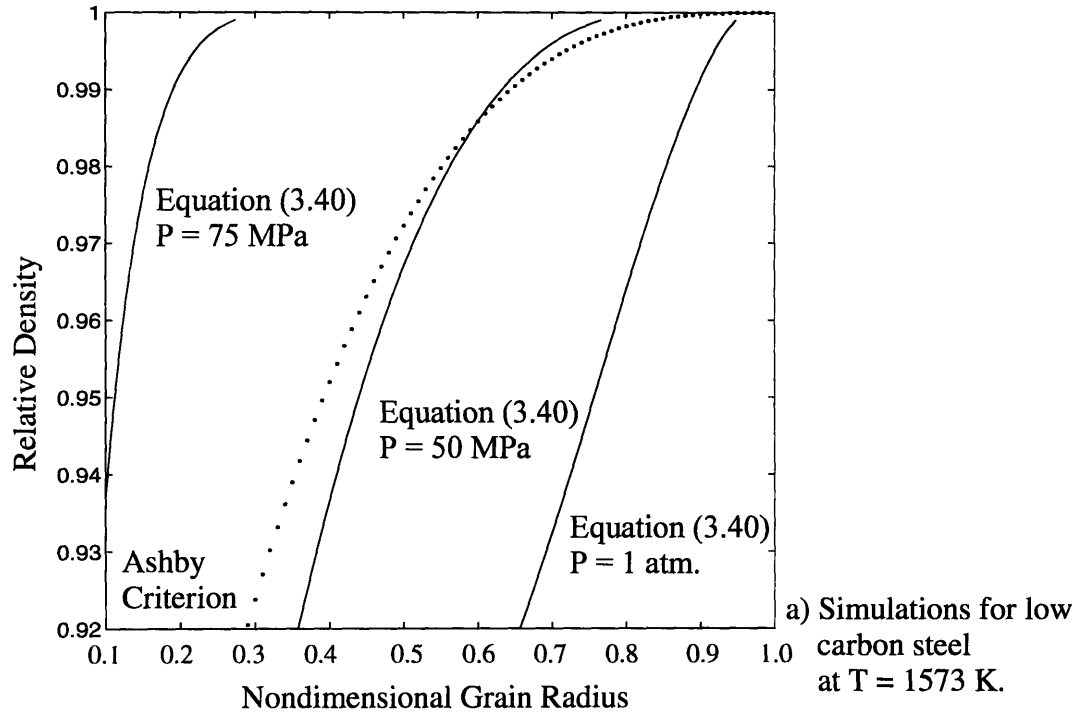


Figure 3.13 Variation in the separation criterion with changes in: a) pressure, at constant temperature $T = 1523$ K and b) temperature, at constant pressure $P = 50$ MPa, all for nickel with $R_m = 7 \mu\text{m}$.

Figure 3.13(b) shows a delay in the onset of separation as temperature increases. Physical justification for the simulated effect of pressure on separation seen in figure 3.13 is left for future work.

The effect of changing a parameter value on the pore separation criterion is shown in figure 3.14 for low carbon steel. A variation in the activation energy for core diffusion, Q_c , by only -5% results in a relatively large change in the onset of separation in terms of the relative density and average grain radius. The effect of a reducing Q_c is an increase in the rate of densification by power law creep. The increase in densification rate implies that the size of the system is shrinking faster than the case when Q_c was unmodified. An increase in the rate of shrinkage of the system implies that the free energy of the system is approaching a maximum sooner, or equivalently, for larger values of Δ and smaller values of \tilde{R} . The figure shows that the onset of separation is shifted towards larger values of Δ and smaller values of \tilde{R} . As was the case for variations in temperature and pressure, the effect of changes in material parameters on equations (3.40) and (3.41) is not obvious. However, the relatively large variation in the separation criterion for the one case illustrated by figure (3.14) serves to emphasize that the ability of the criterion to predict the onset of pore separation is rough at best. Nevertheless, the criterion presented in this chapter is the first to show the dependence of separation on internal structure, processing inputs, and material parameters.

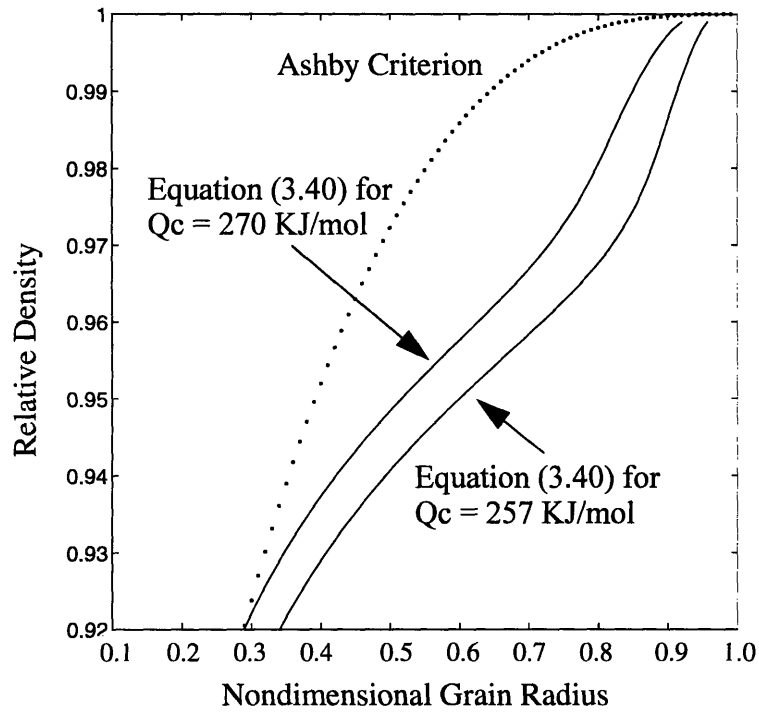


Figure 3.14 Simulated effect of a -5% change in the activation energy for core diffusion, Q_c , on the separation boundary. Simulation is for low carbon steel using parameter values from [54], at $T = 1500$ K and $P = 50$ MPa.

3.8 Nomenclature

Symbol	Definition
C_4	Constant from derivation of grain growth rate equation, 0.0438.
δD_b	Boundary diffusion coefficient.
D_c	Core diffusion coefficient.
δD_{ob}	Pre-exponential for boundary diffusion.
$\Omega^{1/3} D_{om}$	Pre-exponential for boundary mobility.
δD_{ov}	Pre-exponential for surface diffusion.
D_{ov}	Pre-exponential for volume diffusion.
D_v	Volume diffusion coefficient.
\tilde{F}_2	Dimensionless driving force for densification.
k	Boltzmann's constant.
n	Power law creep exponent.
N	Nominal number of pores attached to a grain boundary.
P	Applied external pressure.
P_i	Gas pressure inside a closed pore, as a function of relative density.
P_o	Outgassing pressure (atmospheric pressure usually).
Q_b	Activation energy for boundary diffusion.
Q_c	Activation energy for core diffusion.

Symbol	Definition
Q_m	Activation energy for boundary mobility.
Q_s	Activation energy for surface diffusion.
Q_v	Activation energy for volume diffusion.
r	Mean pore radius.
R	Mean grain radius.
R_g	Ideal gas constant.
R_m	Maximum grain radius (taken equal to maximum particle radius).
\tilde{R}	Nondimensionalized grain radius, $\tilde{R} = R/R_m$
S_{ref}	Reference stress for power law creep.
T	Temperature.
T_m	Melting temperature.
$z_i, i=1,2,3,\dots$	State variables in general.
Δ	Relative density.
$\dot{\Delta}_{bd}$	Contribution of boundary diffusion to the densification rate.
Δ_c	Relative density at pore closure (approximately 0.92).
$\dot{\Delta}_{NHC}$	Contribution of Nabarro-Herring/Coble creep to the densification rate.
$\dot{\Delta}_{vd}$	Contribution of volume diffusion to the densification rate.
γ	Surface energy.
G	Free energy

Symbol	Definition
f	Packing density of atoms in a grain boundary.
π	3.1459265 . . .
θ	Angle of inclination of pore/grain boundary intersection, figure 3.4.
Ω	Atomic or molecular volume.

CHAPTER 4 Formulating a Characteristic Time

Each criterion derived in chapters 2 and 3 can be mathematically interpreted as a boundary that separates the state space of a material into two regions. One region corresponds to the material prior to a transition in behavior, the other region after the transition. In this chapter the focus is on the region prior to the transition. An attempt is made to develop a systematic approach to formulating a characteristic time for a state trajectory to cross the transition boundary, given an initial state. As in the previous chapters, the material behavior is assumed to be governed by coupled, simultaneous kinetic processes. The characteristic time is a function of the internal variables, process input variables, and material parameters. Simulating the time to the transition by numerical integration of the kinetic equations from an initial state does not provide as clear a relation between the internal variables, process input variables, material parameters, and time. Conversely, a characteristic time is approximate and will never be a substitute for numerical integration when the goal is a (model-exact) time to the transition. The characteristic time can aid the design of processing inputs, such as temperature and strain rate for an extrusion process, to predict the rate of approach to the transition.

The formulation of the characteristic time is shown, however, to be incomplete. Approaches for improvement are outlined. The approach is then applied to pore separation to highlight the unresolved issues.

4.1 Previous Work to Derive a Characteristic Time

This section describes previous work to derive a characteristic time for phenomena governed by multiple kinetic processes. The first section gives an example from chemical engineering that is typical of the most widely-practiced approach to developing time constants for phenomena governed by multiple kinetic processes. The approach divides the analysis by considering process conditions whereby one of the kinetic processes dominates over the others, and then analyzes each process separately in turn. The second section discusses mathematically more advanced approaches to analyze systems of

ordinary differential equations than the most widely-practiced approaches. The examples in the second section are closer to the approach taken in this work to develop convergence rate criteria for dynamic recrystallization and pore separation. These transitions have coupled kinetic processes that are simultaneous over a wide region of operating conditions and do not fall easily into categories whereby one of the kinetic processes dominates over the others.

4.1.1 Widely Practiced Approaches

Chemical reactions of complex systems involve multiple kinetic processes. Levenspiel [4] presents a good review of mathematical models of complex chemical reactions and gas/solid reactions in particular. In the treatment by Levenspiel, gas/solid reactions are treated as a single spherical particle interacting with a gaseous reservoir. This development is valid for liquids as well as gases. The analysis is divided into two models: one, the particle shrinks as it reacts with the gas, and two, the particle retains its original size as it reacts. Both models follow similar lines to derive a characteristic time. The development for a particle of unchanging size, called the unreacted core model, will be discussed here.

The unreacted core model approximates reactions such as burning coal or wood. If gaseous products are formed, there are five steps in the overall reaction. If no gaseous products are formed, this model assumes the overall reaction proceeds with three successive steps. The latter case is examined here without loss of generality. The three steps are: one, diffusion of gaseous reactant to the surface of the ash surrounding the solid particle, two, diffusion of the gaseous reactant through the ash to the solid surface of the unreacted core, and three, chemical reaction of the of the gaseous reactant with the unreacted core. Each of these three steps is considered a resistance to the overall progress of the reaction. Depending on operating conditions (size of the solid particles, solid porosity, and temperature of the reaction), one of these resistances may dominate the others, then that one resistance is the rate-controlling step of the reaction. The analysis proceeds by modelling each step, in turn, using conservation of mass and Fick's first law. The result is a single, first order differential equation for each step. Each equation is solved, independent of the others, for time. The characteristic time for each step is taken

as the time for the unreacted core to vanish, i.e. solving for time when the radius of the unreacted core is set to zero. The result is three characteristic times, each as a function of the size of the particles, material parameters, and, implicitly, the process conditions whereby the analysis was separate for each step.

4.1.2 Mathematically More Advanced Approaches

There have been efforts to analyze systems with multiple kinetic processes without resorting to dividing the processes into categories where one process dominates over the others. These efforts apply more advanced mathematics than is used in the previous example of gas/solid interactions. Original work by Lyapunov, as detailed by Drazin [70], and work by Slotine and Li [9] are more mathematically advanced than the approach described for gas/solid reactions.

Lyapunov exponents are a measure of the growth or decay of the separation of neighboring trajectories of an attractor. A Lyapunov exponent based on a system of nonlinear, coupled ordinary differential equations summarizes the complex growth or decay of the neighboring trajectories of this system as a single function. This concept of a single function to describe the time-rate of change of simultaneous kinetic processes is essential to the approach in my work, with one refinement. In the development presented in section 4.2, the characteristic time is refers to the approximate time it takes for a trajectory to reach a boundary in the state space of the system. The boundary is the same boundary derived in section 2.4.1 that indicates the transition in material behavior in terms of the states of the system and material parameters. In the Lyapunov analysis, the decay/growth rate is with respect to neighboring trajectories of an attractor, equilibrium point, or more generally, an omega-limit set.

Slotine and Li [9] estimate convergence rates for systems of nonlinear ordinary differential equations, and implicitly, divergence rates as well. The rate of convergence refers to the rate of convergence of a trajectory to an attractor, not the rate of convergence of a trajectory to an arbitrary boundary in the state space of the system as is the goal of section 4.2. Slotine and Li begin their analysis with a candidate Lyapunov function and its derivative with respect to time. In some cases this derivative can be algebraically manipulated into a differential equation that has a closed form solution. The solution can

sometimes be solved directly for time, or have a form that can be bounded by a simpler function which has an obvious convergence rate. Section 4.2 will detail this approach with an example. The development in section 4.2 then goes on to propose a structured approach to derive a characteristic time for systems with simultaneous, coupled kinetic processes.

4.2 Approach in General

The approach is to bound the rate of convergence of $\Phi(\underline{z})$, where $\Phi(\underline{z})$ is the symbol given in chapter 2, section 2.4 to the general form of a summarizing function, starting with the initial value $\Phi(\underline{z}_0)$, i.e. $\Phi(\underline{z}) = \Phi(\underline{z}_0)$ at $t = 0$, to a value $\Phi(\underline{z}_b)$ associated with the transition boundary. This section starts by giving an example of the bounding approach and then proposing a generalization.

One example of a convergence rate criterion for $\Phi(\underline{z})$ may be obtained by algebraically manipulating the terms in

$$\dot{\Phi} = \dot{\Phi}(\underline{z}) \quad (4.1)$$

to form the scalar linear differential equation

$$\dot{\Phi} = -\lambda(\underline{z})\Phi + f(\underline{z}). \quad (4.2)$$

The general solution of this differential equation is [71]

$$\Phi(t) = C \exp\left[\int -\lambda dt\right] + \exp\left[\int -\lambda dt\right] \int f \exp\left[\int \lambda dt\right] dt \quad (4.3)$$

where C is a constant. If $\lambda(\underline{z})$ and $f(\underline{z})$ are substituted by the upper the bounds on them, λ_u and f_u , where the “u” subscript denotes “upper”, then equation (4.3) simplifies to:

$$\Phi_u(t) = C \exp\left(-\lambda_u t\right) + \frac{f_u}{\lambda_u}. \quad (4.4)$$

Applying the initial condition $\Phi(\underline{z})|_{t=0} = \Phi(z_0)$, results in:

$$\Phi_u(\underline{z}) = \left(\Phi(z_0) - \frac{f_u}{\lambda_u} \right) \exp(-\lambda_u t) + \frac{f_u}{\lambda_u} \quad (4.5)$$

or

$$\Phi_u(\underline{z}) = \Phi_{uss} [1 - \exp[-\lambda_u t]] + \Phi(z_0) \exp[-\lambda_u t] \quad (4.6)$$

where $\Phi_{uss} = \lim_{t \rightarrow \infty} \Phi_u = \frac{f_u}{\lambda_u}$ provided $\lambda_u > 0$. Then if $\lambda_u = \text{lub} \lambda(t)$ and $\lambda_u > 0$, and if $f_u = \text{lub} f(t)$, then $\Phi_u(t) > \Phi(t) \quad \forall t$.

An example of the bound given by equation (4.6) is depicted in figure 4.1. The bound given by equation (4.6) has the characteristic time $\tau_u = \frac{1}{\lambda_u}$.

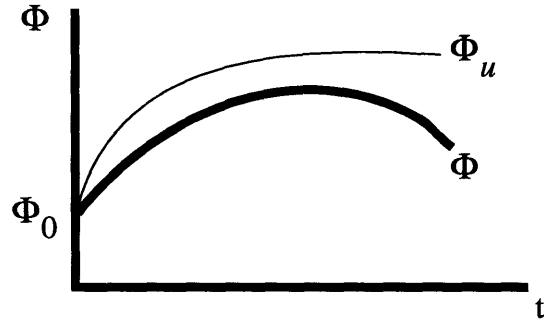


Figure 4.1 An example of the upper bound on Φ given by equation (4.6).

In addition to the requirements on λ_u above, if λ_u is also the same functional form of the expression $\lambda(\underline{z})$, say using the state's initial values $\lambda_u = \lambda(\underline{z})|_{t=0} = \lambda_u(z_0)$, then the characteristic time $\tau_u = 1/\lambda_u(z_0)$ is a function of material parameters and the initial state of the system (the internal variables at $t = 0$). Process inputs, such as temperature and strain rate, appearing in $\lambda_u(z_0)$ can be treated as parameters if they are constant, a reasonable assumption for many production processes. This example can be easily

extended to formulate a lower bound. Having both an upper and a lower bound would provide insight into the tightness of the bound.

This approach is analogous to a solution estimation technique using matrix measures, applicable to a certain class of nonlinear differential equations [13]. Matrix measures can in some practical cases be used to upper and lower bound the convergence rate of the norm of the state vector, $\|\underline{x}(t)\|$. In this treatment $\lambda_{\underline{u}}(\underline{z}_0)$ and $\dot{\Phi}(\underline{z})$ are analogous to a matrix measure and $\|\underline{x}(t)\|$ respectively, noting that $\|\underline{x}(t)\|$ is a special kind of summarizing function. Typically, convergence criteria are associated with the convergence of a state trajectory to an equilibrium point. Here convergence criteria are adapted to obtain a characteristic time associated with a boundary in state space, i.e. the boundary describing the transition in material behavior developed in chapter 2, section 2.4.

The remainder of this section is an attempt at a systematic approach to formulating a characteristic time. The approach I take is to propose a simple, canonical equation to bound a function in the hope that a simple expression for a characteristic time will result and that the tightness of the bound will be easy to evaluate. The development is shown to be incomplete and approaches for improvement are outlined. The incomplete approach is then applied to dynamic recrystallization and pore separation to explicitly show the unresolved issues.

The functional form given by $\Gamma = 1/\lambda_{\underline{u}}(\underline{z}_0)$ is not unique. Alternate functions can be obtained depending on how $\dot{\Phi} = \dot{\Phi}(\underline{z})$ is manipulated to yield $\lambda(\underline{z})$ and $f(\underline{z})$ in equation (4.2). In addition, convergence rates with characteristic times different from $\tau_{\underline{u}} = 1/\lambda_{\underline{u}}(\underline{z}_0)$ can be derived by choosing to solve differential equations other than equation (4.2). For instance, a line $\dot{\Phi} = \text{constant}$, a parabola $\dot{\Phi}\Phi = \text{constant}$, or hyperbola $\dot{\Phi}/\Phi^2 = \text{constant}$. From among these alternatives the best is the one which relates a sufficient range of values of material parameters and internal variables with the tightest bounds.

Rather than search for the tightest bound amongst alternatives, the following argues that a simple alternative exists from which many others can be derived. Equation (4.2) serves as a good example to present this argument. In equation (4.2), $\dot{\Phi}(\underline{z})$ can be factored from the two terms on the left hand side to yield:

$$\dot{\Phi} = \left[\lambda(\underline{z}) + \frac{f(\underline{z})}{\Phi(\underline{z})} \right] \Phi(\underline{z}) . \quad (4.7)$$

The term in brackets could be called a new variable, say $\tilde{\lambda}$:

$$\dot{\Phi} = \tilde{\lambda} \Phi(\underline{z}) . \quad (4.8)$$

Equation (4.8) can be used to form a bound on the evolution of $\Phi(\underline{z})$ in a fashion similar to the way equation (4.2) was used to bound the evolution of $\Phi(\underline{z})$. The general solution to equation (4.8) is:

$$\Phi = \Phi_0 \exp \int_0^t \tilde{\lambda}(s) ds . \quad (4.9)$$

If a constant, λ_u , is chosen such that $\lambda_u \geq \tilde{\lambda}(t) \quad \forall t$, then the following inequality is true.

$$\Phi_u = \Phi_0 e^{\lambda_u t} \geq \Phi_0 \exp \int_0^t \tilde{\lambda}(s) ds = \Phi(\underline{z}) \quad (4.10)$$

where the characteristic time of the upper bound on the evolution in $\Phi(\underline{z})$, Φ_u , is $\Gamma = 1/\lambda_u$.

Supposed, instead of starting with equation (4.2), the differential equation $\dot{\Phi}\Phi = \text{constant}$ had been used. $\dot{\Phi}\Phi = \text{constant}$ can be algebraically manipulated to give $\dot{\Phi} = \left[\frac{\text{constant}}{\Phi^2} \right] \Phi$. The term in brackets is then renamed $\tilde{\lambda}(\underline{z})$ and then equations (4.8), (4.9), and (4.10) follow as before. Many differential equations can be manipulated to form equation (4.8) because, as the step from equations (4.7) to (4.8) illustrates, $\Phi(\underline{z})$ need only be factored out of the equation.

So far it has been argued that many differential equations can be used to bound the evolution of $\Phi(\underline{z})$ and that these alternatives can be simplified to the form given by equation (4.8). Each differential equation will result in a new expression for $\tilde{\lambda}(\underline{z})$ in

equation (4.8). Instead of investigating all possible forms $\tilde{\lambda}(\underline{z})$, a unique $\tilde{\lambda}(\underline{z})$ can be obtained by defining $\tilde{\lambda}(\underline{z})$ as follows:

$$\tilde{\lambda}(\underline{z}) \equiv \frac{\dot{\Phi}}{\Phi} . \quad (4.11)$$

Equation (4.11) is proposed as a single basis for bounding the evolution of a wide variety of $\Phi(\underline{z})$ and deriving a characteristic time. This choice is motivated for two reasons. One, its general solution, equation (4.9) is an exponential form, therefore a characteristic time derived from this form has seen wide use in engineering. A characteristic time derived from some other bound will not have such a wide-spread interpretation. Two, the simplicity of equation (4.11) suggests that further analysis may be kept simple, as has already been seen in forming a bound, equation (4.10).

Deriving a characteristic time based on equation (4.11) proceeds in the same way as the example beginning with equation (4.8), i.e. equation [4.9] is the general solution of equation (4.11) and equation (4.10) gives an upper bound on $\Phi(\underline{z})$ given the restriction on $\tilde{\lambda}_u$. The characteristic time $\Gamma = 1/\tilde{\lambda}_u$ depends on the choice of $\tilde{\lambda}_u$. In the example, choosing $\tilde{\lambda}_u$ was ad-hoc. A better way to choose $\tilde{\lambda}_u$ is to map the feature in the evolution of $\Phi(\underline{z})$, used to define the transition boundary, to the evolution in $\tilde{\lambda}(\underline{z})$, and then choose a suitable $\tilde{\lambda}_u$ with this additional insight. This point is illustrated by the following examples.

Figure 4.2 sketches an example of a $\Phi(\underline{z})$ evolving with time mapped to the evolution in $\tilde{\lambda}(\underline{z})$. The maximum in $\Phi(\underline{z})$ corresponds to the zero-crossing in $\tilde{\lambda}(\underline{z})$. Using the upper bound on $\Phi(\underline{z})$ given by equation (4.11), the least conservative upper bound will result from choosing $\tilde{\lambda}_u = lub\tilde{\lambda}(t) = \tilde{\lambda}_0 \Rightarrow \Gamma = \frac{1}{\tilde{\lambda}_0}$.

If $\Phi(\underline{z})$ evolves as sketched in figure 4.3 instead of the previous example, then the least conservative upper bound will result from choosing $\tilde{\lambda}_u = lub\tilde{\lambda}(t) = \tilde{\lambda}\Big|_{\tilde{\lambda}=0} \Rightarrow \Gamma = \frac{1}{\tilde{\lambda}_{max}}$.

If $\Phi(\underline{z})$ evolves as sketched in figure 4.4, then the least conservative lower bound will result from choosing $\lambda_u = glb\lambda(t) [0 < t < t_{trans}] = \lambda_0 \Rightarrow \tau = \frac{1}{\lambda_0}$.

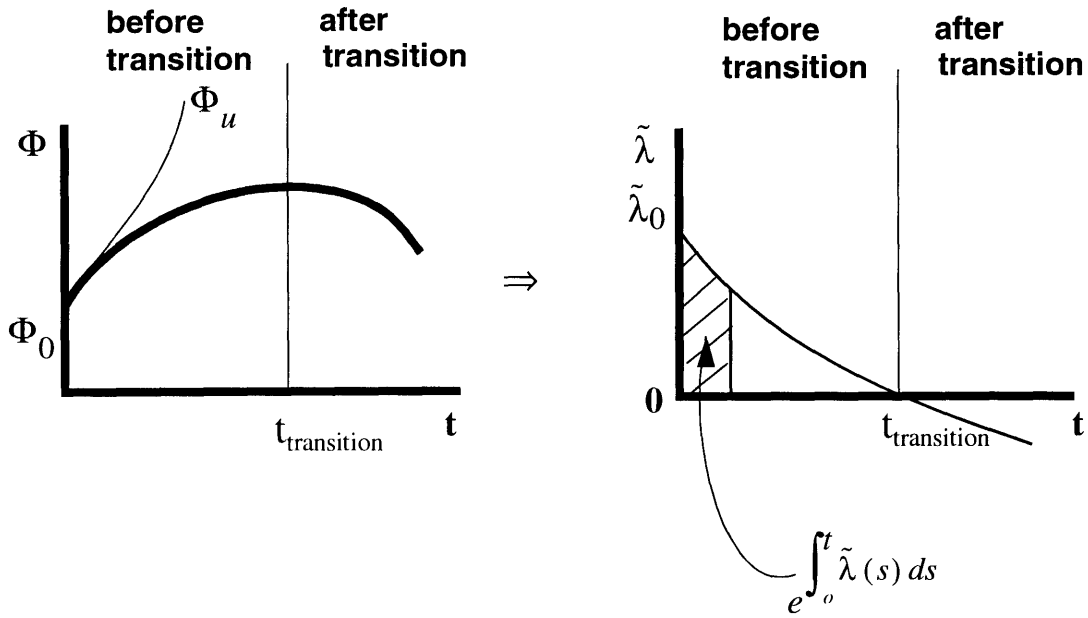


Figure 4.2 Example of mapping an evolution in $\Phi(\underline{z})$ to $\tilde{\lambda}(\underline{z})$.

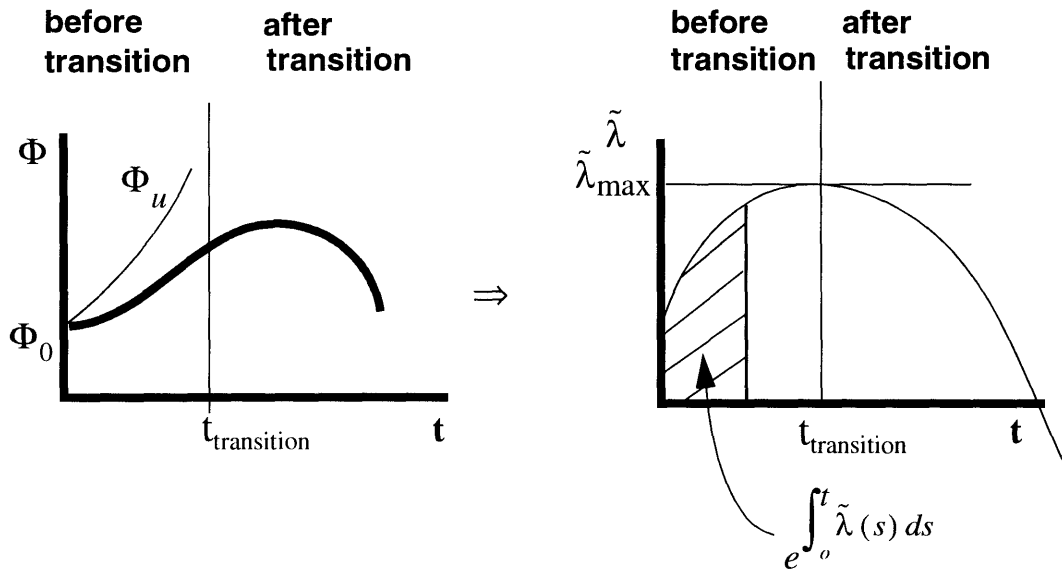


Figure 4.3 Example of mapping an evolution in $\Phi(\underline{z})$ to $\tilde{\lambda}(\underline{z})$.

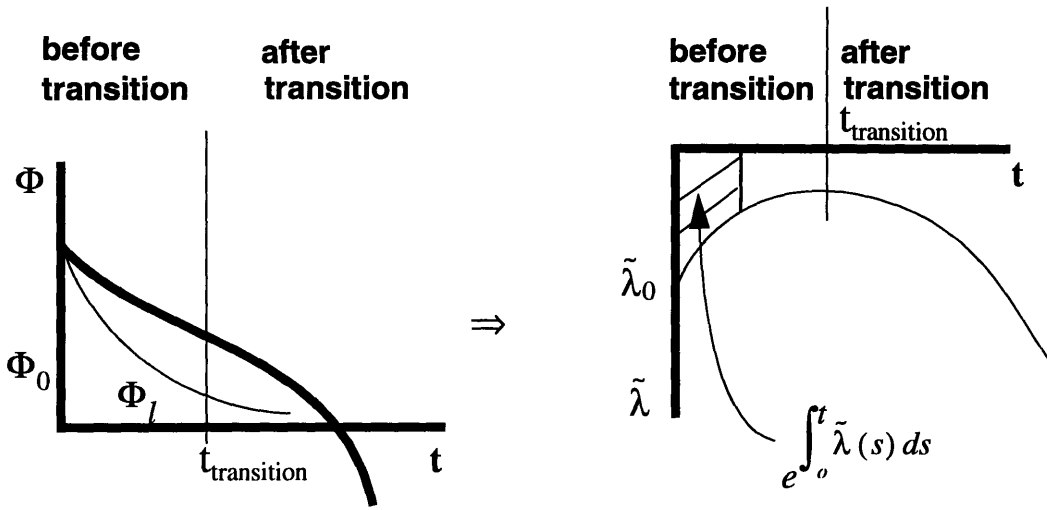


Figure 4.4 Example of mapping an evolution in $\Phi(z)$ to $\tilde{\lambda}(z)$.

As a final example, if $\Phi(z)$ evolves as sketched in figure 4.5, then the least conservative lower bound will result from choosing $\tilde{\lambda}_u = glb \tilde{\lambda}(t) = \tilde{\lambda}_0 \Rightarrow \tau = \frac{1}{\lambda_0}$.

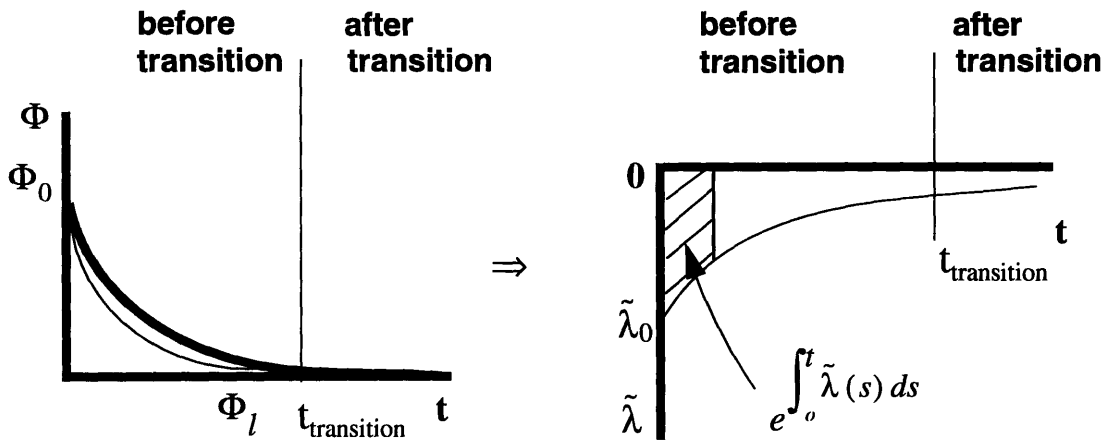


Figure 4.5 Example of mapping an evolution in $\Phi(z)$ to $\tilde{\lambda}(z)$.

4.3 Unresolved Issues of this Approach

The approach described in the previous section to derive a characteristic time based on

equation (4.11) does not guarantee that the characteristic time will remain proportional to the actual time-to-transition. There are examples when a change in the value of an initial condition will result in the characteristic time increasing while the actual time-to-transition decreases. To illustrate, this section begins by interpreting the characteristic time graphically for a particular $\Phi(z)$, and then points out at least two cases when this characteristic time fails to be proportional to the actual time-to-transition. A solution to the first case is proposed. A solution for the second case is not offered. The approach proposed here should not be used until it is proven that the characteristic time remains proportional to the actual time-to-transition for any $\Phi(z)$, or at least for a specific $\Phi(z)$.

Figure 4.6 depicts a geometric interpretation of a characteristic time for the particular $\Phi(z)$ depicted in figure 4.2, as follows. The equation for the tangent to $\Phi(t)$ at Φ_0 is:

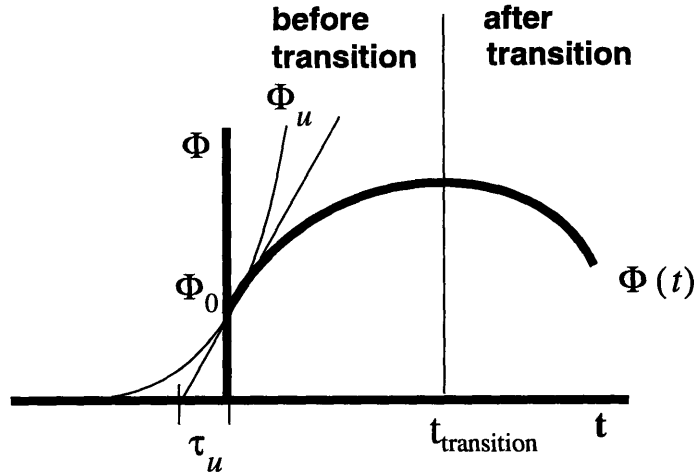


Figure 4.6 Geometric interpretation of the characteristic time based on the upper bound Φ_u , for the specific evolution in $\Phi(z)$ shown.

$$\Phi_u = \dot{\Phi}_0 t + \Phi_0 . \tag{4.12}$$

Solving equation (4.12) for the time t when $\Phi_u = 0$ gives:

$$t|_{\Phi_u = 0} = \frac{\Phi_0}{\dot{\Phi}_0} = \frac{1}{\lambda_0} \equiv \tau_u . \tag{4.13}$$

So, the characteristic time of the upper bound Φ_u is the familiar exponential time constant of the decay of Φ_u to zero as $t \rightarrow -\infty$. Equivalently, the characteristic time proposed by this approach amounts to a simple linear bound.

For τ_u to be proportional to the actual time-to-transition, $t_{\text{transition}}$, the tangent at Φ_0 must remain sandwiched between the upper bound Φ_u and $\Phi(t)$. The tangent at Φ_0 does not remain sandwiched when $\Phi(t)$ no longer has the shape in figure 4.6, but takes on the shape shown in figure 4.7. $\Phi(t)$ could change shape like this as the result of

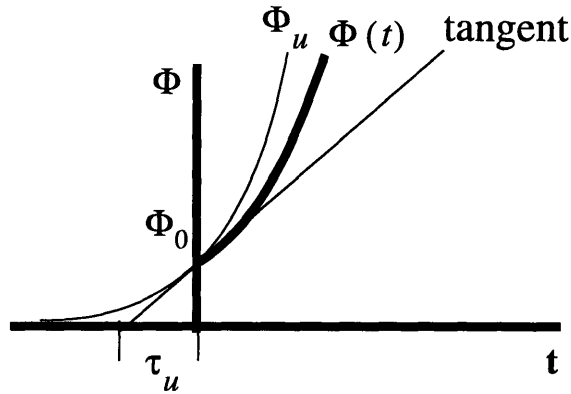


Figure 4.7 Case in which τ_u fails as a prediction of $t_{\text{transition}}$.

changes in the parameter values or initial conditions of the kinetics expressions. But the characteristic time, τ_u , is only useful when changes in the values of the initial conditions and parameter values can be explored for their approximate effect on the time-to-transition.

One way to ensure that $\Phi(t)$ holds the shape depicted in figure 4.6, i.e. $\Phi(t)$ evolves with a single maximum, is to require that $\Phi > 0$, $\dot{\Phi} > 0$, and $\ddot{\Phi} < 0$. These requirements on Φ and its derivatives have the following implications on the function λ_u , in addition to the conditions mentioned in section 4.2. The first two requirements, $\Phi > 0$, $\dot{\Phi} > 0$, give:

$$\dot{\Phi} = \lambda_u \Phi > 0 \Rightarrow \lambda_u > 0 . \quad (4.14)$$

Equation (4.14) is easily satisfied by ensuring that changes in the values of the initial conditions and parameter values result in λ_u staying positive.

The third requirement, $\ddot{\Phi} < 0$, gives:

$$\ddot{\Phi} = \lambda_u \dot{\Phi} + \dot{\lambda}_u \Phi < 0 \Rightarrow \Phi [\lambda^2 + \dot{\lambda}_u] < 0 \Rightarrow \lambda^2 < -\dot{\lambda}_u . \quad (4.15)$$

These restrictions, equations (4.14) and (4.15), on the function λ are equivalently restrictions on the values of the initial conditions and parameter values because λ_u is itself a function of the states of the system and $\dot{\lambda}_u$ is a function of the states and their derivatives (which are themselves a function of the states and parameter values as given by the kinetics expressions comprising the internal variable model).

Equations (4.14) and (4.15) are difficult to evaluate except for the most simple cases where the internal variable models are both low in order and have simple nonlinearities. For this reason alone the approach taken in section 4.2 has to be investigated further. Another drawback, for which no solution is offered, occurs when the shape of $\Phi(t)$ evolves in a more subtle manner than the change in shape illustrated in going from figure 4.6 to 4.7. Figure 4.8 depicts the problem. Again, the result is that the characteristic time, τ_u , is not proportional to the time-to-transition, $t_{\text{transition}}$. In the figure, for the change in

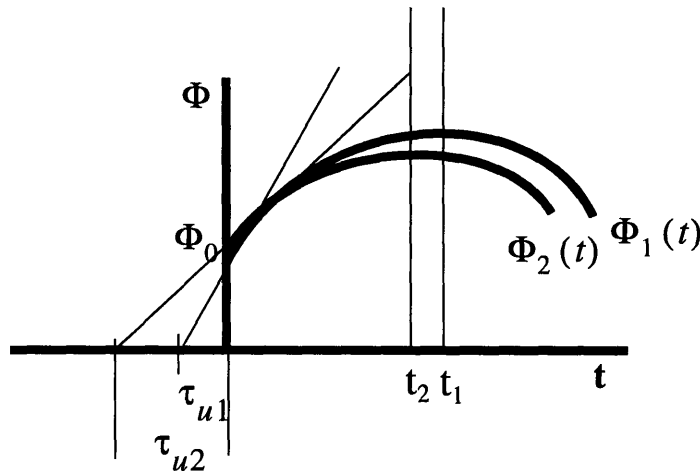


Figure 4.8 Example of changes in the shape of $\Phi(t)$ which result in the characteristic time, τ_u , not being proportional to the time-to-transition, $t_{\text{transition}}$.

shape from $\Phi_1(t)$ to $\Phi_2(t)$ the time-to-transition decreases from t_1 to t_2 but the characteristic time increases from τ_{u1} to τ_{u2} . As in the previous example, the change in shape in $\Phi(t)$ could result from changes in the values of the initial conditions or parameter values, which renders predictions by the time constant useless.

4.4 A Characteristic Time for Pore Separation

In this section a characteristic time for pore separation is derived to explicitly show how the approach outlined in section 4.2 is implemented. Predictions by the time constant agree well with numerical simulations of the model-exact time-to-separation, but, as shown in section 4.3, the time constant has not been proven to be proportional to the time-to-separation. The basis for the approach applied to pore separation is the local geometric model depicted in figure 3.4.

The derivation of a time constant for pore separation follows the same steps as outlined in section 4.2. Recall from section 3.5 that the free-energy of the system serves as the function $\Phi(z)$. Begin with the integrated form of equation (3.33) where $n = 3fA/\pi a^2$ and $A = A_{\text{cone}} = 0.432\pi rR$ as discussed in section 3.5:

$$G = \left[u \cdot \frac{3fA}{\pi a^2} - Ts \cdot \frac{3fA}{\pi a^2} + \gamma A \right] = \left[\frac{3f}{\pi a^2} (u - Ts) + \gamma \right] \cdot 0.432\pi rR . \quad (4.16)$$

The derivative of this equation with respect to time is

$$\dot{G} = 0.432\pi \left[\frac{3f}{\pi a^2} (u - Ts) + \gamma \right] [r\dot{R} + R\dot{r}] . \quad (4.17)$$

Now using equation (4.16), solve for r

$$r = \frac{G}{\left[\frac{3f}{\pi a^2} (u - Ts) + \gamma \right] (0.432\pi R)} \quad (4.18)$$

and again from equation (4.16), solve for R

$$R = \frac{G}{\left[\frac{3f}{\pi a^2} (u - Ts) + \gamma \right] (0.432\pi r)} . \quad (4.19)$$

Substituting equations (4.18) and (4.19) into equation (4.17) yields:

$$\begin{aligned} \dot{G} &= \lambda G \\ \lambda(t) &\equiv \frac{\dot{R}}{\bar{R}} + \frac{\dot{r}}{r} \end{aligned} \quad (4.20)$$

The general solution of equation (4.20) is

$$G = G_0 \exp\left(\int_0^t \lambda d\tau\right) \quad (4.21)$$

where $G_0 \equiv G|_{t=0}$. If a constant, call it λ_u , can be found such that $\lambda_u > \lambda(t) \quad \forall t$, then

$$G_u(t) = G_0 \exp(\lambda_u t) \geq G_0 \exp\left(\int_0^t \lambda d\tau\right) = G(t), \quad (4.22)$$

i.e. $G_u(t)$ is an upper bound on $G(t)$. A suitable λ_u based on the functional form of $\lambda(t)$ in equation (4.20) is:

$$\lambda_u = \frac{\tilde{R}_0}{\tilde{R}_0} - \frac{\tilde{r}_0}{r_0} > \frac{\tilde{R}}{\tilde{R}} + \frac{\tilde{r}}{r} = \lambda(t) \quad (4.23)$$

where the subscript “0” denotes the variable’s value at $t = 0$. This inequality is easily verified given the following two assumptions. One, the initial grain growth rate and the absolute value of the pore shrinkage rate are larger than subsequent rates, $\tilde{R}_0 > \tilde{R}(t)$ and $|\tilde{r}_0| > |\tilde{r}(t)|$. Two, the average grain radius grows monotonically, $\tilde{R}_0 < \tilde{R}(t)$, and the average pore radius shrinks monotonically, $r_0 > r(t)$.

Using equation (4.23), a characteristic time for the onset of pore separation is then

$$\tau_u = \frac{1}{\lambda_u} = \frac{1}{\frac{\tilde{R}_0}{\tilde{R}_0} - \frac{\tilde{r}_0}{r_0}} = \frac{1 - \Delta_0}{\dot{\Delta}_0} \quad (4.24)$$

where the last term was formed by substituting equation (3.20), and its derivative at $t = 0$, for r_0 and \dot{r}_0 respectively. Figure 4.9 shows a simulation comparing $G(t)$ from equation (4.16) to $G_u(t)$ from equation (4.22) using the internal variable model for the evolution of R and Δ given in section 3.2. The figure indicates that the characteristic

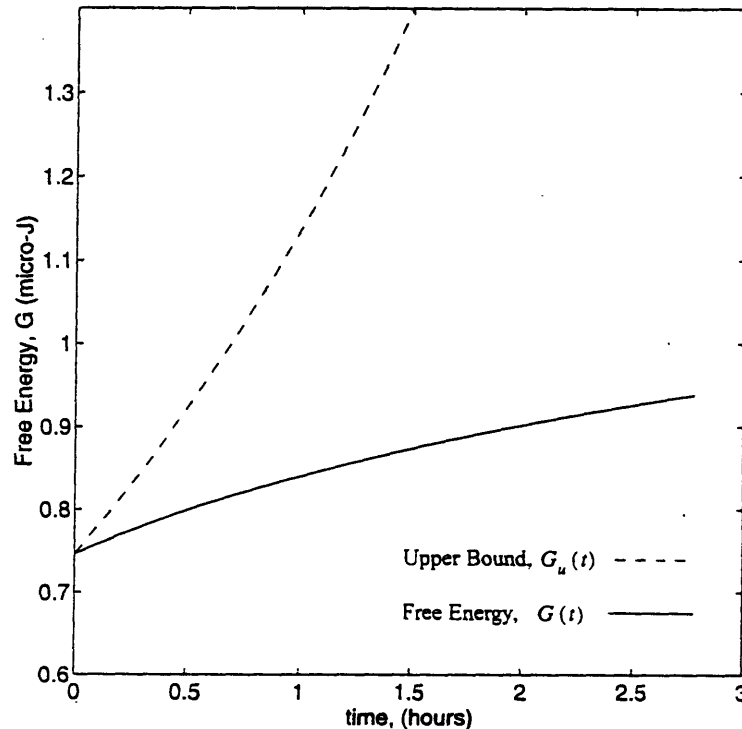


Figure 4.9 Simulation of the upper bound on the free energy $G_u(t)$, equation (4.22), and the free energy $G(t)$, equation (4.16) using copper parameter values listed in [14] where $\Delta_0 = 0.92$ and $\dot{R}_0 = 0.25$ with $T = 1300$ K and $P = 1$ atm.

time given by equation (4.24) yields very conservative estimates of the actual time-to-transition. In the next section the accuracy of the upper bound on the characteristic time will be investigated further.

4.5 Comparison to Simulations

Experimental data to test the characteristic time for pore separation, equation (4.24), is not available. In this section the characteristic time is compared to simulations that show, qualitatively, the ability of the characteristic time to predict the effect of changes in initial conditions and parameter values on the time-to-separation.

The method presented here to derive a characteristic time for separation is based on the upper bound $G_u(t)$, equation (4.22). The characteristic time is therefore an inherently conservative estimate of the time-to-transition. The approach can be easily extended to generate another characteristic time based on a lower bound. This characteristic time would nonconservative. Since a conservative characteristic time is of greater practical interest to persons planning a consolidation process than a nonconservative characteristic time, an analysis based on a lower bound is not presented. On the other hand, having both an upper and a lower bound on a characteristic time associated with a transition in material behavior would provide insight into the tightness of the bounds.

The characteristic time for pore separation is conservative for two more reasons. One, in this treatment λ_u is a constant such that $\lambda_u > 0 \quad \forall t$ and $\lambda_u > \lambda(t) \quad \forall t$, while $\lambda(t)$ most often evolves from positive values to negative, meaning $G_u(t) \rightarrow G_{max}$ much faster than $G(t) \rightarrow G_{max}$. Two, when the surface area of the cone is less than the surface area of the catenoid, as indicated by figure 3.9, equation (4.22) implies that $G_{u, cone} \rightarrow G_{max}$ much faster than $G_{u, cat} \rightarrow G_{max}$ since the additional area of the catenoid would appear inversely in the exponential of the upper bound. Table 4.1 shows simulations of the time-to-separation compared to predictions from the characteristic time, equation (4.24). The characteristic time is conservative, as expected. Table 4.2 shows the simulated effect of changes in initial conditions and parameter values on the model-exact time-to-separation. Equation (4.24) correctly predicts the increase or decrease in the model-exact time-to-separation. For instance, as the average starting grain size increases, table 4.2 shows the time-to-separation increasing. Equation (4.24) predicts the same. Physically, a smaller grain size implies that the driving force for grain boundary motion decreases, hence the likelihood of separation is diminished. On the other hand, as the initial density increases, table 4.2 shows the time-to-separation as decreasing. From equation (4.24) an increase in the initial density leads to a reduction in the time-to-separation (assuming the densification rate does not change much until the density is greater than 0.99). Physically, as the initial density increases, the pores get smaller and hence there is a smaller drag force on the grain boundaries, hastening the onset of separation. As another example, consider the effect of increasing the processing temperature or pressure; table 4.2 shows both lead

initial condition varied	simulated time-to-transition	equation [4.24]
$\Delta_0 = 0.92$	$4.2 \times 10^4 \text{s}$	$2.09 \times 10^4 \text{s}$
$\Delta_0 = 0.94$	$2.8 \times 10^4 \text{s}$	$1.75 \times 10^4 \text{s}$
initial condition varied	simulated time-to-transition	equation [4.24]
$\tilde{R}_0 = 0.4$	$4.2 \times 10^4 \text{s}$	$2.09 \times 10^4 \text{s}$
$\tilde{R}_0 = 0.6$	$1.2 \times 10^5 \text{s}$	$8.58 \times 10^4 \text{s}$

Table 4.1 Simulated time-to-separation compared to predictions from the characteristic time. Unless otherwise noted, the initial state of each simulation was $\tilde{R}_0 = 0.4$ and $\Delta_0 = 0.92$, for $T = 1573 \text{ K}$ and $P = 50 \text{ MPa}$. Simulations used parameter values for alumina from [14].

to a decrease in the time-to-separation. The decrease is much more dramatic for a temperature increase than a pressure increase. The effect of temperature and pressure on the time-to-separation predicted by equation (4.24) is found by interpreting the effect of temperature and pressure on the rate of densification. Increasing the temperature or pressure will increase the rate of densification, which equation (4.24) shows will decrease the time-to-separation. The effect of temperature variations is more profound than pressure variations on densification, hence equation (4.24) shows the time-to-separation is more sensitive to a temperature increase than a pressure increase. Physically, diffusion is a thermally activated processes, so greater sensitivity to temperature variations as opposed to pressure variations is expected. In addition, for a constant average grain diameter smaller pores translate to decreased likelihood for separation, so an increased rate of densification would lead to an increase in the time-to-separation as equation (4.24) predicts. As a final example, if a material is chosen that has a larger surface energy as compared to some other material, table 4.2 shows the time-to-separation as nearly constant. Equation (4.24) has a parameter for surface energy embedded in the expressions

for densification rate. Surface energy appears in these rate equations linearly, so the effect of an increase in surface energy leads to a small decrease in the time-to-separation as compared to the parameters that appear exponentially. In fact, equation (4.24) indicates that any changes to the value of a material parameter that is included in the densification rate will tend to have the opposite effect on the time-to-separation; a prediction supported by physical reasoning that was argued above.

While the predictions by the characteristic time shown in tables 4.1 and 4.2 appear to agree well with physical arguments and simulations, this is not a proof of the validity of the characteristic time. As detailed in section 4.3, there are issues that need to be resolved before this characteristic time should be used.

Quantity Varied	Values				
\tilde{R}_0	0.2	0.3	0.4	0.6	0.8
Time-to-Separation (s)	7.0×10^3	2.0×10^4	4.2×10^4	1.2×10^5	4.0×10^5
Δ_0	0.92	0.93	0.94	0.95	0.96
Time-to-Separation (s)	4.2×10^4	3.5×10^4	2.8×10^4	2.0×10^4	8.0×10^3
T (K)	1200	1400	1600	1800	2000
Time-to-Separation (s)	3.5×10^9	3.8×10^6	2.3×10^4	410	17
P (MPa)	10	20	30	40	50
Time-to-Separation (s)	4.0×10^7	8.0×10^5	2.0×10^5	8.0×10^4	4.2×10^4
γ (J/m ²)	0.36	0.63	0.9	1.17	1.44
Time-to-Separation (s)	4.4×10^4	4.2×10^4	4.2×10^4	4.0×10^4	3.8×10^4
Q_b (J/mol)	168×10^3	293×10^3	419×10^3	545×10^3	670×10^3
Time-to-Separation (s)	~0	3.5×10^3	4.2×10^4	4.2×10^4	4.2×10^4
Q_c (J/mol)	191×10^3	334×10^3	477×10^3	620×10^3	763×10^3
Time-to-Separation (s)	Trajectory stays in drag region.	Trajectory stays in drag region.	4.2×10^4	850	17
S_{ref} (N/m ²)	500×10^6	875×10^6	1250×10^6	1625×10^6	2000×10^6
Time-to-Separation (s)	2.5×10^3	1.4×10^4	4.2×10^4	9.0×10^4	1.75×10^5

Table 4.2 Model-exact time-to-separation as a function of changes in initial state, temperature, pressure, and material parameter values for alumina. Unless otherwise noted, the initial state of each simulation was $\tilde{R}_0 = 0.4$ and $\Delta_0 = 0.92$, for

$$T = 1573 \text{ K and } P = 50 \text{ MPa.}$$

CHAPTER 5 Closing

This chapter begins by discussing the main results of this work. Following this discussion, suggestions to improve the internal variable models and auxiliary functions are summarized. Finally, some preliminary work on how the models can be used in an adaptive control framework is presented.

5.1 Main Results of this Work

This work uses a model-based approach to derive criteria that predict the onset of two transitions in material behavior that are routinely encountered in processes of component production. The first criterion shows explicitly the interaction of internal structure with temperature and strain rate to predict the initial peak in stress associated with dynamic recrystallization. No other criteria from previous research shows this explicit relation. The second criterion shows the interaction between the grain growth rate and the densification rate, modified by the grain size and relative porosity of the material to predict the rapid increase in grain growth rate associated with pore separation. It is the first criterion for pore separation that explicitly shows the effect of variations in temperature, pressure, and material parameters on internal structure; none of the existing criteria account for all of these quantities at once.

The benefit of taking a model-based approach as compared to an empirical approach is the ability to use the models and the criteria beyond the data used to validate them. This work presents three applications of the criteria and models: one, processing envelopes that plot the onset of the transitions as a boundary in state space, two, a graphical way to show the effect of uncertainties in the parameter values on the predictions made by the criteria, and three, an adaptive control framework.

5.2 Suggested Improvements to the Internal Variable Models

The model of the kinetic processes associated with dynamic recrystallization presented in chapter 2 treats the nucleation site density as constant, as argued by Roberts

et. al. [27]. They state that the nucleation sites involved in the initial wave of recrystallization remains constant. This research has evidence suggesting that the nucleation site density is increasing during the first wave of recrystallization. The evidence is given in figures 2.7 and 2.7. The figures show the predicted strain at peak stress is too large as compared to the experimental data at the higher strain rates. If the nucleation site density did increase, instead of remaining constant, then the simulated volume fraction of recrystallized material would also increase, thereby reducing the predicted strain at peak stress. Physically, it is reasonable to assume that the nucleation site density may increase since the dislocation density is also increasing due to work hardening. Peczak and Luton [41] present a model for the evolution of nuclei as a function of dislocation density. While it is true that models of nucleation are still not well established, it would be interesting to see if adding a characterization of nucleation to the kinetic model presented in chapter 2 improved the ability of the criterion to predict the strain at peak stress. Or, perhaps, the additional kinetic equation could possess a stability structure that contains a boundary that corresponds to the first peak in stress.

In chapter 3, the idealized shape of a grain boundary local to a pore attached to a grain boundary is given as a catenoid of revolution, as first reported by Hellman and Hillert [49]. This research approximates the shape by a right circular cone, for mathematical convenience. Better approximations of this shape should be investigated. Also, the data presented in chapter 3 is for sintering only. To test the criterion further it is vital that data from hot isostatic pressing experiments be collected.

Chapter 4 already has a section with detailed suggestions for improvement that do not bear repeating in this last chapter.

5.3 Preliminary Work using the Models in an Adaptive Control Framework

The models of the kinetic processes presented in chapters 2 and 3 are each a system of low-order, lumped-parameter ODEs. This mathematical form is suitable for building a simulated control system. This section gives an example of the model of the kinetics associated with dynamic recrystallization used in a simulated adaptive controller.

The objective of the control system is to compute the necessary temperature and strain rate history in order for the system to reach desired final values of dislocation density and

volume fraction recrystallized, in the presence of uncertainties in the values of two parameters. There is one uncertain parameter per ODE in the formulation presented here. The approach is to first feedback-linearize the ODEs and then embed the linearized plants in an adaptive control structure. The adaptive controller is an indirect scheme called dynamic parameter estimation [73]. Dynamic parameter estimation was chosen, because it reduces overshoot in the system response as compared to simpler indirect schemes.

This control system has an obvious shortcoming. The adaptive controller does not account for unmodelled dynamics. The controller could be improved by incorporating robustness to unmodelled dynamics. This section does not consider robustness. The control system is presented to illustrate how the models developed in chapters 2 and 3 can be used in a control system. It is left for future work to improve on the control system presented here.

5.3.1 Feedback Linearization

The objective of feedback linearization is to cancel the effect of nonlinear terms in the system to be controlled and replace the cancelled terms with simpler terms [9]. The feedback linearization presented here replaces the nonlinear terms in the model of the kinetics associated with dynamic recrystallization with terms that make the system behave as two decoupled, first-order linear ODE's. The feedback linearization is aided by the fact that the two coupled, nonlinear ODE's comprising the model of the kinetic processes associated with dynamic recrystallization is triangular.

To begin the description of the feedback linearization presented in this section, the rate equation modelling the evolution of the volume fraction of recrystallized material given in chapter 2, equation (2.8), is repeated below:

$$\dot{v}_r = 3A_s N_s C_{ac} b v_{gb} v_r^{2/3} \exp\left(\frac{-Q_{gb}}{kT}\right) \left(\frac{\mu b^2 \Omega \rho}{2kT}\right) (1 - v_r). \quad (5.1)$$

For notational simplicity, several of the material parameters in equation (5.1) are lumped into fewer constants:

$$\dot{v}_r = L_1 \exp\left(\frac{-L_2}{T}\right) \rho v_r^{2/3} (1 - v_r). \quad (5.2)$$

Now define

$$T_1 \equiv \exp\left(\frac{-L_2}{T}\right) \quad (5.3)$$

and substitute equation (5.3) into equation (5.2), yielding

$$\dot{v}_r = L_1 T_1 \rho v_r^{2/3} (1 - v_r). \quad (5.4)$$

If the value of T_1 is given by

$$T_1 = \frac{1}{\rho v_r^{2/3} [1 - v_r]} \left[v_r + \frac{v_{rd}}{L_1} \right] \quad (5.5)$$

then substituting equation (5.5) into equation (5.4) gives

$$\dot{v}_r = L_1 v_r + v_{rd} \quad (5.6)$$

which is a first order, linear ODE.

To continue the description of the feedback linearization presented in this section, the rate equation modelling the evolution of the dislocation density given in chapter 2, equation (2.5), is repeated below

$$\dot{\rho} = \frac{A_1}{b} \sqrt{\rho} \left(1 - \frac{\rho}{\rho_{ss}} \right) \dot{\epsilon} \quad (5.7)$$

where

$$\rho_{ss} = \tilde{\rho} \left[\frac{\dot{\epsilon}}{v_{dm} A_3} \exp\left(\frac{Q_{dr}}{kT}\right) \right]^{m_2} \quad (5.8)$$

and the static recovery term does not appear because, as previously mentioned, for

moderate strain rates above 10^{-3} s^{-1} the effect of static recovery can be neglected. For notational simplicity, several of the material parameters in equation (5.7) are lumped into fewer constants yielding:

$$\dot{\rho} = C_1 \sqrt{\rho} \left[1 - \frac{\rho}{C_2 \exp\left(\frac{C_3}{T}\right)} \right] \dot{\epsilon} \quad (5.9)$$

where for mathematical simplicity the steady state dislocation density, ρ_{ss} , is taken as a function of temperature only, i.e. the strain rate was fixed at 0.02 1/s for the computation of C_2 . If the value of $\dot{\epsilon}$ is chosen such that it solves the equation:

$$\dot{\epsilon} = \left[\sqrt{\rho} \left[1 - \frac{\rho}{C_2 \exp\left(\frac{C_3}{T}\right)} \right] \right]^{-1} (\rho + \rho_d) \quad (5.10)$$

then substituting equation (5.10) into equation (5.9) gives

$$\dot{\rho} = C_1 \rho + \rho_d. \quad (5.11)$$

Figure 5.1 shows a block diagram of the feedback linearization procedure described by equations (5.1) to (5.5) and (5.9) to (5.11). Figure 5.1 shows a block diagram of the resulting dynamics of the feedback-linearized system, equations (5.6) and (5.11), illustrated in figure 5.1.

5.3.2 Adaptive Control with Dynamic Parameter Estimation

This section applies an indirect adaptive control scheme to the plants given by equations (5.6) and (5.11). A description of the theoretical foundations of many forms of adaptive control are given by Narendra and Annaswamy [73]. The reference models used in the adaptive controller was chosen as a first order linear ODE to complement the feedback-linearized plants. The time constant for the reference models was chosen to be roughly equal to the the time scale for dynamic recrystallization at a moderate strain rate, namely 25 seconds. The adaptive controller is given by the following two systems of equations. The first system controls the dislocation density, the second controls the volume fraction recrystallized. Together they compute the necessary values for the processing inputs,

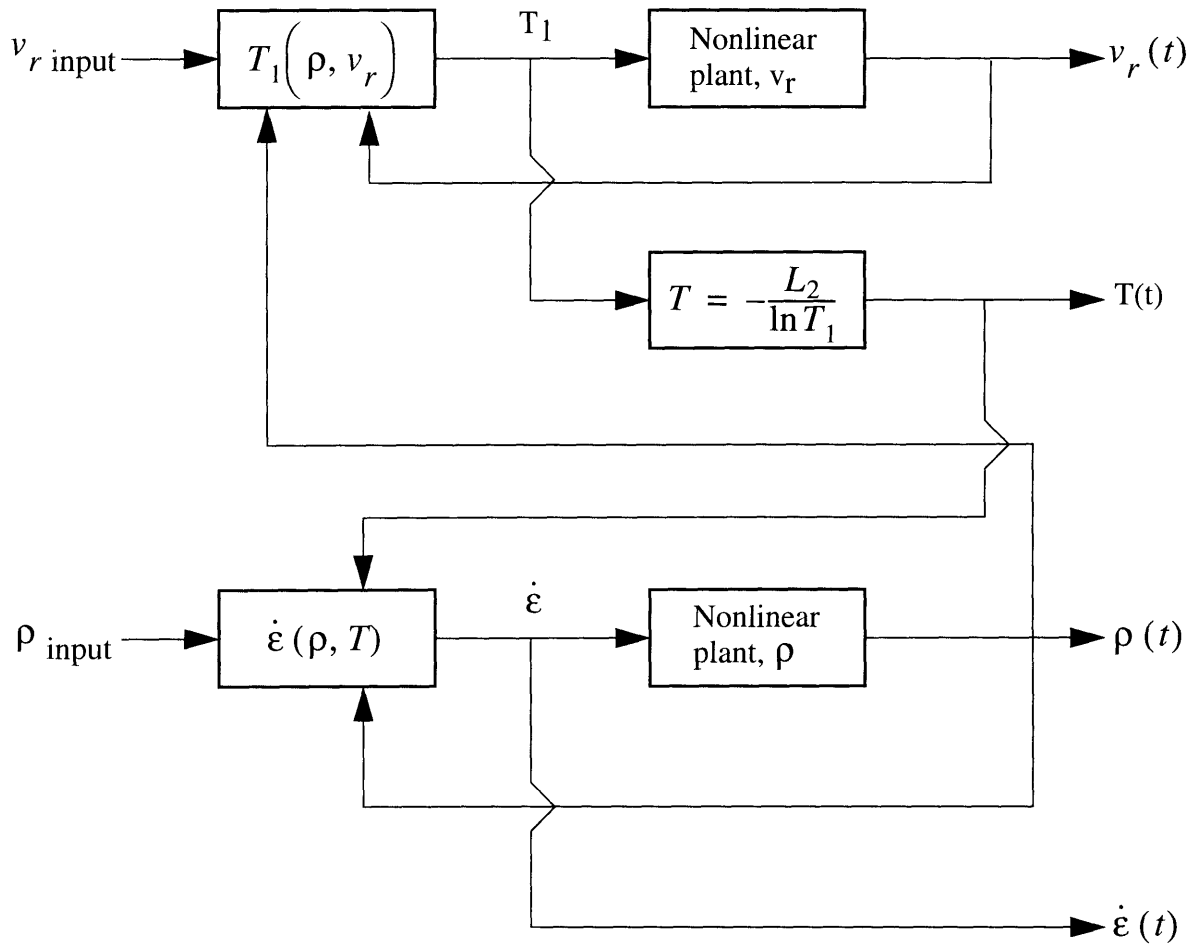


Figure 5.1 Block diagram of the feedback linearization given by equations (5.1) to (5.5) and (5.9) to (5.11).

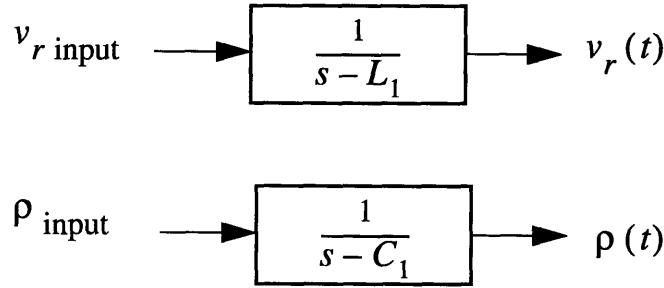


Figure 5.2 Block diagram of the resulting dynamics of the feedback-linearization system illustrated in figure 5.1.

temperature and strain rate, to achieve the desired values of dislocation density and volume fraction recrystallized.

CONTROL OF VOLUME FRACTION RECRYSTALLIZED

PLANT $\dot{v}_{rp} = L_1 v_{rp} + v_{rd}$ (5.12)

MODEL $\dot{v}_{rm} = 0.04 v_{rm} + r_v$ (5.13)

ESTIMATOR $\dot{\hat{v}}_{rp} = 0.04 \hat{v}_{rp} + [\hat{L}_1 - 0.04] v_{rp} + v_{rd}$ (5.14)

ERROR $e_v = \hat{v}_{rp} - v_{rp}$ (5.15)

ADAPTATION LAW $\dot{\hat{L}}_1 = -v_{rp} [\hat{v}_{rp} - v_{rp}] - e_{\theta v}$ (5.16)

FEEDBACK GAIN LAW $\dot{\theta}_v = -e_{\theta v} = -[-\hat{L}_1 + \theta_v - 0.04]$ (5.17)

where $v_{rd} = r_v + \theta_v v_{rp}$ and $\theta_v = 0.04 - \hat{L}_1$. (5.18)

CONTROL OF DISLOCATION DENSITY

$$\underline{\text{PLANT}} \quad \dot{\rho}_p = C_1 \rho_p + \rho_d \quad (5.19)$$

$$\underline{\text{MODEL}} \quad \dot{\rho}_m = 0.04 \rho_m + r_\rho \quad (5.20)$$

$$\underline{\text{ESTIMATOR}} \quad \dot{\hat{\rho}}_p = 0.04 \hat{\rho}_p + [\hat{C}_1 - 0.04] \rho_p + \rho_d \quad (5.21)$$

$$\underline{\text{ERROR}} \quad e_\rho = \hat{\rho}_p - \rho_p \quad (5.22)$$

$$\underline{\text{ADAPTATION LAW}} \quad \dot{\hat{C}}_1 = -\rho_p [\hat{\rho}_p - \rho_p] - e_{\theta\rho} \quad (5.23)$$

$$\underline{\text{FEEDBACK GAIN LAW}} \quad \dot{\theta}_\rho = -e_{\theta\rho} = -[-\hat{C}_1 + \theta_\rho - 0.04] \quad (5.24)$$

$$\text{where} \quad \rho_d = r_\rho + \theta_\rho \rho_p \quad \text{and} \quad \theta_\rho = 0.04 - \hat{C}_1. \quad (5.25)$$

A block diagram for adaptive controller of volume fraction recrystallized, equations (5.12) to (5.18), with feedback-linearized plant, equations (5.6) is shown in figure 5.1. The adaptive controller of dislocation density has the same structure as the block diagram in figure 5.1.

5.3.3 Simulation Results

Simulations of the adaptive controller, equations (5.12) to (5.25), were first conducted using nonphysical, whole numbers for the inputs, r_v and r_ρ , and parameter values, C_1 and L_1 , to facilitate validation of the computer program. Figure 5.4 shows a typical simulated response to a step input where the initial conditions for the states where $v_{rp} = \rho_p = 0$. The estimators started with $\hat{C}_1 = 1.5$ and $\hat{L}_1 = 2.0$ while the plants used $C_1 = 3.0$ and $L_1 = 4.0$.

The adaptive controller was then simulated using parameter values for OFHC copper, given in table (2.1). Using these parameter values, $C_1 = 35.2 \times 10^6$ and

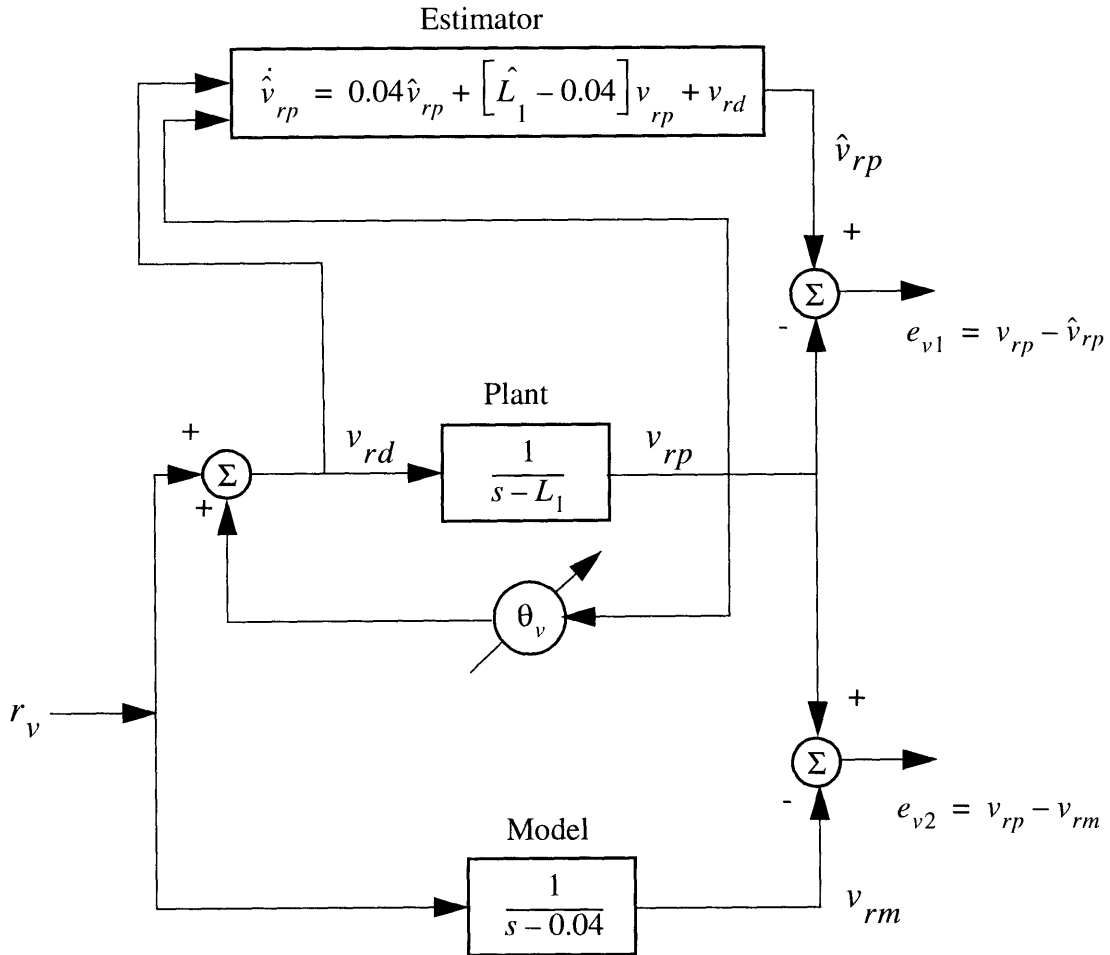


Figure 5.3 Block diagram of one-half of the adaptive controller, equations (5.12) to (5.18), with feedback-linearized plant, equations (5.6).

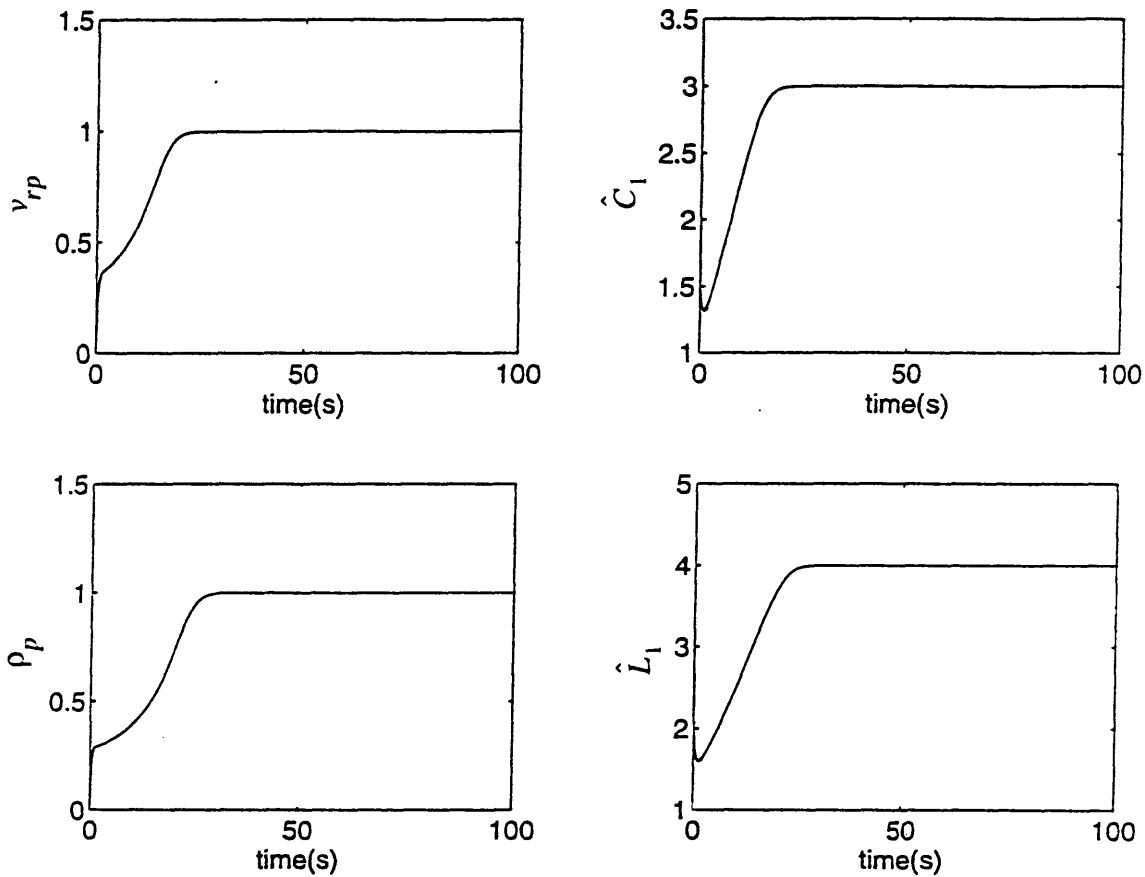


Figure 5.4 Simulation of the adaptive control strategy using inputs and parameter values to facilitate validation of the computer program.

$L_1 = 12.6 \times 10^{-22}$. The simulations started with parameter values 50% less than the values used by the plants. The initial conditions were $\rho_p = 1 \times 10^{10} \text{ m/m}^3$ and $v_{rp} = 1 \times 10^{-11}$ and the inputs were $r_v = 0.3$ and $r_\rho = 1 \times 10^{14}$. The simulations were performed on a 486 workstation using a fourth-order Runge-Kutta routine. The result of typical simulation is given in figure 5.1. The figure gives the time history of temperature and pressure inputs in order to achieve the desired state values. The simulation was stopped at 1 second because the computation speed was excessively slow..

5.4 Suggested Future Work

A broader suggestion for future work is to include the state space representation into the mainstream of analysis of material phenomena. The trajectories plotted in chapters 2 and 3 alone, without the criteria developed by this work, are valuable tools to plan process

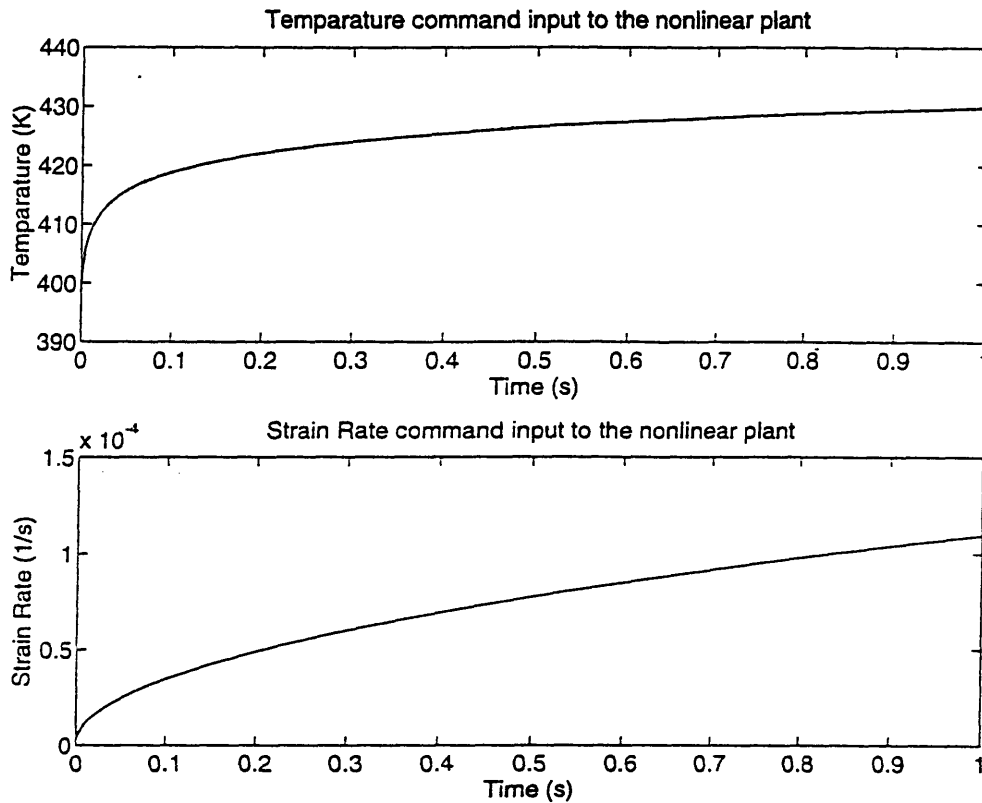


Figure 5.5 Partial time-histories of temperature and strain rate inputs required to for the states to evolve to $v_r = 0.3$ and $\rho = 1 \times 10^{14} \text{ m/m}^3$.

schedules and aid in the design of machinery. With the addition of criteria to predict transitions in material behavior, the state space representations could be used as processing envelopes. These processing envelopes could provide manufacturers a means of readily interpreting the effects of process inputs on material behavior. The process inputs could be set to avoid or exploit a transition in material behavior. The envelopes would also serve as a means of retaining processing knowledge and a record of improvements to that knowledge.

The criterion might conceivably be used as a cost function in a control strategy that computes processing input histories that simultaneously achieve a target state value while avoiding a transition in material behavior.

Finally, even though this research shows that it is possible to develop criteria using a low-order model that does not have a stability structure with a boundary that corresponds to a transition being studied, it would be intriguing to model a transition with a stability

structure that has such a boundary. The insight gained from this effort would likely help in developing new models of complex material behavior.

References

1. Materials Science and Engineering for the 1990s: National Research Council, 1989.
2. Advanced Materials by Design: U. S. Office of Technology Assessment, 1989.
3. S. B. Brown, K. H. Kim, and L. Anand: *International Journal of Plasticity*, 1989, volume 5 (2), pp. 95-130.
4. O. Levenspiel: *Chemical Reaction Engineering*, Chapters 11-13, John Wiley, 1962.
5. O. Penrose and P. C. Fife: *Physics D.*, 1990, vol. 43, pp. 44-62.
6. H. L. Gegel: *Computer Simulation in Materials Science—An ASM Materials Science Seminar*, ASM, Orlando, FL, Oct. 1986.
7. P. Holmes: *Nonlinear Dynamics, Chaos, and Mechanics*, Applied Mechanics Reviews, vol. 43, pp. S23-S39, 1990.
8. S. Strogatz: *Nonlinear Dynamics and Chaos*, Addison-Wesley, Redwood City, CA, 1994.
9. J. E. Slotine and W. Li: *Applied Nonlinear Control*, Prentice Hall, New York, NY, 1991.
10. D. Luenberger: *Introduction to Dynamic Systems*, John Wiley & Sons, New York, NY 1979.
11. W. Hahn: *Stability of Motion*, Chapter 4, Springer-Verlag, New York, NY, 1967.
12. W. Walter: *Differential and Integral Inequalities*, Chapter 1, Springer-Verlag, New York, NY, 1964.
13. M. Vidyasagar: *Nonlinear Systems Analysis*, Chapter 4, Prentice Hall, Englewood Cliffs, NJ, 1993,
14. H. J. Frost and M. F. Ashby: *Deformation Mechanism Maps*, Pergamon Press, New York, NY, 1982.
15. T. Sakai and M. Ohashi: Dislocation Substructures Developed During Dynamic Recrystallization in Polycrystalline Nickel, *Materials Science and Technology*, 1990, vol. 6, pp. 1251 - 1257.
16. M. J. Luton and C. M. Sellers: *Acta Metallurgica*, 1969, vol. 17, pp. 1033-1043.
17. T. Sakai and J.J. Jonas: *Acta Metallurgica*, 1984, vol. 32 (2), pp. 189-209.
18. R. Sandstrom and R. Lagneborg: *Acta Metallurgica*, 1975, vol. 23, pp. 387-398.

19. R. O. Adebajo and A. K. Miller: *Materials Science and Engineering*, 1989, vol. A119, pp. 87-94.
20. A. K. Miller: *Journal of Engineering Materials Technology*, 1976, vol. 98 (2), pp. 97-113.
21. R. W. Cahn: *Physical Metallurgy*, North-Holland Physics Publishing, Amsterdam, 1983, chapter 25, pp. 1595-1670.
22. E. Voce: *Acta Metallurgica*, 1955, May, pp. 219-226.
23. F. B. Prinz and A. S. Argon: *Acta Metallurgica*, 1984, vol. 32 (7), pp. 1021-1028.
24. W. D. Nix, J. C. Gibeling, and D. A. Hughes: *Metallurgical Transactions A*, 1985, vol. 16A, pp. 2215-2226.
25. J. Bonneville and B. Escaig: *Acta Metallurgica*, 1987, vol. 27, pp. 1477-1486.
26. U. F. Kocks: *Journal of Engineering Materials Technology*, 1976, January, pp. 76-85.
27. W. Roberts, H. Boden, and B. Ahlblom: *Metals Science*, 1979, March-April.
28. R. D. Doherty: *Physical Metallurgy*, North Holland Physics Publishing, Amsterdam, 1983, chapter 25, pp. 934-1030.
29. L. Blaz, T. Sakai, and J. J. Jonas: *Metals Science*, 1983, vol. 17, pp. 609-616.
30. U. F. Kocks, A. S. Argon, and M. F. Ashby: *Thermodynamics and Kinetics of Slip*, Pergamon Press, New York, NY, 1975.
31. F. A. McClintock and A. S. Argon: *Mechanical Behavior of Materials*, Addison-Wesley, Reading, MA, 1966.
32. J. W. Christian: *The Theory of Transformations in Metals and Alloys*, Pergamon Press, New York, NY, 1975, chapter 10, pp. 448-457.
33. J. E. Dorn: *Mechanical Behavior of Materials at Elevated Temperatures*, McGraw-Hill, New York, NY, 1961.
34. J. Weertman: *Journal of Applied Physics*, 1955, vol. 26, pp. 1213-1217.
35. D. Kuhlmann-Wilsdorf: *Metallurgical Transactions A*, 1985, vol. 16A, pp. 2091-2108.
36. W. D. Nix and J. C. Gibeling: *1985 ASM Materials Science Seminar, Metals/Materials Technology Series*, ASM, Metals Park, OH, 1985, pp. 1-63.
37. The NAG Fortran Library Manual, NAG Inc., IL, 1988, Mark 13, vol. 2.
38. D. W. Jordan and P. Smith: *Nonlinear Ordinary Differential Equations*, Clarendon Press, London, 1987.

39. J. W. Cahn and J. E. Hilliard: *Journal of Chemical Physics*, 1958, vol. 28 (2), pp. 258-267.
40. M. J. Luton: Private communication, Exxon Research Center, New Jersey, 1994
41. P. Peczak and M. J. Luton: *The Effect of Nucleation Models on Dynamic Recrystallization. I. Homogeneous Stored Energy Distribution*, Philosophical Magazine B, 1993, vol. 68, pp. 115-144.
42. E. H. Aigeltinger: *An Experimental Determination of the Topological Properties of Sintered Structures*, Ph.D. Thesis, University of Florida, 1970.
43. C. Zener quoted by C. S. Smith: *Grains, Phases, and Interfaces: An Interpretation of Microstructures*, Transactions of the American Institute of Mining Engineers, 1948, vol. 175, pp. 47-49.
44. F. A. Nichols: *Further Comments on the Theory of Grain Growth in Porous Compacts*, Journal of the American Ceramic Society, 1968, vol. 51, pp. 468-469.
45. R. J. Brook: *Pore-Grain Boundary Interactions and Grain Growth*, Journal of the American Ceramic Society, 1968, vol. 52, pp. 56-57.
46. W. D. Kingery and B. Francois: *Grain Growth in Porous Compacts*, Journal of the American Ceramic Society, 1965, vol. 48, pp. 546-547.
47. M. V. Speight and G. W. Greenwood: *Grain Boundary Mobility and its Effects in Materials Containing Inert Gases*, Philosophical Magazine, 1964, pp. 683-689.
48. T. Gladman: *On the Theory of the Effect of Precipitate Particles on Grain Growth in Metals*, Proceedings of the Royal Society A, 1966, vol. 294, pp. 298-309.
49. P. Hellman and M. Hillert: *On the Effect of Secondary-Phase Particles on Grain Growth*, Scandinavian Journal of Metallurgy, 1975, vol. 4, pp. 211-219.
50. P. M. Hazzledine, P. B. Hirsch and N. Louat: *Migration of a Grain Boundary Through a Dispersion of Particles*, N. Hansen ed., First RISO Conference, 1980.
51. C. H. Worner and A. Cabo: *On the Shape of a Grain Boundary Pinned by a Spherical Particle*, Scripta Metallurgica, 1984, vol. 18, pp. 565-568.
52. C. H. Worner, A. Cabo and M. Hillert: *On the Limit for Particle Attachment in Zener Drag*, Scripta Metallurgica, 1986, vol. 20, pp. 829-831.
53. R. Elst, J. Van Humbeeck and L. Delaey: *Evaluation of Grain Growth Criteria in Particle-Containing Materials*, Acta Metallurgica, 1988, vol. 36, pp. 1723-1729.
54. M. F. Ashby: *Sintering and Isostatic Pressing Diagrams*, Cambridge University, Department of Engineering, UK, 1990.

55. Y. Liu and B. R. Patterson: *Grain Growth Inhibited by Porosity*, in press, 1993
56. M. J. Gore, M. Grujicic, G. B. Olson and M. Cohen: *Thermally Activated Grain Boundary Unpinning*, *Acta Metallurgica*, 1989, vol. 37, pp. 2849-2854.
57. M. Hillert: *On the Theory of Normal and Abnormal Grain Growth*, *Acta Metallurgica*, 1965, vol. 13, pp. 227-238.
58. M. F. Ashby, J. Harper and J. Lewis: *The Interaction of Crystal Boundaries with Second-Phase Particles*, *Trans. of the Metallurgical Society of AIME*, 1969, vol. 245, pp. 413-420.
59. M. A. Spears and A. G. Evans: *Microstructure Development During Final/Intermediate Stage Sintering -I. Pore/Grain Boundary Separation*, *Acta Metallurgica*, 1982, vol. 30, pp. 1281-1289.
60. C. H. Hsueh, A. G. Evans and R. L. Coble: *Microstructure Development During Final/Intermediate Stage Sintering -I. Pore/Grain Boundary Separation*, *Acta Metallurgica*, 1982, vol. 30, pp. 1269-1270.
61. S. P. Ringer, R. P. Kuziak and K. E. Easterling: *Liquid Film Simulation of Zener Grain Boundary Pinning by Second Phase Particles*, *Materials Science and Technology*, 1991, vol. 7, pp. 193-200.
62. B. J. Kellet and F. F. Lange: *Experiments on Pore Closure During Hot Isostatic Pressing and Forging*, *Journal of the American Ceramic Society*, 1988, vol. 71, pp. 7-12.
63. F. B. Swinkels and M. F. Ashby, *A Second Report on Sintering Diagrams*, *Acta Metallurgica*, 1981, vol. 28, pp. 259 - 281.
64. M. F. Ashby: *The Modelling of Hot-Isostatic Pressing*: Cambridge University, Department of Engineering, UK, 1987.
65. *Journal of Physical Chemistry*, volume 14, supplement 1, 1985.
66. W. L. Masterson, E. J. Slowinski: *Chemical Principles*, W. B. Saunders Company, Philadelphia, PA, 1977, Appendix A.
67. B. R. Patterson: Private communication, University of Alabama, Birmingham, Alabama, 1994.
68. G. Long: Private communication, National Institute of Standards and Technology, Gaithersburg, Maryland, 1994.
69. A. Watwe: Private communication, INCO Alloys International, Huntington, West Virginia, 1994.
70. P. G. Drazin: *Nonlinear Systems*, Chapter 4, 1993.
71. G. Simmons: *Differential Equations*, Chapter 2, Section 10, McGraw Hill, 1972.

72. A. P. Mishina and I. V. Proskuryakov; Higher Algebra, Chapter 3, Pergamon Press, 1965
73. K. Narendra and A. Annaswamy; Stable Adaptive Systems, Chapter 3, Prentice Hall, 1992.